MRI Guidance of Transcranial Histotripsy Treatments

by

Dinank Gupta

A dissertation submitted in partial fulfillment
of the requirements for the degree of
Doctor of Philosophy
(Biomedical Engineering)
in the University of Michigan
2024

Doctoral Committee:

Professor Douglas C. Noll, Co-Chair
Professor Zhen Xu, Co-Chair
Assistant Professor Steven P. Allen
Professor Jeffrey A. Fessler
Associate Research Scientist Timothy L. Hall
Associate Professor Zhongming Liu

Dinank Gupta
dinankg@umich.edu
ORCID iD: 0000-0001-7496-1056

DEDICATION

To my grandparents Om Prakash Gupta and Daya Rani Gupta.

ACKNOWLEDGEMENTS

First and foremost, I would like to thank my advisors, Dr. Zhen Xu and Dr. Douglas Noll. Throughout these years, they have been tremendously supportive, given me space to explore my interests, and provided me with guidance every step of the way. I could not have asked for better advisors. Zhen is one of the most driven and visionary researchers I have seen. She has taught me that a good scientist not only does good science but also needs to be better at science communication and a better scientific writer. Doug is a fantastic mentor who has supported my interests and ambitions. Doug is an expert in MRI, and my love for this domain is primarily due to how much I have learned from Doug. I want to thank Dr. Tim Hall for his continuous support and guidance during my Ph.D. Tim has constantly challenged me, but he always listened to me and guided me to think and work like a scientist. I want to also thank Dr. Jon-Fredrik Nielsen for his help with pulse sequence programming and fun conversations. I want to thank Dr. Scott Peltier, Dr. Ulrich Scheven, Krisanne Litinas, and Dave Choi for their support with technical challenges with MRI. Lastly, I would like to thank Drs. Steven Allen, Jeff Fessler, and Zhongming Liu to be on my thesis committee. Their feedback and support have been crucial to my dissertation.

My PhD would be incomplete (and boring) without my amazing lab mates. I had the privilege of collaborating with many outstanding scientists: Tarana Kaovasia, Ning Lu, Ellen Yeats, Mariama Salifu, Scott Haskell, and Rodrigo Lobos. I feel fortunate to be a part of fMRI, Histotripsy, and Fessler labs. I had the pleasure of interacting with a remarkable set of people: Shouchang Guo, Melissa Haskell, Amaya Murguia, Rex Fung, David Frey, Jayden Pothoof, Yongli He, Andrea Jacobson, Robert Jones, Guanhua Wang, Haowei Xiang, Ryan Hubbard, Greyson Stocker, Sarah Duclos, Christina Hendren, Mahmoud Komaiha, Reliza McGinnis, Tejaswi Worlikar, Hanna Kim, James Messina, Sang Won Choi and Tianrui Luo. I wish them all the best in their future.

No Ph.D. journey is done alone. Through lots of ups and downs of research, I have always been able to count on my friends. From spending summers on the beaches or tubing and kayaking on the river to playing board games in the winters, to celebrating many festivals, my friends never made me feel alone. I want to thank Naveen, Harsha, Anish, Navid, Shreyas, Ari, Rachana, Preeti, Alex, Shariq, Bikash, Ross, Bianca, Gaurish, Olivia, Diana, Wenyuan,

Natasha, Adelaide, Liz, Raksha and many others for being there for me throughout these many years.

I feel extremely lucky to have a loving and supportive family. Although being so far away from them was extremely hard at times, talking with my parents almost every day while I walked to the lab made me feel close to them and kept me sane in tough times. I also want to thank my family members in India and the US for being tremendous support for me and my parents throughout the years that I have been in the US. I also want to acknowledge my brother's support for all these (10+) years that we have been in the US. He has always been there for me through all the stages of my journey, and I know I can always count on him to be there.

Finally, Sushmitha — my best friend, cheerleader, and future. Sush has been by my side since our undergraduate studies, through a global pandemic and years of ups and downs during my Ph.D.. This dissertation would have been impossible without Sush's positivity and cheerfulness. Regardless of what the future holds, I will be happy spending it with her.

TABLE OF CONTENTS

LIST OF FIGURES

FIGURE

LIST OF ACRONYMS

CNS Central Nervous System

MRI Magnetic Resonance Imaging

FUS Focused Ultrasound

tcMRgFUS Transcranial MR-guided Focused Ultrasound

tcMRgHIFU Transcranial MR-guided High Intensity Focused Ultrasound

tcMRgHt Transcranial MR-guided Histotripsy

PRF Proton Resonance Frequency

HIFU High Intensity Focused Ultrasound

ARFI Acoustic Radiation Force Imaging

MR-ARFI MR-Acoustic Radiation Force Imaging

GRE Gradient Recalled Echo

ADC Apparent Diffusion Coefficient

FFT Fast Fourier transform

ABSTRACT

Brain cancers account for over 250000 deaths per year worldwide, with over 300000 new cases reported every year. There are three main treatment options for patients with brain tumors: surgery, radiation therapy, and chemotherapy. Surgery and radiation therapy are the most commonly used practices, but they expose patients to infections, trauma, and damage to the surrounding cerebral parenchyma or expose patients to ionizing radiation. Chemotherapy has seen limited success in treating brain tumors due to the presence of the blood-brain barrier (BBB) that prohibits chemotherapeutic drugs from entering the brain.

Histotripsy is a focused ultrasound-based therapy that uses cavitation to precisely and non-invasively treat tissues. Performing histotripsy treatments requires imaging guidance to localize the treatment region and monitor treatment outcomes.This dissertation presents methods to perform transcranial histotripsy treatments using treatment guidance from MR imaging.

The first chapter discusses the prevalence of brain tumors and the treatment options available for treating tumors. The second chapter introduces the technical background of histotripsy and MRI and discusses the relevant topics that combine focused ultrasound and MRI.

The third and fourth chapters discuss methods to perform histotripsy pre-treatment targeting in *ex-vivo* brain tissues. The method involves acquiring MR-thermometry and/or MR-Acoustic Radiation Force (MR-ARFI) images before the histotripsy treatments and then comparing the estimated focus from the two methods to the focus estimated from a histotripsy lesion generated at the same target location. Both the pre-treatment targeting methods perform similarly well in estimating histotripsy lesions with mean absolute errors along the transverse/longitudinal axis of 2.06 mm/2.95 mm and 2.13 mm/2.51 mm for MR-ARFI and MR-thermometry, respectively.

The fifth chapter discusses a method to perform real-time monitoring of histotripsy treatments in *ex-vivo* brain. MR images are sensitized to histotripsy cavitation cloud-induced motion by encoding motion using a set of bipolar gradients. Image magnitude and phase changes are shown to provide complementary information about the lesion. The image magnitude decreases due to the increased random motion within the lesion. The image phase

encodes the motion induced by the bubble cloud and indicates a net motion away from the histotripsy transducer. The sensitivity to the lesion is controlled by both the amplitude and the spacing of the encoding gradients. This method was validated by monitoring histotripsy sonications through the skull with 0.5 s temporal resolution using a spiral acquisition.

The sixth chapter describes different MR-visible parameters that change with histotripsy dose in the brain. MR parameter maps of T1, T2, and Apparent Diffusion Coefficient (ADC) for varying histotripsy treatment doses are acquired. It is observed that the T1 and T2 do not correlate with the histotripsy dose. The ADC within the lesion increases as more histotripsy dose is delivered. As histotripsy breaks down the cellular structure, it significantly increases the diffusion of water within the lesion, which is quantified using the lesion's ADC ($p < 0.001$). For the tissues treated in this study, the ADC increased by $6.5 \times 10^{-4}\,\mathrm{mm^2/s}$ with 50 reps of histotripsy dose across three tissues.

The final chapter summarizes the findings and contributions of this dissertation and discusses future work to advance MR methods for treating brain tumors using histotripsy.

CHAPTER 1

Introduction

Over 700 000 Americans are living with brain tumors [83]. About 24 000 new patients are diagnosed with brain and Central Nervous System (CNS) tumors, with an estimated 18 000 deaths each year [46, 11, 5]. The brain is also one of the primary sites for tumor metastasis from the bladder, kidneys, lung cancers, leukemia, lymphoma, and melanoma [83].

Surgical resection of tumors by craniotomy is the backbone of brain tumor treatments [41]. Craniotomy involves the opening up of brain dura and removal of the tumorous tissue [41, 16]. This procedure is highly invasive and associated with surgical trauma, infections, and impaired motor and sensory response [16, 55]. Radiation therapy has limited treatment capability with poor treatment outcomes [62] and can be used only for smaller treatment volumes. Drug delivery to the central nervous system is largely restricted by the blood-brain barrier (BBB). One of the biggest hurdles for drug delivery is the large molecular weights of the drugs that cannot cross the BBB [84].

Focused Ultrasound (FUS) is a non-ionizing and non-invasive therapy being investigated for treating brain tumors. Two main types of FUS therapies based on continuous wave (CW) ultrasound are currently used: High Intensity Focused Ultrasound (HIFU) for thermal ablation [17, 45] and low-intensity FUS for BBB opening [12, 74]. Transcranial MR-guided High Intensity Focused Ultrasound (tcMRgHIFU) is approved by the FDA and is clinically used to treat essential tremors and Parkinson's disease [63, 21]. Recent human trials of tcMRgHIFU for brain tumor treatment have provided fundamental limitations to the system: long treatment times, the ability to treat small volume within the center of the brain, and over-heating of the skull [17, 12, 72]. The majority of brain tumors are present close to the skull surface and are, therefore, hard to treat by HIFU. Low-intensity FUS BBB opening facilitates the delivery of heavier chemotherapy drugs to the brain by partially opening the BBB [12]. There has been limited evidence regarding the safety and efficacy of brain treatment using this approach.

Histotripsy is also a non-invasive FUS treatment method that uses short, high-pressure ultrasound pulses to generate focal cavitation and liquefy tissues [108]. Unlike HIFU, which

relies on CW ultrasound pulses to heat the tissue and cause thermal necrosis, histotripsy uses μs-long pulses to generate acoustic cavitation and mechanically fractionate the tissues into an acellular homogenate [107, 7]. Histotripsy is a threshold phenomenon localized to the region where the peak negative pressure increases a certain cavitation threshold; it imparts no damage to tissues below the cavitation threshold. Histotripsy is FDA-approved for the treatment of liver tumors. A recent clinical trial of histotripsy treatment of liver tumor resulted in 100 % technical success in creating planned treatment volume with no complications. Moreover, a few patients in the study reported abscopal response to treatment [99].

Histotripsy is currently being evaluated as a potential therapy for treating brain diseases [94, 65, 66]. Recent *in-vivo* animal studies have successfully demonstrated the feasibility of using this therapy for non-invasive brain treatments [94, 65]. Transcranial MR-guided Histotripsy (tcMRgHt) has also elucidated the essential role MRI can play in guiding these treatments. MR imaging is non-invasive and can provide the high-resolution soft-tissue contrast needed to precisely treat the target of interest. MR images can also be sensitized to various contrast mechanisms that could prove valuable for assessing the damage caused by histotripsy [1, 2, 3, 31]. The main objective of this thesis is to develop MRI methods to facilitate histotripsy therapies of the brain. There are three main roles that MRI can play to guide histotripsy: Pre-treatment targeting, real-time therapy monitoring, and post-treatment evaluation.

Chapters 3 and 4 discuss methods to accurately perform pre-treatment histotripsy targeting using MR-ARFI and MR-thermometry [31, 32]. These two methods estimate the histotripsy treatment focal region by using low-pressure sonications while encoding a temperature change or tissue displacement. Then, the targeting error is estimated by performing histotripsy treatment at the target location and comparing the estimated foci from the two methods against the actual lesion location. We performed these experiments on 12 tissue samples and found the mean absolute errors along the transverse/longitudinal axis of 2.06/2.95 mm and 2.13/2.51 mm for MR-ARFI and MR-thermometry, respectively.

Chapter 5 discusses the strategies to monitor histotripsy treatments in real-time using MRI. Many MR-visible contrasts are generated by the histotripsy cavitation events and the dynamics that follow these events. We show that the image magnitude and phase provide complementary information about the lesion. First, a rapid increase in the random motion within the lesion causes a magnitude signal loss, which increases with the histotripsy pulses until the lesion is completely liquified. Second, the image phase encodes the histotripsy-caused local radiation force effect, which is shown to be in the direction of ultrasound propagation. Real-time monitoring of transcranial histotripsy treatments is demonstrated by

treating *ex-vivo* bovine brain through an excised human skull.

Chapter 6 discusses the changes in the MR-visible parameters as a function of histotripsy dose in the brain. T1, T2, and Apparent Diffusion Coefficient (ADC) parameter maps were acquired for various histotripsy dose levels. Although the T2 and ADC changed with histotripsy dose, only the ADC values depicted a dose-related increase. Histotripsy lesions mostly contain broken-down tissues. All the cellular matter is exposed in the intracellular space. This change causes an increase in the Apparent Diffusion Coefficient (ADC) of the lesion compared to the baseline ADC level. The mean ADC increased by $6.5 \times 10^{-4}\,\mathrm{mm}^2/\mathrm{s}$ with complete liquefaction of the brain tissue.

Chapter 7 concludes the thesis with a review of the contributions made in this dissertation and discusses the challenges and suggestions about future work in MRI technology to progress tcMRgHt.

CHAPTER 2

Background

2.1 Histotripsy

Histotripsy is a FUS based therapy [108] that uses ultrasound cavitation to briefly excite the air pockets intrinsically dissolved in liquids (such as water present in animal tissues). When an ultrasound wave imparts a high negative pressure on tissues that exceeds a tissue-specific threshold, it causes inertial expansion and collapse of these endogenous air bubbles. The localized expansion and collapse phases are then repeated at a low-duty cycle to stretch, strain, and eventually fracture cells and turn them into acellular debris [107].

Histotripsy is typically performed using a 1 to 3 cycle pulse (Fig. 2.1) at a low duty-cycle ($<$0.1 %), but a high peak-negative pressure ($\gtrsim$ 23MPa). Since histotripsy is a cavitation-based treatment method, tissues below the cavitation threshold are virtually unaffected (Fig. 2.1). The low-duty cycle ensures that the time-average energy deposited in the tissue is low and does not cause a significant increase in temperature [28]. There are three types of mechanisms by which histotripsy treatments could be performed [7]. In this dissertation, we only perform intrinsic threshold cavitation-based histotripsy [100].

2.2 MRI

Magnetic Resonance Imaging (MRI) is ubiquitous in hospitals worldwide and is a workhorse of clinical diagnosis. Traditionally, imaging with MRI involves three crucial parts, which I will briefly describe below.

The object is placed in a homogeneous magnetic field called the $\vec{B}_0$ field (typically 1.5 T to 7 T for current clinical scanners). The strong magnetic field polarizes the paramagnetic hydrogen atoms (also called isochromats) in tissues, and the net magnetization experienced by the isochromat (M_0) aligns in the same direction as the $\vec{B}_0$ field. The 'magnetized' hydrogen atoms have an angular momentum associated with the $\vec{B}_0$ field vector, which is

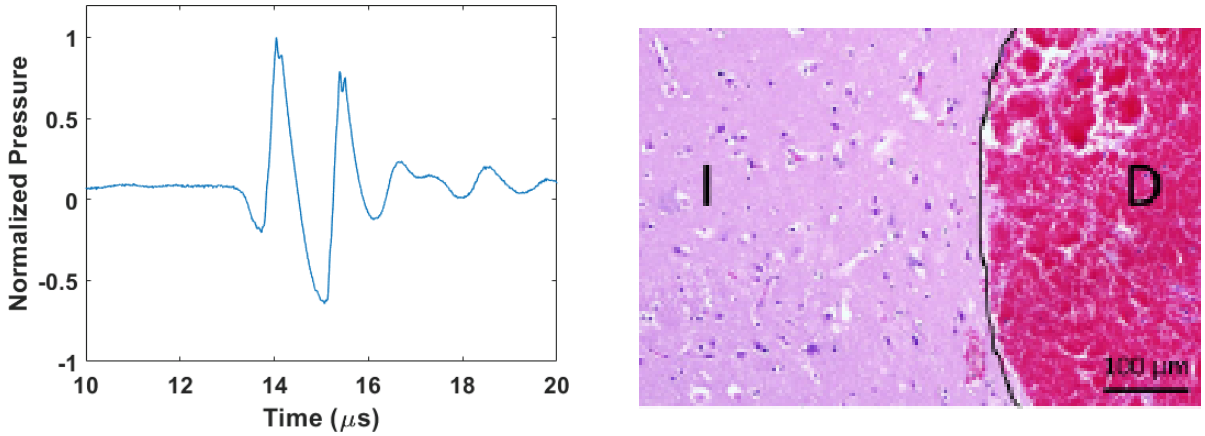

Figure 2.1: Left: Normalized histotripsy waveform. Right: Histology slide showing the precise boundary of histotripsy treatments in an *in-vivo* pig brain. The intact (I) neurons in the untreated region and disrupted (D) acellular debris and red blood cells in the treatment region are separated.

given by the Larmor equation:

$$\vec{\omega} = \gamma \vec{B}_0, \tag{2.1}$$

where γ is a constant called the gyromagnetic ratio, $\vec{\omega}$ is the frequency (called Larmor/resonance frequency) of the spin associated with the hydrogen atom. Typically $\vec{B}_0 = \boldsymbol{B_0}\hat{z}$. For hydrogen atoms $\gamma \approxeq 42.58MHz/T$. So for a 3T MRI scanner, $\boldsymbol{\omega} \approxeq 127.74MHz$.

To get an observable signal from the polarized isochoromats, the magnetization M_0 has to be aligned away from the $\vec{B}_0$ field and along the $\hat{x} - \hat{y}$ axes. This is achieved by playing a circularly polarized RF pulse ($\vec{B}_1$) at the Larmor frequency. For the majority of the $\vec{B}_1$ pulses used in MRI, the area under the $\vec{B}_1$ controls how much the spins 'tip' into the $\hat{x} - \hat{y}$ plane. Once the magnetization aligns to the $\hat{x} - \hat{y}$ plane, it relaxes back to its equilibrium position along $\hat{z}$ by time constant called T1 (2.2), and the transverse magnetization decays with a time constant called T2 (2.3):

$$M_z(\hat{r}, t) = M_0(\hat{r})(1 - (1 - \cos\alpha)e^{-t/T_1}), \tag{2.2}$$

$$M_{xy}(\hat{r}, t) = M_0(\hat{r}) \sin\alpha e^{-t/T_2}, \tag{2.3}$$

where $M_0(\hat{r})$ is the equilibrium magnetization at the spatial location $\hat{r}$, $M_{xy}(\hat{r}, t)$ is the magnetization at time t pointing in the transverse $(\hat{x} - \hat{y})$, and $M_z(\hat{r}, t)$ is the longitudinal magnetization pointing in the longitudinal $(\hat{z})$ plane after the excitation pulse with a tip angle of α in the transverse plane. Note that there are two coordinates associated with a spin: its physical spatial location, given by $\hat{r}$, and the vector denoting where the magnetization

points, given by subscripts x, y, z. While a magnetization component is along the transverse axis, the spins' signal can be measured by the same coil used for transmission or a different set of receiving-only RF coils. The receiving coils then acquire the signal coming from the object irradiated by the $\vec{B}_1$ pulse, which is given by:

$$S(t) = \oint_{\hat{r}} M_{xy}(\hat{r}, t)\, d\hat{r}, \tag{2.4}$$

To make an image of the object, a spatially varying magnetic field is applied along the main magnetic field. This causes a spatially varying precession frequency, which is then recorded by the receiving coil(s). The encoding is done by using RF coils that can independently apply a magnetic field gradient along the three axes. The MRI signal with the effect of the gradient is then given by:

$$S(t) = \oint_{\hat{r}} M_{xy}(\hat{r}, t) e^{-(\int_0^t i\gamma \vec{G}(\tau)\cdot\hat{r}\, d\tau)}\, d\hat{r} = \oint_{\hat{r}} M_{xy}(\hat{r}, t) e^{-i2\pi\vec{k}(t)\cdot\hat{r}}\, d\hat{r}, \tag{2.5}$$

where

$$\vec{k}(t) = \frac{\gamma}{2\pi} \int_0^t \vec{G}(\tau)\cdot\vec{r}\, d\tau.$$

Equation (2.5) is similar to the Fourier Transform of the magnetization, evaluated at the frequency $\vec{k}(t)$, called k-space (Fig. 2.2a).

Practically, MR imaging is performed using different gradients to traverse and sample the k-space, and then an inverse Fast Fourier transform (FFT) is performed to get the image of the object (Fig. 2.2b). There are various ways to fill the k-space, but I will use a spiral acquisition in this work. We use a non-uniform FFT [24] to reconstruct the non-Cartesian acquired images.

Typically, the $\vec{B}_0$ field is not uniform as it is affected by changes in the susceptibility of tissues and air-water interfaces. This $\Delta\vec{B}_0$ can be seen by looking at the phase of the image since it causes the Larmor frequency to change spatially as well, creating a spatially varying phase profile ($\Delta\phi$) that depends on the time at which the image is acquired with respect to the RF pulse (Echo Time, TE). $\Delta\phi$ can also be created manually by playing a gradient. Thus, the image phase can be used as a contrast mechanism in MRI. Two relevant methods that use the image phase are described in Chapter 2.3

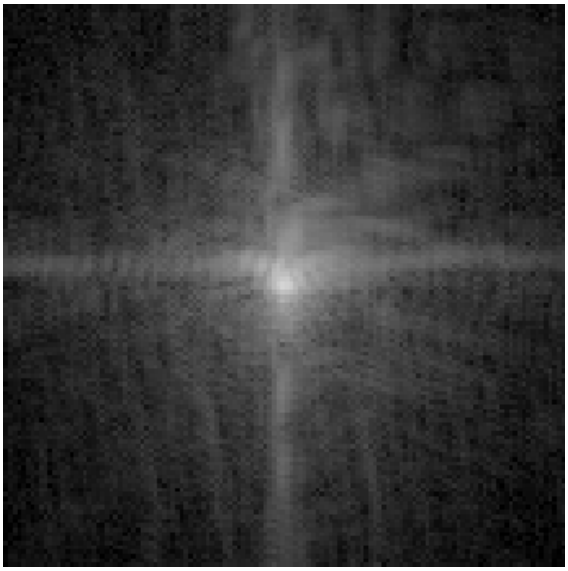

(a) Magnitude k-space of a histotripsy array

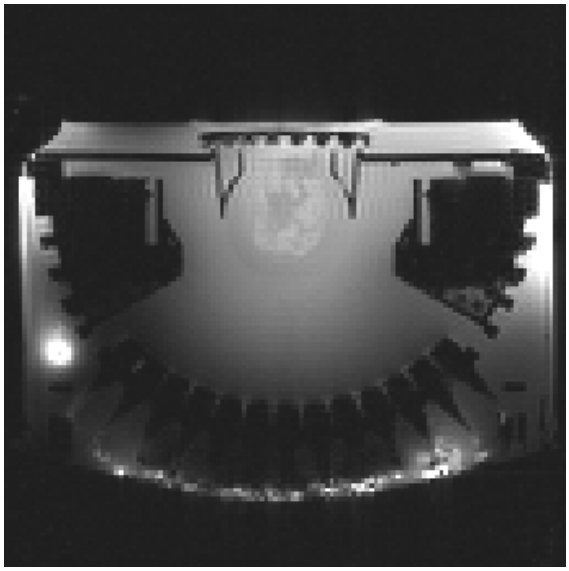

(b) Magnitude image of a histotripsy array

Figure 2.2: Histotripsy array and its k-space.

2.3 FUS and MRI

FUS has been combined with MRI to leverage MRI's superior tissue contrast and capability to sensitize the signal to different contrast mechanisms. Here, I will briefly describe two relevant methods.

2.3.1 MR-Thermometry

Many tissue properties such as the proton-density (M_0), T1, T2, and diffusion coefficient vary with temperature [89]. Temperature also relates to the local $\vec{B}_0$ field experienced by the water molecules. As a water molecule heats up, the Hydrogen bonds weaken, and the neighboring electrons shield the Hydrogen molecules, decreasing the net local $\vec{B}_0$ field [42]. The Larmor frequency can then be given as:

$$\vec{\omega} = \gamma \vec{B}_0 (1 - \alpha T), \tag{2.6}$$

where α is $-1.03 \pm 0.02 \times 10^8/^\circ C$ for $15^\circ C$ to $100^\circ C$ [42]. This linear relation between the temperature (T) and the Proton Resonance Frequency (PRF) causes a phase difference between two images taken at different temperatures. The phase difference image can estimate

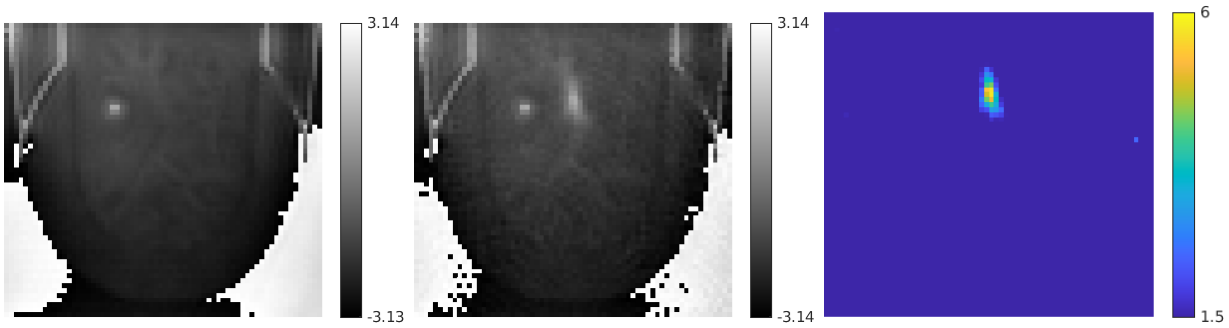

(a) Phase image with no heating (b) Phase image with a temperature increase (c) Phase difference, scaled to get the temperature in $°C$

Figure 2.3: An example of MR-thermometry temperature map estimated from the phase difference of heating-on and heating-off images.

the temperature change by using the following relation:

$$\Delta T = \frac{\Delta\phi}{\gamma\alpha B_0 TE}, \tag{2.7}$$

Figure 2.3 shows magnitude and phase images and the corresponding temperature map estimated using the phase difference images.

2.3.2 MR-ARFI

Ultrasound propagates as a pressure wave that imparts an acoustic radiation force to the medium. The force is proportional to the ultrasound intensity and depends upon the medium's stiffness. MR-Acoustic Radiation Force imaging (MR-ARFI) is a method that can be used to encode this acoustic radiation force caused displacement applied by the FUS array [73]. As described in Chapter 2.2, MR gradients apply a position-dependent $\Delta\vec{B}_0$ field on the top of the main magnetic field. In a standard MR-ARFI experiment, the FUS array imparts a radiation force on the tissue while a gradient is applied simultaneously to encode the displacement caused by the radiation force. The same scan is repeated but with the FUS turned off. The change in phase accrued by the tissue due to the displacement can be written as:

$$\Delta\phi = \gamma\vec{G}t \cdot \Delta\vec{r}, \tag{2.8}$$

Note that the displacement is encoded only along the gradient direction. Using this change in phase, the net displacement during the gradient can be estimated. Figure 2.4 shows magnitude and phase images and the corresponding ARFI displacement map estimated from the phase difference image.

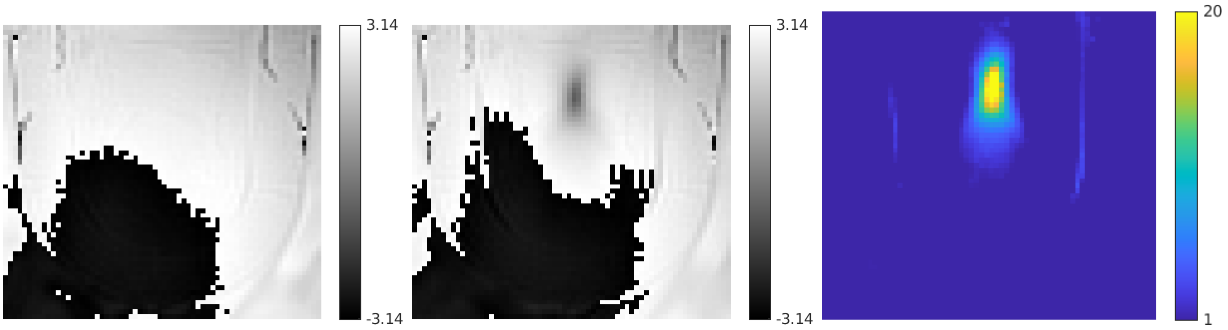

(a) Phase image with no ARFI displacement

(b) Phase image with ARFI encoded with gradient

(c) Phase difference, scaled to get displacement in μm

Figure 2.4: An Example of MR-ARFI displacement image estimated from the phase difference of US-on and US-off images.

CHAPTER 3

Histotripsy Pre-Treatment Targeting using MR-thermometry

3.1 Introduction

Transcranial MR-guided Focused Ultrasound (tcMRgFUS) uses external ultrasound energy focused through the skull to create local heating for thermal tissue ablation. tcMRgFUS has been used clinically to treat essential tremor [22, 77]. However, due to the potential concern for overheating of the skull, tcMRgFUS is limited to treating a small volume in the center of the brain [72, 15]. Using microsecond-length, high peak negative focal pressure ($P^- < -26MPa$) ultrasound pulses through the skull, transcranial histotripsy has been shown to generate controlled and confined cavitation to mechanically destroy targeted brain tissue [94, 65]. Histotripsy minimizes heating by using a very low duty cycle ($< 0.1\%$), while maintaining effective therapy. This allows transcranial histotripsy to potentially treat a wide range of locations and volumes in the brain [94, 101].

Histotripsy typically uses ultrasound imaging for treatment targeting and monitoring, because histotripsy-generated cavitation is easily visualized by ultrasound imaging [38]. However, for transcranial MR-guided histotripsy (tcMRgHt) brain treatment, ultrasound imaging is not practical due to the presence of the skull. MRI guidance is desirable, as MRI is the gold standard for the diagnosis and post-therapy follow-up for many brain pathologies. Recently, our lab has designed and built an MR-compatible transcranial histotripsy system [65]. This system was used to treat *in-vivo* intact pig brain through an excised human skull [66]. However, in that study, a stereotactic approach was used with fiducial markers for targeting. An MR-based, non-invasive targeting method for transcranial histotripsy would be desirable.

MRgFUS heating therapies also use low-temperature heating and MR-thermometry for

This chapter has been published in Ultrasound in Medicine and Biology (UMB)[31].

pre-treatment targeting. Commercial MR-guided HIFU systems such as the Sonalleve V2 by Profound Medical for the treatment of osteoid osteoma [92] and uterine fibroids [104] and Exablate Body by Insightec for the treatment of uterine fibroids and bone metastasis use this method for pre-treatment targeting [47, 58]. tcMRgFUS thermal therapy uses MR-thermometry for pre-treatment targeting [48, 87] and treatment monitoring [89, 82, 45, 86]. For pre-treatment targeting, the focal region is heated by a few degrees Celsius, keeping below the damage threshold, and visualized in real-time using MR-thermometry to confirm the location of the treatment region [48]. Low temperature pre-treatment targeting is used in both the Sonalleve V2 system, as well as the ExAblate System, for transcranial treatments [21, 72]. The low-temperature heating for the MR-thermometry targeting approach works well for tcMRgFUS since both pre-treatment targeting and treatment are performed via ultrasound heating. Another alternative for tcMRgFUS pre-treatment targeting is MR-Acoustic Radiation Force Imaging (MR-ARFI), which sensitizes contrast to the displacement induced by radiation force from the absorption of the ultrasound beam [73, 40, 13, 49, 70]. The displacement from ultrasound radiation force is very small and transient (e.g., one micron over less than a second), but recent studies have shown high spatio-temporal resolution MR-ARFI images [110, 19] in tissue phantoms. Hardware requirements for MR-ARFI are similar to those for MR-thermometry. In this study, we investigate the ability of MR-thermometry to

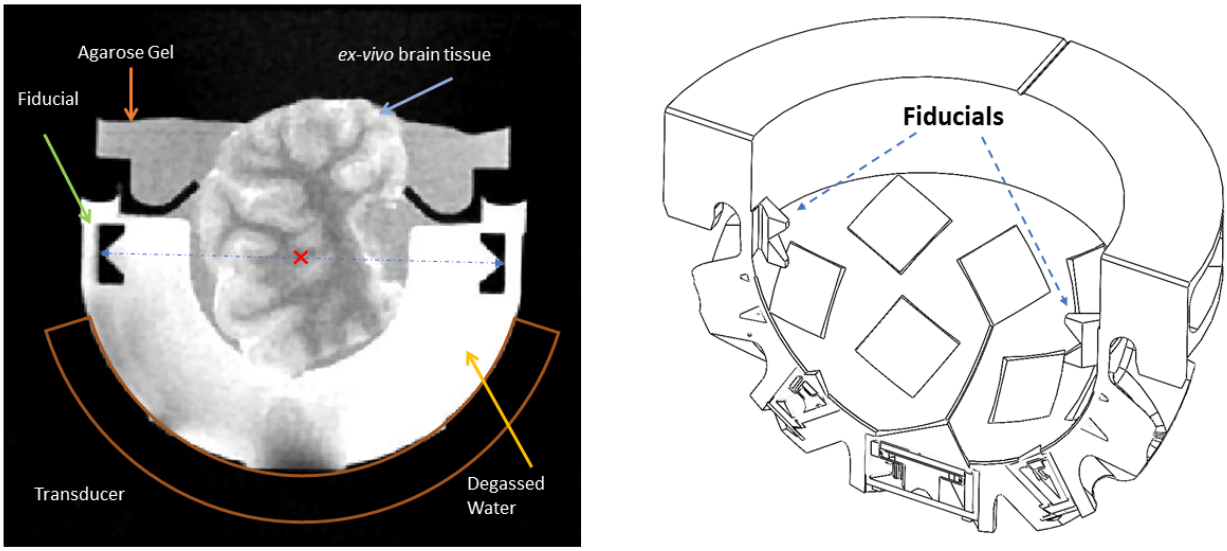

Figure 3.1: Left: T2-weighted image of the experimental setup inside the MR scanner. Right: Cross section image of the array. The transducer was constructed such that the mid point drawn from the two fiducials estimates the geometric focus of the array.

predict focal locations generated from histotripsy treatments. Even though MR-thermometry for tcMRgFUS is well established, there are technical challenges that need to be addressed

when it is applied to histotripsy. First, ultrasound heating arises from the absorption of acoustic pulses, whereas histotripsy is a threshold phenomenon and occurs by exceeding a pressure threshold. The peaks of the acoustic field for heating and histotripsy may not coincide and needs to be assessed. Second, histotripsy transducers and electrical drivers are designed to generate microsecond-length pulses at very high pressure and low duty cycle ($< 1\%$), minimizing heating. In this work, a modified electrical driver was used to produce both low-temperature heating and histotripsy.

To test the feasibility and accuracy of using MR-thermometry for pre-treatment targeting of histotripsy, we designed and constructed a 15-element MR-compatible histotripsy array (Figure 1) with a modified electrical driver capable of both histotripsy and low-temperature heating and quantified the accuracy of MR-thermometry for histotripsy pre-treatment targeting. This system was designed using a similar f-number and frequency to a transcranial array designed for human experiments [66]. Because the 15-element array is not powerful enough to produce cavitation through the skull, the testing was done in the *ex-vivo* bovine brain tissue without a skull. Even in the absence of the skull, any discrepancy between the thermometry focal location and histotripsy lesion location can still be evaluated.

3.2 Materials and Methods

3.2.1 Histotripsy transducer and drivers

All experiments were performed using a custom-built, 15-channel, 750 kHz hemispherical array (Fig. 3.1) with a 50 mm focal radius and an f-number of 1. The array was designed to be a water-tight container while keeping a small footprint, to ensure a small Field of View (FOV) on MR images. The array focal zone has a Full-Width Half Maximum (FWHM) of 3 mm in the longitudinal and 1.2 mm in the transverse planes in free-field. The same driving electronics were used to produce both histotripsy and heating acoustic waveforms.

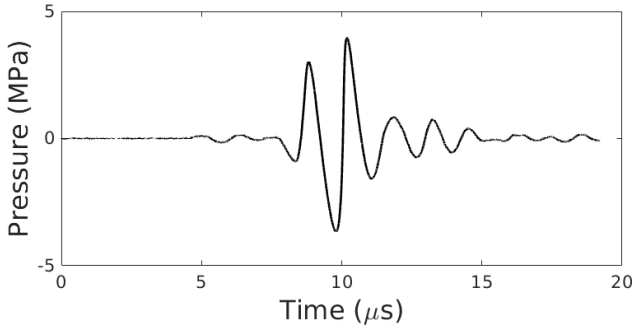

Figure 3.2: Free field pressure waveform from 1 transducer element at the array focus.

3.2.2 Experimental Setup

Seven *ex-vivo* bovine brain tissues were harvested from a nearby slaughterhouse and stored under refrigeration in 1 % benzalkonium chloride solution prior to use (within 1 week). Immediately prior to the experiments, the tissues were degassed in a vacuum chamber and set in 1.5 % agarose gel to ensure that there was no bulk displacement throughout the duration of the experiments (Fig. 3.1).

To produce low-temperature heating for pre-treatment targeting, 6 µs pulses (Fig. 3.2) at relatively low pressure (peak negative pressure of 4 MPa) and a high duty-cycle (30 % duty-cycle; equivalent of 50 kHz Pulse Repetition Frequency (PRF) were used. Given the low-pressure and high focal gain sound field, no significant non-linear propagation effects were expected. The tissues were heated for 15 seconds while simultaneous MR-thermometry images were acquired.

To test the precision of MR-thermometry to estimate the histotripsy focus, we created the smallest histotripsy lesions that were readily visible on MRI. Histotripsy was delivered using 6 µs pulses at high pressure (estimated peak negative pressure of 54 MPa) and a low duty cycle (0.3 %; equivalent of 50 Hz PRF). The array focus was electronically steered to a 3 mm × 3 mm × 2 mm grid with 100 pulses per focal location and 0.5 mm × 0.5 mm × 1 mm spacing between adjacent focal locations.

3.2.3 MR Thermometry Pre-Treatment Targeting

All MR images were acquired on a GE MR750 3 T scanner (GE Healthcare, Waukesha, WI) using a 32-channel head array (Nova Medical, Wilmington MA). MR-thermometry was performed using a gradient-recalled echo (GRE) scan with a spiral acquisition. The slices were centered at the focus estimated using the fiducials placed on the array (Fig. 3.1). MR-thermometry scan parameters were: flip angle: 60°, TE/TR: 30 ms/1000 ms, 13 cm FOV, 10 slices, 2 mm slice thickness, 128 × 128 matrix size, and 4 shots. Thus, the temporal resolution was 4 s and spatial resolution was 1 mm for the imaging plane and 2 mm in the slice direction. Conjugate phase reconstruction was used to reconstruct the images with reduced off-resonance distortions [81]. Fourier interpolation was applied to resample the images to a 256 × 256 matrix size.

Drift correction was applied to the phase-difference images by calculating the mean phase difference from a region outside of the heating zone and subtracting it from the entire image. The precision of temperature measurement from MR-thermometry was estimated by measuring the temperature change in the tissues with no heating applied.

To estimate the targeting location from the heating map on MR-thermometry images,

an ROI that contained the heated region was selected and interpolated to a 4x finer grid. Then a 2D Gaussian surface was fitted to the temperature values. The peak of the fitted Gaussian was estimated as the heating focus (Fig. 3.3). To make the Gaussian fit robust to noise, moving averages of three heating map images were taken before estimating the fit. To reduce the effect of thermal diffusion altering the location of the estimated target, the fit was calculated from the earliest image during heating where a temperature change was easily observable. This was done by measuring the SNR of the heated region and using the earliest time point within 90% of the maximum SNR to fit the Gaussian.

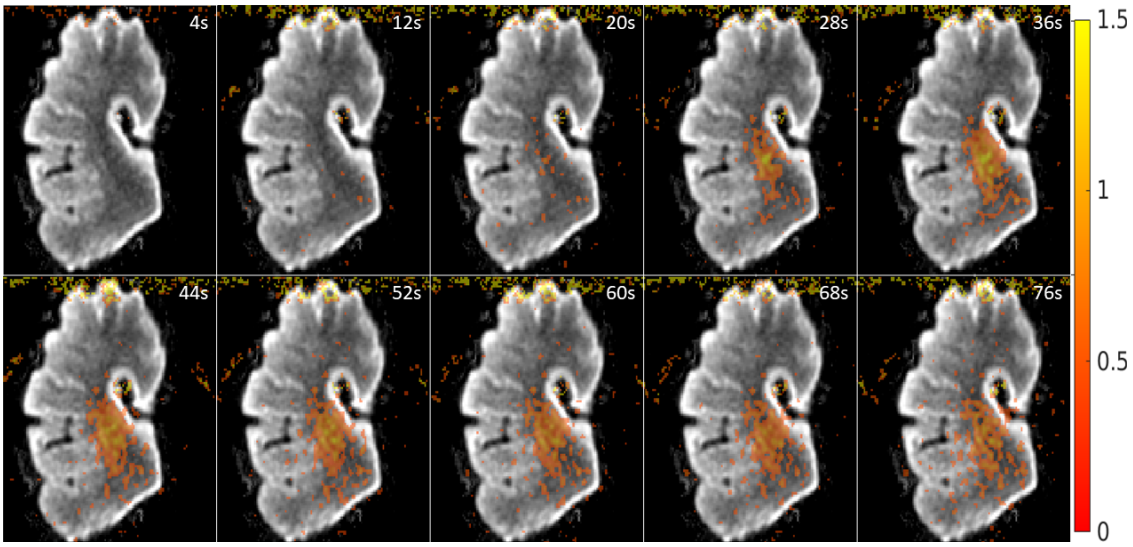

Figure 3.3: Time series display of MR thermometry for 1 slice at every other time point. Heating starts at 28 s and ends around 40 s. With longer heating times, diffusion effects spread out the heating zone.

3.2.4 Estimation of Array Geometric Focus

A set of fiducials were placed on the histotripsy array housing, such that the mid-point estimated from the two fiducials approximate the geometric focus of the array (Fig. 3.1). Both MR and ultrasound factors will contribute to errors in the estimated array focus. Since the histotripsy lesion was produced at the geometric focus, the difference between the focal location measured by the fiducial markers and the location of the lesion generated by histotripsy on the MR image was measured to assess the focal position shift due to non-linear ultrasound propagation with the high-pressure histotripsy pulses and acoustic aberration. Since the MR-Thermometry estimated focus is assumed to overlap with the fiducial geometric focus, the difference between the MR-thermometry targeting location and the geometric focus location estimated from the fiducial markers on MR images was

measured to evaluate the inaccuracy mainly due to MR-related factors (e.g., non-uniform gradient distribution across the field of view, noise in Gaussian fit).

3.2.5 Targeting Accuracy Evaluation

To measure the accuracy of MR-thermometry pre-treatment targeting, the target location estimated from MR-thermometry was compared to the central location of the histotripsy lesion measured from post-treatment MR scans. Pre and post-treatment T2-weighted, T2*-weighted, and diffusion-weighted imaging (DWI) scans were used to visualize the histotripsy lesion. The imaging parameters for T2*-weighted images were: Spoiled GRE with TE/TR: 10 ms/300 ms, FOV: 13 cm, Slice thickness: 2 mm, Matrix size: 192×192, and Flip Angle: 42°. T2-weighted images were acquired using Fast Spin Echo with TE/TR: 66 ms/3 s, FOV: 13 cm, Slice thickness: 2 mm, Matrix size: 192×192, and Echo Train Length: 19. DWI (b-value=0 s/mm^2 and 1000 s/mm^2) were acquired using a spiral acquisition with TE/TR: 60 ms/2 s, FOV: 13 cm, Slice thickness: 2 mm, Matrix size: 128×128, 4 shots, and 40 averages. Spiral acquisition parameters and reconstruction pipeline was kept the same for the DWI and MR-thermometry scans to ensure that no bias due to image acquisition and reconstruction processes is seen in the estimated focus, although eddy currents due to diffusion gradients could lead to additional distortions that are not accounted for in this method. Since we cannot ensure the lesion to be fully contained within a voxel (partial-volume effect), it was expected to see the lesion visualized in a different number of voxels for each tissue. To estimate the lesion location from post-treatment MR images, all the voxels with hypointense region were identified on DWI images. A center of mass was evaluated from these voxels and designated as the lesion center. To measure the accuracy of targeting, the focal location estimated from fiducials and MR-thermometry targeting location were compared to the lesion center estimated from post-treatment MR by calculating the difference in the location in longitudinal and transverse axes.

3.3 Results

3.3.1 MR Thermometry Pre-treatment Targeting

The tissues were heated to ∼1.6 °C increase (Fig. 3.3) in temperature, as measured by MR-thermometry, using the parameters described in the Methods section. The baseline standard-deviation of temperature change without heating was ∼0.2 °C. Fig. 3.4 shows an example of the MR-thermometry image measuring the heating generated from the modified histotripsy transducer and driver. An ROI is also marked showing the area that was selected

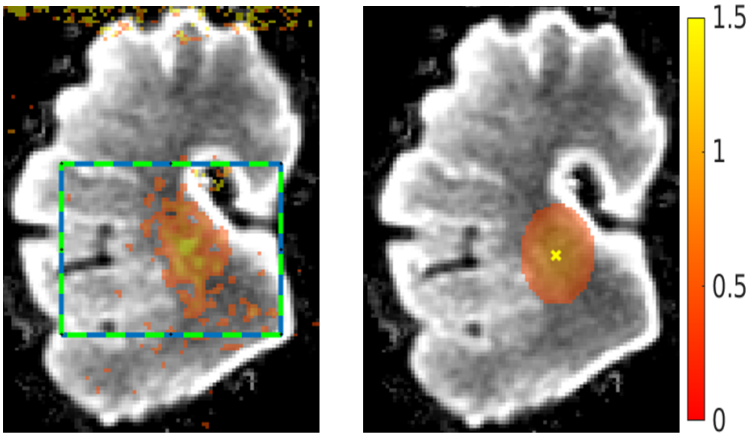

Figure 3.4: MR-thermometry heating image overlaid on b=0 DWI background image. Left: Raw heating image with an ROI that is used to fit the Gaussian. Right: The fitted Gaussian along with the estimated MR-thermometry focus.

to fit a 2D Gaussian over the heating image. An example targeting location estimated by MR-thermometry for this tissue is also shown.

3.3.2 Post-treatment MRI of Histotripsy

Fig. 3.5 shows MR images for a tissue before and after histotripsy treatment. Histotripsy lesions were visualized in all tissues. Lesions were not visible on T2*-weighted scan for any tissue. T2-weighted scans were able to visualize the lesion in most tissues, although the contrast of the lesion was low. Therefore, the post-treatment T2-weighted scan was not used for targeting accuracy evaluation. DW images showed the lesion as a hypointense spot [3] and was easily visible in all tissue samples and was used for determining the histotripsy focal location. Fig. 3.6 shows an example of how histotripsy lesion was estimated on post-treatment DWI scans.

3.3.3 Targeting Accuracy Evaluation

The targeting accuracy was evaluated by measuring the mean and standard-deviation of the absolute difference in the MR-thermometry targeting location and the center of mass of the histotripsy lesion measured using the post-treatment DWI scan (Table 3.1). The absolute mean/standard-deviation difference of the estimated lesion location using MR-thermometry was 0.59 mm/0.31 mm in the transverse and 1.31 mm/0.93 mm in the longitudinal planes, respectively.

To assess the focal position shift due to non-linear ultrasound propagation histotripsy

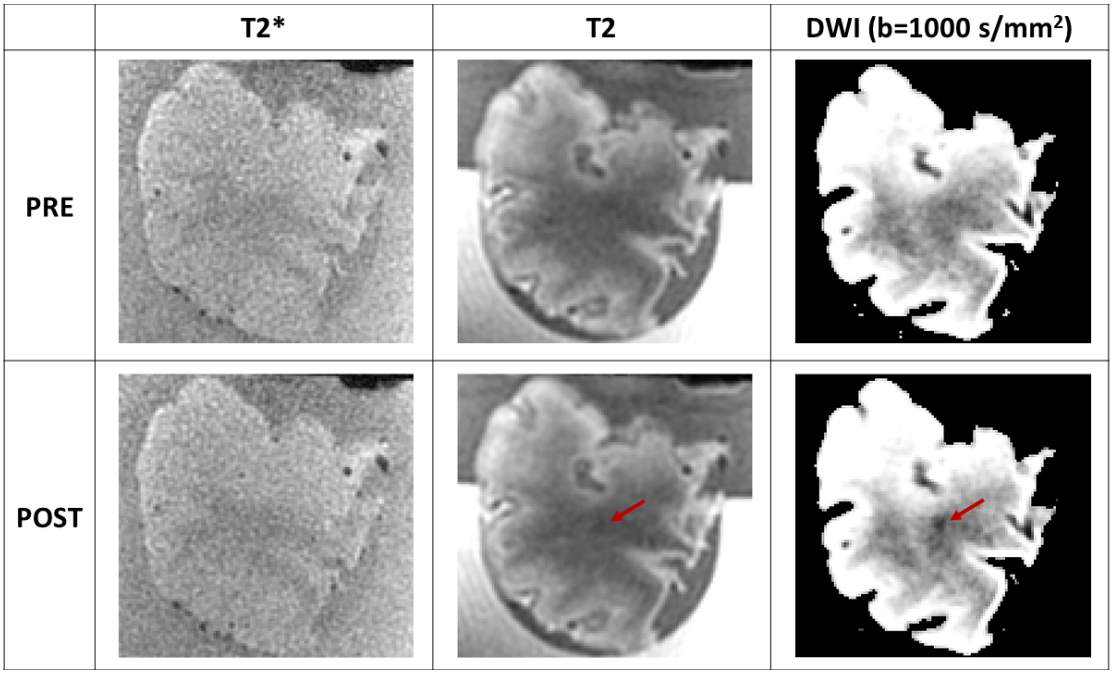

Figure 3.5: T2*, T2 and DWI (b=1000 s/mm^2) images before and after histotripsy treatments. The lesion contrast is best visualized on DWI scan due to homogenization of cellular matter in that region, causing higher diffusion in the lesion compared to the surrounding tissues.

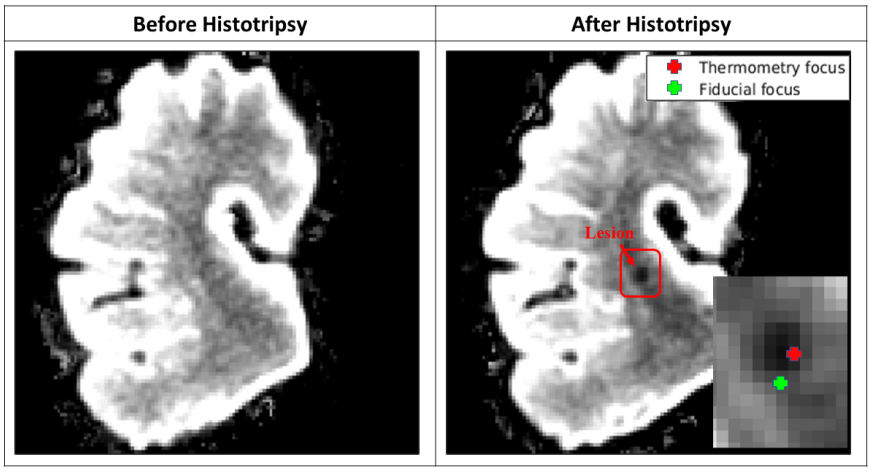

Figure 3.6: Visualizing the histotripsy lesion along with estimated focus from MR-thermometry and fiducials.

pulses and acoustic aberration, the difference between the geometric focal location measured by the fiducial markers and the actual location of the histotripsy lesion on post-treatment MR scan was measured (Table 3.1). The absolute mean/standard-deviation difference between the geometric location measured with the fiducials and the central location of the

Tissue	Difference between fiducial and lesion location (mm)		Difference between MR-thermometry and lesion location (mm)		Difference between MR-thermometry and fiducial location (mm)	
	Transv.	**Long.**	**Transv.**	**Long.**	**Transv.**	**Long.**
1	0	1.3	0.8	1.8	0.7	0.5
2	-0.4	1.7	-0.3	2.3	0.2	0.6
3	-0.2	0.9	-0.5	1.1	-0.3	0.1
4	0	0.4	0.6	-2.3	0.6	-2.6
5	0.3	0.4	0.1	0.1	-0.1	0.2
6	-0.5	0.8	0.9	0.1	1.4	-0.6
7	0.2	1.2	0.9	1.5	0.6	0.4
Mean Abs. Error	0.23	0.96	0.59	1.31	0.56	0.71
St. Dev Abs. Error	0.19	0.48	0.31	0.93	0.44	0.85

Table 3.1: Error in focus estimation. (-) sign is towards the array in longitudinal axis and to the left in the transverse axis. Abbreviations: Transv.: Transverse, Long.: Longitudinal directions

histotripsy lesion measured using the post MR-scan was 0.23 mm/0.19 mm in the transverse and 0.96 mm/0.48 mm in the longitudinal planes, respectively.

The difference between the MR-thermometry targeting location and the focal location estimated from the fiducial markers was measured to evaluate the inaccuracy mainly due to MR-related factors (Table 3.1). The absolute mean/standard-deviation difference between the MR-thermometry targeting location and the geometric focus location estimated from the fiducial markers was 0.56 mm/0.44 mm in the transverse and 0.71 mm/0.85 mm in the longitudinal planes, respectively.

3.4 Discussion

This work shows that MR-thermometry based targeting can successfully predict the location of histotripsy lesions with sub-millimeter precision. We investigated the accuracy of using MR-thermometry for histotripsy targeting by comparing the peak location of a Gaussian fitted to the MR-thermometry map and the center of mass in post-treatment DWI of histotripsy lesions.

This approach has several limitations. First, using different MRI pulse sequences for MR-thermometry and DWI means that issues like susceptibility and motion could cause varying image distortions for different pulse sequences. This could cause shifts in estimated focus that

could be accounted for by performing image registration or by carefully matching acquisition and reconstruction methods. A calibration phantom can be used to evaluate distortions caused by the different pulse sequences. Second, using a Gaussian fit to determine the target location from the thermometry map can be confounded by heat absorption, diffusion, flow, and the ROI selected to estimate the Gaussian. This error can be reduced by using the earliest heating image with high SNR before the heating profile broadens.

We showed that the fiducial marker approach can be used to estimate the ultrasound transducer geometric focus precisely, but its role may be limited for transcranial ultrasound therapy where significant aberrations from the skull might cause more pronounced focal shifts. Additionally, larger imaging FOV with more B0 non-uniformity and gradient non-linearity across the imaging plane could reduce MR fiducial accuracy.

However, there are still other issues with using ultrasound heating for histotripsy targeting. First, heating is affected by thermal diffusion and flow, thus spreading the heating region with time and biasing the targeting location estimate. Second, ultrasound propagation for low-temperature heating is in the linear regime, and thus the effect of aberrations on the focal shift may be different in the case of non-linear propagation in histotripsy, although this difference may be small, as transcranial histotripsy transducers have a very low f-number and ultrasound beams do not overlap significantly until they get close the focal regions. Third, for tcMRgFUS experiments, it has been observed that getting focal heating is more difficult closer to the skull. Thus, using MR-thermometry for pre-treatment targeting in shallow regions might be difficult.

In this study, we showed that in the case of limited aberration, MR-thermometry can be effective for pre-treatment targeting for histotripsy. In future studies, we plan to modify the driving electronics to the 360-element, 700 kHz hemispherical transcranial array designed for human use, which will be able to perform aberration correction through the skull and electrical focal steering. We will also explore the effects of skull aberration on the accuracy of this method. The precision of using MR-thermometry targeting for histotripsy with electrical steering also needs to be investigated. The larger transcranial array allows for steering and more pressure output than the array used in this study. Another way of performing pre-treatment targeting is by using MR-ARFI to measure acoustic pressure directly, which may provide a better targeting accuracy than MR-thermometry, as it takes the non-linearity into account and will be investigated in the future. The modifications to our drivers for performing both heating and histotripsy also allow them to perform radiation force sonications. Another benefit of using MR-ARFI is that it can be used for aberration correction prior to histotripsy sonications [40].

3.5 Conclusions

The safety and accuracy of tcMRgHt rely on pre-treatment targeting guidance. In this study, by using driving electronics capable of performing low-temperature heating and histotripsy, we demonstrate the feasibility of using MR- thermometry to provide sub-millimeter accuracy for pre-treatment histotripsy targeting. In future studies, we will implement the modified driving electronics to the human-scale, 360-element hemispherical transcranial histotripsy array and explore the effect of skull aberration as well as electrical focal steering on the performance and accuracy of MR-thermometry for pre-treatment histotripsy targeting.

CHAPTER 4

Histotripsy Pre-Treatment Targeting using MR-ARFI and MR-thermometry

4.1 Introduction

Histotripsy is a non-invasive, focused ultrasound (FUS) treatment method that uses high pressure ($\gtrsim 20MPa$), short (1-2 cycles) ultrasound pulses at low duty-cycle ($\leq 1\%$) to mechanically disrupt the target soft tissues via acoustic cavitation [71, 108, 107]. It has been proven effective in various tissue types in preclinical studies [99, 101, 103] and was recently approved by the FDA for the non-invasive treatment of liver tumors. Histotripsy has also been shown to stimulate local and systemic immunological response in rodent tumor models and abscopal effect (reduction of off-target tumors) in human case reports [88, 106, 99]. Transcranial histotripsy has been shown to treat the target brain tissues through an excised human skull without causing significant heating of the skull [27, 94]. Recently, Transcranial MRI-guided histotripsy (tcMRgHt) studies have demonstrated MRI as a viable tool for guiding and monitoring transcranial histotripsy treatments [66, 65, 31].

Treatment planning for histotripsy treatments in the abdomen region, such as liver and kidney, involves taking pre-treatment CT and MRI scans to locate the treatment region [99]. During treatment, an ultrasound imaging probe co-aligned with a histotripsy array is used to monitor the histotripsy treatment in real time since cavitation bubble clouds show hyperintense contrast in B-mode ultrasound images [38]. For the brain application, as ultrasound imaging cannot image through highly aberrating human skulls, MRI guidance is currently being investigated for histotripsy targeting and monitoring. Transcranial MR-guided histotripsy (tcMRgHt) employs pre-treatment MRI scans to delineate the treatment region of interest (ROI) by co-registering the histotripsy transducer's focal region coordinates and the MRI coordinates. This work aims to assess the use of MR-thermometry [87] and

This chapter has been submitted to Ultrasound in Medicine and Biology[33]. Portions of this work have been presented at the 33rd Annual Meeting of ISMRM[32]

MR-acoustic radiation force imaging (MR-ARFI) [73] to visualize the histotripsy transducer focal zone and the accuracy of these two MRI-based pre-treatment targeting methods for histotripsy treatments.

MR-thermometry and MR-ARFI are routinely utilized in high-intensity focused ultrasound (HIFU) thermal and blood-brain-barrier opening (BBBO) studies [18, 44, 78, 89]. MR-thermometry is used with low-temperature heating to perform pre-treatment guidance for thermal ablation. This works well because the treatment and targeting methods use the same physical mechanism (ultrasound absorption causing temperature change). Alternatively, MR-ARFI uses milliseconds-long ultrasound bursts to displace the tissue a few microns, which is characterized by MRI to perform targeting for both thermal and BBB opening studies. MR-thermometry provides additional information about thermal dose while the treatments are performed [9, 14, 82, 98]. MR-ARFI-based elastography methods have also been used to estimate tissue elasticity changes during thermal therapies [9].

MR-thermometry has been tested for histotripsy pre-treatment targeting, but not through the skull [31]. MR-ARFI has not been tested for histotripsy pre-treatment targeting. In this paper, for the first time, MR-thermometry and MR-ARFI are evaluated for pre-treatment targeting of histotripsy with and without the skull. The accuracy of the two methods is compared at different pressure levels with and without trans-skull sonication. Even though HIFU and histotripsy both use ultrasound, histotripsy uses much higher acoustic pressures with substantial non-linear effects. Therefore, the accuracy of MR-thermometry/MR-ARFI for pre-treatment targeting of histotripsy treatments under high pressures and non-linear propagation is unknown, especially in the presence of the skull.

To perform MR-Thermometry, the driving electronics of the histotripsy array were modified to generate low-temperature heating using continuous waves (CW) at low pressure at the focus for 30 seconds. To perform MR-ARFI for pre-treatment targeting, radiation force push at the array focus was generated by low-pressure bursts with a much longer pulse duration (20 ms) than histotripsy pulses (3 μs). To evaluate the targeting accuracy, a histotripsy lesion was created and visualized using diffusion-weighted imaging (DWI). The focal location determined by pre-treatment MR-thermometry/MR-ARFI was compared to the centroid of the post-histotripsy lesion on Diffusion Weighted Imaging (DWI) images to determine the targeting accuracy. The targeting accuracy of MR-thermometry/MR-ARFI was assessed at different pressure levels and through an excised human skull.

4.2 Materials and Methods

4.2.1 Experimental Setup

All experiments used a focused, 700 kHz, 128-element MR-compatible histotripsy array (f-number: 0.73, FWHM: 2 mm × 2 mm × 7 mm). The same array has been previously used for our transcranial *in-vivo* histotripsy experiments on pigs [66, 65]. The array was placed in a 3 T GE UHP human MRI scanner (GE HealthCare, Chicago, IL), and 21-channel GE AIR coils were used for receiving MR signals. Treatments were performed on 12 *ex-vivo* bovine brains sourced from a nearby slaughterhouse within 48 hours of resection and refrigerated under degassed saline solution until the day of the experiments. On the day of the experiment, the tissues were degassed and set in 1.5 % agarose gel at room temperature for up to three hours before the experiment. Using a custom 3D-printed insert, the brains were placed centered at the array's geometric focus. The experimental setup inside the MRI scanner is shown in Fig. 4.1.

For the transcranial histotripsy treatment, two human skulls were acquired from the University of Michigan Anatomical Donations Program and were stored under degassed saline. The skulls were degassed under a vacuum chamber for 24 hours before the experiment and held in place using screws mounted on the array. Since the skull significantly aberrates the ultrasound field, a pin hydrophone was used to perform aberration correction by adjusting the phase delays to each array element based on the hydrophone signal measured at the array focus from each element.

4.2.2 Pre-treatment targeting using MR-thermometry

To perform MR-thermometry for pre-treatment targeting, focused heating was generated using continuous wave (CW) ultrasound (100 % duty cycle) for 30 s. For experiments without the skull, the peak negative pressure (P^-) of 4 MPa was measured in the free field (Fig. 4.2) by capturing the pressure waveform while firing the entire array using a fiber-optic hydrophone (Onda HNR-0500, Sunnyvale, CA). Through an excised human skull, the in-situ P^- of 1.2 MPa was estimated, with approximately 70 % ultrasound attenuation through the human skull with aberration correction measured previously. This resulted in spatial-peak temporal-average intensity (Ispta) of 437 W/cm^2 and 40 W/cm^2 for the cases without and with the skull, respectively.

Proton resonance frequency MR-thermometry was performed simultaneously during heating using a 3D RF-spoiled gradient recalled echo (GRE) scan using a stack of spirals acquisition with 8-shots/platter. The scan parameters were TE/TR/FA: 33 ms/39 ms/13°, FOV:

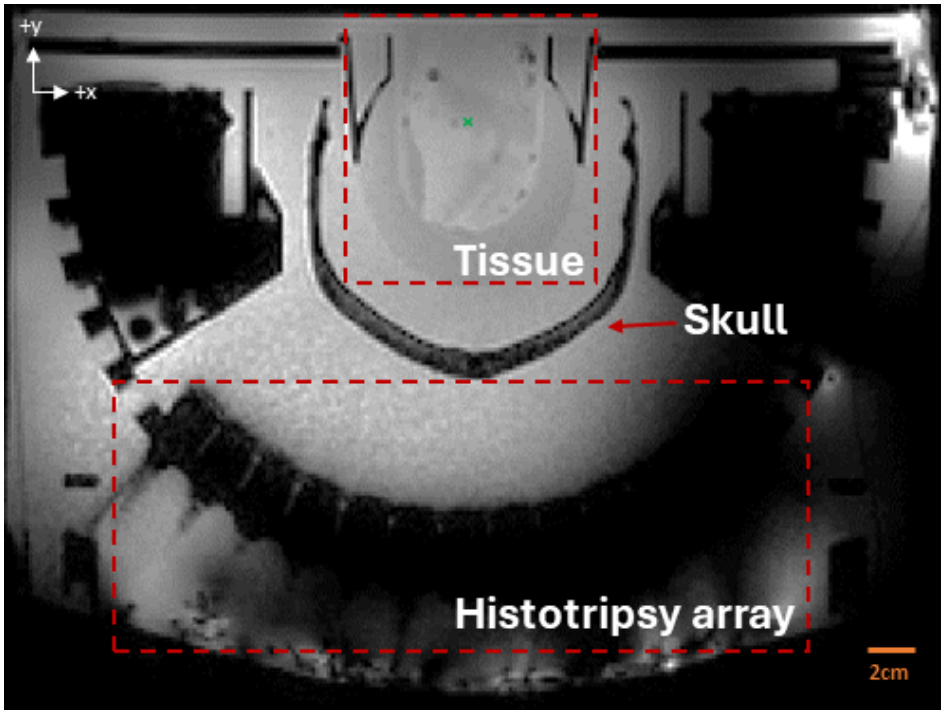

Figure 4.1: T2* weighted image of the array setup inside the MRI scanner. For the scans involving human skulls, the skulls were set in the path of the ultrasound by four mounting screws. The receive coil was placed on top of the tissue to maximize SNR inside the tissue. The green arrow in the tissue marks the array's geometric focus.

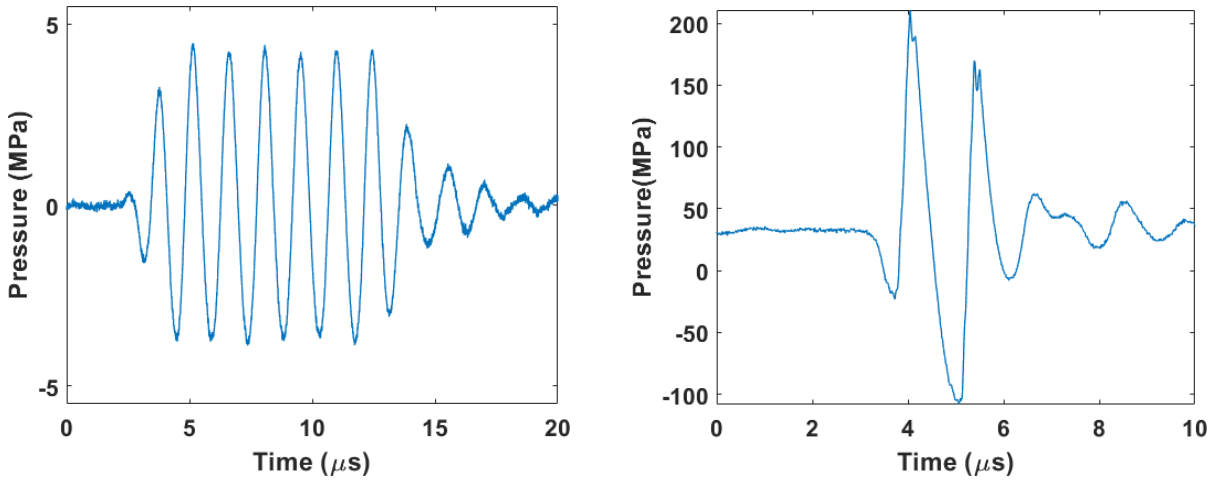

Figure 4.2: Summed pressure waveforms acquired using a hydrophone for (a) MR-thermometry/MR-ARFI and (b) histotripsy experiments from the therapy array. The actual waveform length for MR-thermometry/MR-ARFI was 30sec/20ms, respectively. The same electronic drivers were used to generate these waveforms.

40 cm × 40 cm × 4.5 cm, matrix: 256 × 256 × 15, 4.68 s per acquisition. A field-map-informed conjugate-gradient sensitivity map encoded (CG-SENSE) reconstruction was done using a field map and sensitivity map acquired from a separate scan [23]. Phase difference images were calculated by subtracting the angle of the pre-heating image from the subsequent heating images. Zeroth-order phase correction was done to correct for scanner drift-induced phase changes before estimating the final temperature changes. Under these conditions, the focus of the array was estimated by identifying the hottest pixel during sonication.

4.2.3 Pre-treatment targeting using MR-ARFI

To perform MR-ARFI for pre-treatment targeting, ultrasound radiation force was applied using the 20 ms length pulses at the P^- focal pressure of 5 MPa without the skull and 1.5 MPa through the skull with aberration correction. Each ultrasound pulse was triggered with the ARFI gradient pulse, resulting in a 4° duty cycle. MR-ARFI scan was done using a 3D spin-echo pulse sequence with a stack of spiral acquisition with 8 shots/platter and a pair of bipolar gradients on either side of the 180° pulse, similar to the method described in [51]. The scan parameters were TE/TR: 38 ms/500 ms, FOV: 40 cm × 40 cm × 4.5 cm, matrix: 256 × 256 × 15, 60 s per acquisition. Each gradient in the bipolar gradient had a first moment of 24 G · ms/cm and was oriented along the array's longitudinal axis (scanner y-axis). The ultrasound array was turned on for 20 ms each TR to cover half of both the bipolar gradients along with the 180° pulse [51]. Like MR-thermometry, field map informed

CG-SENSE was also used for reconstructing MR-ARFI images. Three sets of MR-ARFI images were acquired, with the array's state: off, on+, and on-, with the on+ and on- images having opposite polarity of the ARFI gradient to increase the SNR of the averaged phase difference images. Phase difference images were calculated by subtracting the averaged ARFI on images from the ARFI off images and calculating the MR-ARFI 'displacement' images. Phase unwrapping was performed on the phase difference images using the Goldstein method [29]. Like MR-thermometry, the peak of the MR-ARFI images was designated as the focus.

4.2.4 Targeting accuracy evaluation

To evaluate the targeting accuracy, the array focus location based on pre-treatment MR-Thermometry and MR-ARFI images was compared to the estimated center location of the post-histotripsy lesion determined by DWI. Single point histotripsy lesions were generated using 1.5 cycle pulses and 100 Hz Pulse Repetition Frequency (PRF) (0.02 % duty cycle) until the tissue was completely homogenized with a treatment time of two minutes. Histotripsy ultrasound pulse waveform is shown in Fig. 4.2. Pressure waveforms from individual transducer elements were acquired using the fiber-optic hydrophone and summed to estimate the total pressure output from the transducer. Three experimental conditions were tested to examine the impact of pressure levels and skull presence on the targeting accuracy: 1) estimated in-situ peak-negative pressure P^- of 35 MPa without a skull, estimated in-situ P^- of 75 MPa without a skull, and estimated in-situ P^- 36 MPa through the human skulls. Since histotripsy causes cell membrane disruption, lesions show well on DWI images due to the increased diffusion coefficient inside the lesion compared to untreated tissue [1, 3, 31].

The lesions were imaged using a DWI scan (b=0 s/mm^2 and 1000 s/mm^2) with echo-planar imaging (EPI) readout. The scan parameters were TE/TR: 52.6 ms/2 s, FOV: 40 cm×40 cm× 4.5 cm, matrix: 256 × 256 × 15, and 4 shots [53]. Vendor-provided distortion correction was used to correct for EPI image warping. Finally, the DWI images were aligned with the magnitude of the MR-thermometry and MR-ARFI images using MATLAB's `imregister` function using a Mutual Information cost-function to correct for rigid shifts between the three scans. The lesion was identified by comparing the pre- and post-treatment ADC images and determining the lesion area. The lesion voxel with the maximum increase in ADC was then found, and to demarcate the complete lesion volume, the neighboring voxels with an increase in ADC by half the max ADC increase were thresholded to be the complete lesion.

To quantify the targeting accuracy of MR-thermometry and MR-ARFI, the center of mass of the marked DWI lesion was designated as the 'actual' histotripsy target and com-

pared to the center of mass focus identified by the MR-thermometry and MR-ARFI. The difference between the focus coordinates estimated from the two methods, and the estimated histotripsy focus was calculated as the targeting error. A negative error in the longitudinal and transverse axis corresponded to the estimated focus being more distal (+y) and right (+x) of the histotripsy focus, respectively.

4.3 Results

4.3.1 Pre-treatment MR-thermometry and MR-ARFI

MR-thermometry, MR-ARFI, and DWI images could visualize heating, radiation force, and histotripsy lesions in 12 tissue samples. Heating and ARFI focal regions were seen as oblong, elliptical-shaped regions with a tight focal spot (Fig. 4.3). To avoid a shift in the estimated focus due to heat diffusion for MR-thermometry images, the earliest timepoint where the heating spot was visible was used to estimate the focus. The peak temperature change and the peak displacement without the skull were about 8 °C and 20 µm, respectively. Heating temperature uncertainty was estimated to be ∼0.2 °C. The estimated temperature increase generated by the MR-ARFI experiment was ∼1.2 °C.

Histotripsy lesions were visible on the post-treatment DWI image as an elongated hypointense region along the array's longitudinal axis, which was in agreement with the array's longer FWHM along that axis. The heating region shown on MR-thermometry and the displacement region on MR-ARFI is more spread out than the lesion on post-treatment DWI or the focal zone size (Fig. 4.3). For experiments with a human skull, both ARFI and Thermometry peaks were lower intensity and more diffuse compared to the cases without a skull. The peak temperature change and the peak displacement with the skull were about ∼2 °C and 4 µm, respectively.

4.3.2 Targeting Error Estimation

Fig. 4.4 shows the error in the focus estimated from MR-Thermometry and MR-ARFI compared with histotripsy focus estimated from DW images. The mean estimated error across all cases in the transverse/longitudinal axis was 2.06 mm/2.95 mm and 2.13 mm/2.51 mm for MR-ARFI and MR-Thermometry, respectively (Fig. 4.5). For MR ARFI, the mean absolute error in the transverse/longitudinal axis was 2.94 mm/2.07 mm at 35 MPa (n = 4), 2.20 mm/3.86 mm at 75 MPa (n = 4), and 1.10 mm/2.91 mm through the skull (n = 4). For MR-Thermometry, the mean absolute error in the transverse/longitudinal axis was 2.57 mm/1.90 mm at 35 MPa, 2.58 mm/2.74 mm at 75 MPa, and 1.29 mm/2.91 mm through

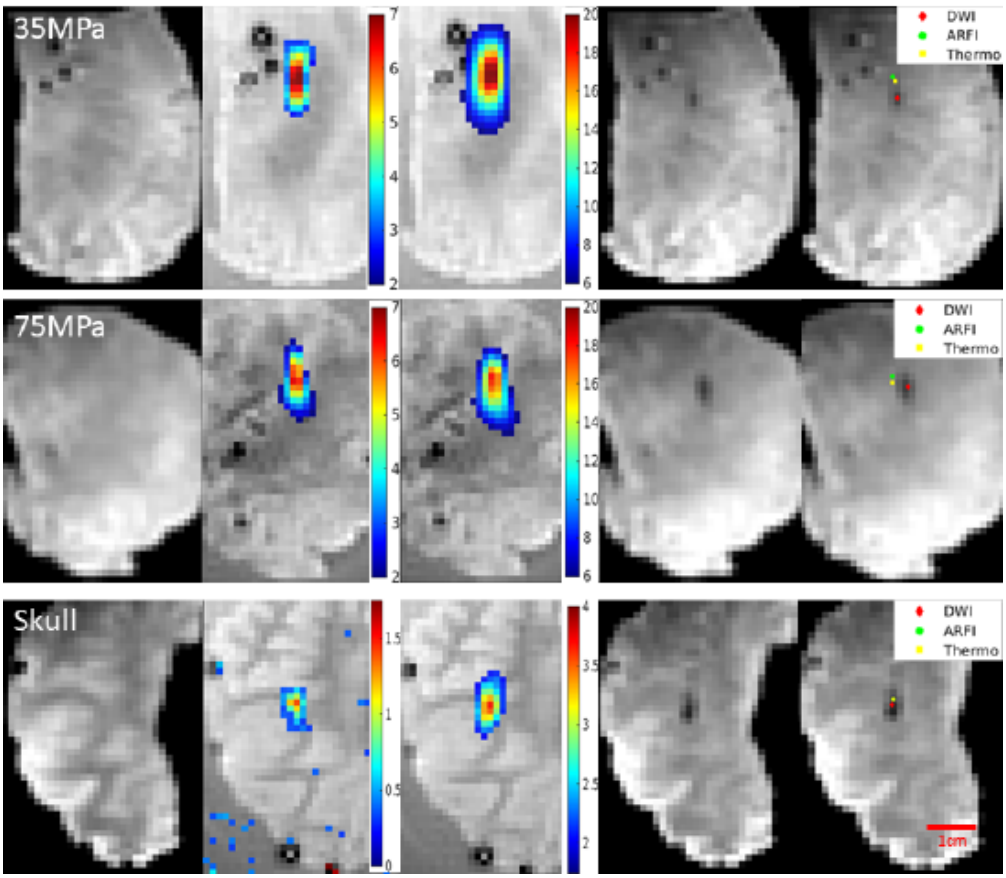

Figure 4.3: From left to right: Example pre-treatment DWI, MR-thermometry (°C), MR-ARFI (μm), post-treatment DWI, and post-treatment DWI labeled with the estimated focus for the estimated peak negative pressure of 35 MPa with a skull (top), 70 MPa without a skull (middle), and 36 MPa with a skull (bottom).

the skull. Since the array focus was elongated along the image top-down axis, there was high uncertainty for estimating focus along that axis (Fig. 4.4).

Fig. 4.5 shows that in the longitudinal direction, the focal location from both MR-based methods was estimated to be more distal from the transducer than the focus estimated from DWI for tissues with higher-pressure treatments. The error in the longitudinal treatment location could be attributed to non-linear propagation effects due to the high-amplitude histotripsy pulses. We found that the uncertainty in estimating the focal location in the transverse axis could be due to the small lesion size, causing a partial volume effect and confounding the focus estimation method. The tissues treated through the skull had a similar range of error values as the tissues treated without the skull.

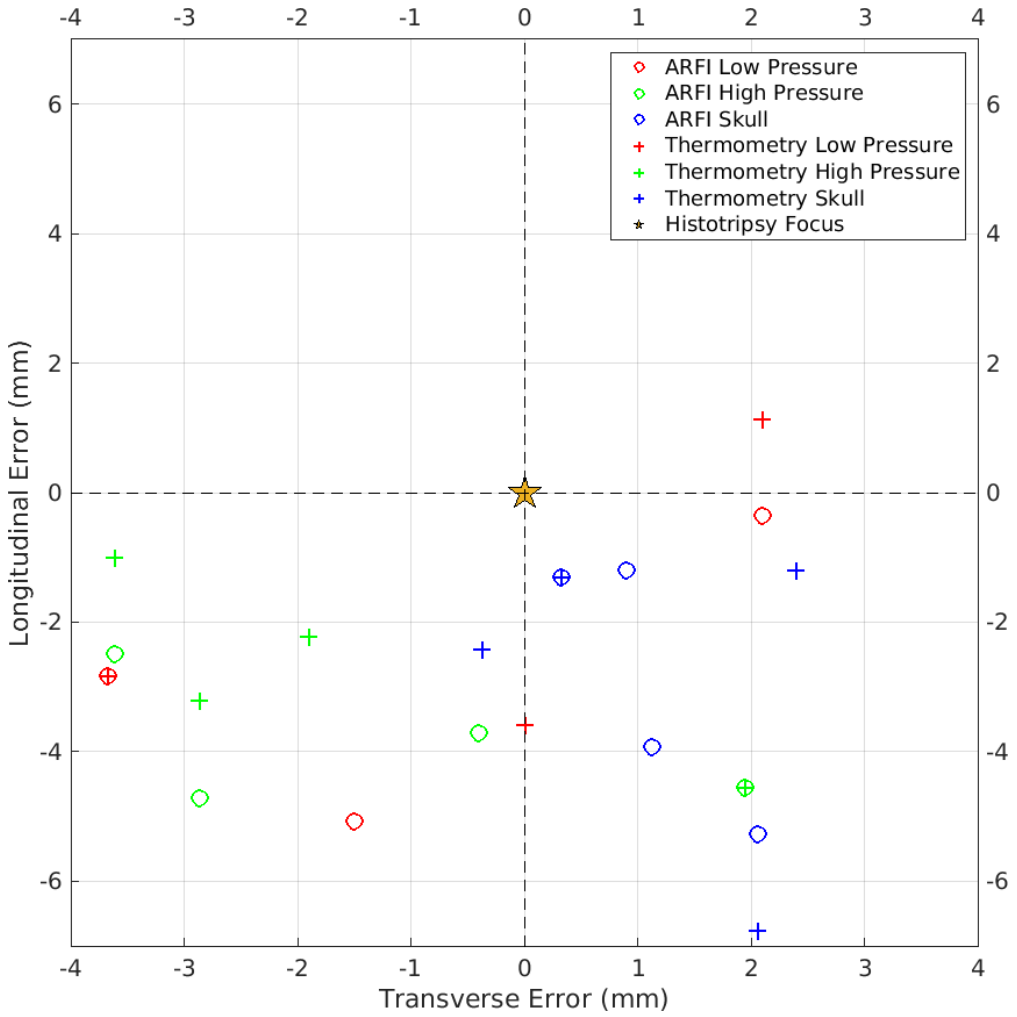

Figure 4.4: Transverse and Longitudinal errors for all the tissues tested in this study. The origin represents the centroid of the DWI-derived histotripsy lesion. The error is skewed away from the FUS array (negative sign on the longitudinal axis).

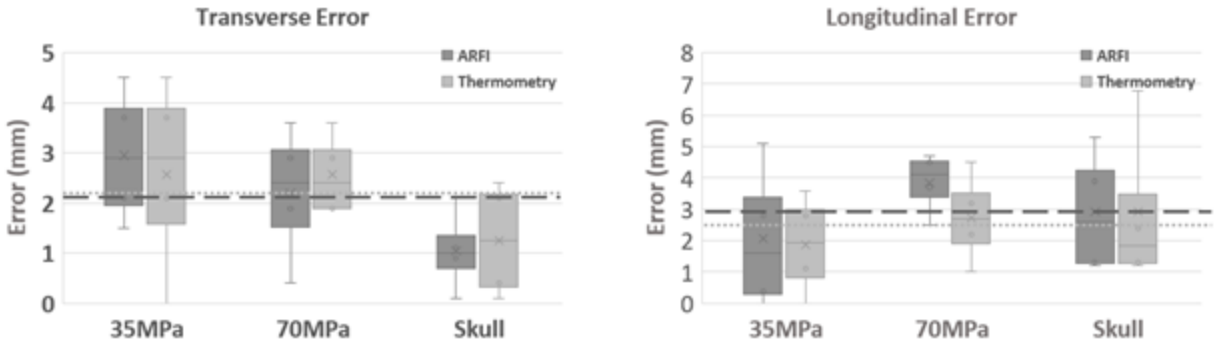

Figure 4.5: Absolute targeting error for MR-ARFI and MR-Thermometry estimated focus. The acquired image resolution was 1.5 mm, and the lesion focus was estimated as the center of mass of the estimated lesion. The dashed/dotted lines mark mean error across all tissue samples for MR-ARFI/MR-thermometry.

4.4 Discussion

Treatment planning for tcMRgHt treatments requires pre-treatment scans to determine the treatment region and prescribe the dose. Ensuring the treatment is delivered at the intended location is a challenging process, which includes registration of ultrasound array to MR scanner, aberration correction, and avoiding unwanted ultrasound 'hot spots'. To combat some of these challenges, we investigated and compared MR-ARFI and MR-thermometry to localize histotripsy treatments on ex-vivo bovine brains on a 3 T human scanner with and without a human skull. Both MR-thermometry and MR-ARFI provided an accurate estimate of histotripsy focus with a worse-case error of less than four imaging voxels. Both these methods explored in this study do not require external devices to perform the targeting task, and the scan times (without any MRI acceleration) are on the order of a few seconds for MR-thermometry to two minutes for MR-ARFI. Although targeting through the skull caused significant pressure attenuation, the focal spot was visible on both MR-ARFI and MR-thermometry after aberration correction. The targeting error through the skull was not increased compared to without the skull.

To perform MR-thermometry and MR-ARFI, the electronic drivers of the histotripsy array needed to be modified to enable long pulses or continuous waves at the lower pressure, as histotripsy transducers are typically designed to be used with microsecond pulses at very high pressures. It should also be noted that the reported pressure through the skull is estimated based on skull attenuation, but it does not account for attenuation due to the brain tissue.

In previous histotripsy experiments, it has been noted that the histotripsy lesion genera-

tion tends to shift pre-focally towards the transducer compared to the geometry focus of the transducer due to the non-linear effect [61]. This non-linear effect becomes more significant at higher pressures. This pre-focal shift contributes to a significant portion of the targeting error, as evident by the higher error in the longitudinal direction towards the transducer (negative error). We investigated the impact of histotripsy pressure on focus estimation by treating tissues at two different pressure levels. At the acquired image resolution, we observed that, on average, the estimated focus at lower pressures is similarly well estimated by the two targeting methods. At 35 MPa, the lesion is smaller, and demarcating the lesion becomes more challenging due to partial-volume effects, causing higher uncertainty in error estimation. At the higher pressure, a larger lesion was generated. Imaging at higher resolution could improve the accuracy of the targeting. This can be done by using pulse sequences that image smaller field-of-view and/or custom-made RF coils with higher signal close to the area of interest.

MR-thermometry and MR-ARFI performed similarly well for all tissues. An added benefit of using MR-ARFI is the potential to perform aberration correction [40, 50, 54, 70]. Although slow, it can provide a good starting point by estimating delays for groups of array elements. These delays can allow us to deposit a few treatment points in the tissue, which can then be used to estimate a new set of delays for all array elements [67, 109]. Using MR-ARFI for aberration correction was beyond the scope of this work and will be investigated in a future study. This study also used brain tissues that were sourced from a slaughterhouse that had varying levels of bleeding and became gassier during the duration of the experiments, which could explain the varying range of estimated errors.

4.5 Conclusion

This study demonstrated the capability of MR-ARFI and MR-thermometry to accurately estimate histotripsy focal region in the presence of a human skull. Histotripsy focus was estimated with mean absolute errors along the transverse/longitudinal axis of 2.06 mm/2.95 mm and 2.13 mm/2.51 mm for MR-ARFI and MR-thermometry, respectively. The presence of the human skull caused the focal region to become more diffuse, but it did not affect the targeting accuracy of either of the two methods. Future work will test the efficacy and accuracy of MR-ARFI and MR-thermometry for histotripsy pre-treatment targeting on *in-vivo* animal models.

CHAPTER 5

Realtime MRI Monitoring of Histotripsy Treatments

5.1 Introduction

Cancers of the brain account for over 250,000 deaths per year worldwide, with over 300,000 new cases reported every year [97]. Current treatment options for patients are surgery, radiation therapy, or chemotherapy. Craniotomy-based surgery is the most common treatment option used, but it exposes patients to risks of infections, surgical trauma, and damage to surrounding cerebral parenchyma [55]. Radiation therapy is usually used to destroy tumors that may remain after surgery but results in necrosis, edema, and reduction in hippocampal cellular activity [30]. Chemotherapy and Blood-Brain barrier (BBB) based therapy are also available but are not widespread [84].

Focused Ultrasound (FUS) is currently being investigated for non-invasively treating brain tumors either by producing thermal necrosis using High-Intensity Focused Ultrasound (HIFU) [17] or by applying low-intensity FUS for the opening of BBB to assist chemotherapeutic treatments [12]. Transcranial MR-guided HIFU (tcMRgHIFU) is approved by the FDA and is clinically used in the brain for the treatment of essential tremors and Parkinson's disease [63, 21, 77]. Human studies of tcMRgHIFU of brain tumors have shown very limited results due to overheating of the skull, long treatment times, inadvertent heating of surrounding tissues, and constrained targeting region capabilities in the brain [17, 72]. Low-intensity FUS BBB opening facilitates the delivery of heavier chemotherapy drugs to the brain by the partial opening of the BBB [12], but there has been limited evidence regarding the safety and efficacy of brain treatment using this approach.

Histotripsy is a non-invasive FUS therapy that uses short, high peak-negative pressure ultrasound pulses to generate focal cavitation [108]. Histotripsy treatments mechanically

This chapter will be submitted to Magnetic Resonance in Medicine (MRM). Portions of this chapter will be presented at the 23rd Annual Meeting of ISTU.

fractionate the tissues into an acellular homogenate that is localized to the region where the peak negative pressure exceeds a cavitation threshold [107, 7]. Histotripsy is FDA-approved for the treatment of liver tumors [99] and is currently being investigated for treatments throughout the body under ultrasound guidance [57]. This work is motivated, in part, by the difficulty in performing transcranial ultrasound imaging.

Recent *in-vivo* animal studies have demonstrated the feasibility of using histotripsy to perform non-invasive brain treatments [94, 27, 65, 20]. Additionally, histotripsy treatments are performed using low-duty cycle (<0.1%) sonications, enabling brain therapy without significant heating to the skull and the surrounding tissue [28]. We have previously performed a transcranial MR-guided histotripsy (tcMRgHt) feasibility study to show that brain histotripsy treatments could be successfully performed inside an MRI scanner [65]. We have also demonstrated that MR-thermometry and MR-acoustic radiation force imaging (MR-ARFI) can be used for pre-treatment targeting these treatments [31]. MR images can also be sensitized to various contrast mechanisms that could prove valuable for assessing the damage caused by histotripsy in real-time [1, 2, 3].

The aim of this work is to perform real-time monitoring of histotripsy cavitation effects in a human MRI scanner with an MR-compatible transcranial histotripsy array using *ex-vivo* bovine brains as a testbed. We first discuss the potential sources of MRI-sensitive contrast generated in real-time by histotripsy treatments. Then, we outline the MRI pulse sequence that was used to sensitize the image to histotripsy cavitation events in real time. Finally, we demonstrate the real-time changes to the image contrast due to histotripsy events in agarose gel and bovine brains and through an excised human skull.

5.2 Theory

Histotripsy cavitation events and the post-cavitation effects are stochastic in nature, and the dynamical changes could range from tens of microseconds to a few milliseconds[7, 107, 76]. As the cavitation threshold is exceeded at the target spot, the high peak-negative pressure allows the air pockets dissolved in the liquid to overcome surface tension and undergo rapid expansion within a few microseconds [103, 7]. The localized air bubbles then dissolve back into the liquid within a few hundred microseconds until the next histotripsy pulse re-excites them [103, 102]. In most cases, the bubble cloud could undergo secondary expansion and collapse cycles before finally returning to equilibrium. The size of the bubble cloud depends on the ultrasound array's frequency and f-number, peak negative pressure, and elasticity of the tissue [75, 76, 100]. This section will briefly discuss the dynamic effects induced by histotripsy bubble clouds and describe how the MRI pulse sequence could be modified to

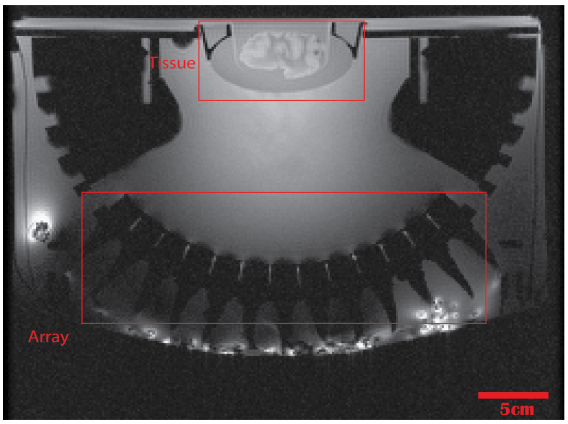

Figure 5.1: Full field-of-view experimental setup inside the MRI scanner. This image was acquired using a spin-warp acquisition used for real-time histotripsy monitoring. The direction of ultrasound propagation is from the bottom to the top axis in this figure (scanner y-axis).

capture these changes.

5.2.1 Random Motion within the Lesion

As histotripsy pulses are delivered to the tissue, the cavitation events break down the tissue's cellular matrix structure. As the treatment progresses, the ablation region gets increasingly liquified until it completely turns into a liquified homogenate [107]. After the collapse of the cavitation bubble cloud, the tissue homogenate rapidly fills up the air cavity, causing chaotic mixing within the lesion that subsides within a few milliseconds [76]. The chaotic motion within the lesion is expected to increase as the tissue becomes more liquified until it reaches a peak value, signifying the complete liquefication of the tissue.

The random motion of the liquid within the histotripsy treatment region can be imaged using MRI pulse sequences sensitized to random motion by using gradients. The random motion within the lesion will lead to an incoherent phase accumulation of the spins, causing a decrease in the magnitude signal. It has been shown that b-values $<0.5\,\mathrm{s/mm^2}$ are enough to visualize histotripsy cavitation events in liquids [1]. Since the cavitation events have short time scales, the relative timing of histotripsy sonications with respect to the gradient waveforms controls the sensitivity of the pulse sequence to histotripsy [1].

5.2.2 Bulk Motion and Acoustic Radiation Force

As the histotripsy bubble cloud expands and collapses, it stretches and strains the tissue. Since the tissue becomes more homogenized with histotripsy pulses, the tissue around the

lesion might get displaced as the treatment progresses. It has also been shown that following the chaotic, random motion of the homogenate, the acellular debris has a coherent motion due to an acoustic radiation force effect [76, 6]. It has been shown that the displacement within the histotripsy lesion due to acoustic radiation force is initially away from the transducer but then rebounds back towards the transducer [75]. The displacement can range from 10-60 microns, most of which lasts 1-15ms after the histotripsy sonication [75].

Only an average effect of the two motion types described above can be imaged with the temporal resolution of MRI. The radiation force-induced displacement can be encoded with an MRI pulse sequence using a gradient timed with the histotripsy treatment. The displacement will be encoded as a change in the image phase, similar to MR-ARFI, which uses CW ultrasound to displace the medium a few microns and encodes the motion using gradients [73]. It is possible that the dynamic change in the phase information could provide information about tissue elasticity changes due to histotripsy[79].

5.3 Methods

5.3.1 Experimental Setup

Histotripsy experiments were performed using a focused, 700kHz, 128-element MR-compatible histotripsy array (f-number: 0.74, FWHM: $2 \times 2 \times 7$ mm^3) [65] using 1.5-cycle pulses at a peak-negative pressure of 70MPa in free field and 36MPa through the human skull. The array was placed in a 3T GE UHP human MRI scanner (GE HealthCare, Chicago, IL) with a 21-channel GE AIR receive coil. The experimental setup is shown in Fig. 5.1.

Experiments were performed on 1.5 % agarose gel and *ex-vivo* bovine brains. The bovine brains were sourced from a nearby slaughterhouse within 48 hours of resection and refrigerated under degassed saline solution until the day of the experiments. The degassed gel/tissue block was placed at the histotripsy array's geometric focus using 3D-printed inserts. To monitor transcranial histotripsy treatments, histotripsy lesion was generated in the *ex-vivo* brain tissues through an excised human skull. The skull was acquired from the University of Michigan's Anatomical Donations Program. It was stored under degassed saline until the day of the experiment and held in place using non-metallic screws mounted on the histotripsy array scaffold.

All monitoring pulse sequences used in this study were programmed using *Pulseq*, which is a vendor-agnostic open-source pulse programming software [56, 80].

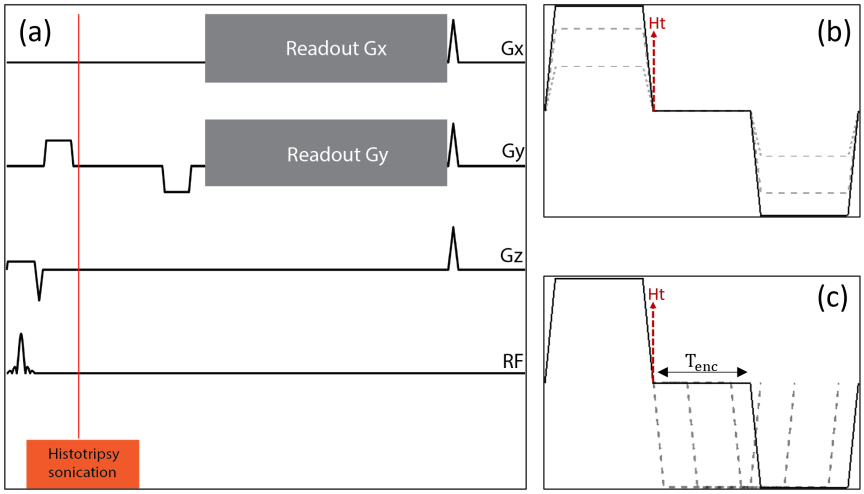

Figure 5.2: (a) GRE pulse sequence with a bipolar gradient along the y-axis. The vertical red lines mark the region where histotripsy sonication was done. For all experiments, only 1 sonication was done every TR. The therapy was sensitized along the y-axis due to the highest expected motion encoded along that axis. (b) Histotripsy encoding gradient with the same encoding time but different b-values of encoding gradients by scaling the two gradients. (c) Histotripsy encoding gradients with varying levels of encoding times. All scans used the same TE/TR values.

5.3.2 Acquisition Protocol

Histotripsy sonications were performed at the array's geometric focus at 10 Hz pulse-repetition frequency (PRF), triggered by the MRI scanner. Treatment monitoring was done using a gradient echo (GRE) pulse sequence with a spin-warp Cartesian acquisition and a 2D spiral non-Cartesian acquisition. The two sequences were modified by placing a bipolar gradient of area 320 mT/m · ms and 4 ms spacing between the gradients along the array's longitudinal axis (scanner y-axis) between the excitation and acquisition blocks (Fig. 5.2, Section 5.7). Although spiral acquisition provides faster treatment monitoring, the advantage of spin-warp acquisition is that the large readout bandwidth inherently reduces susceptibility artifacts and image distortions compared to spiral acquisition. Both the sequences were sensitized to first-order motion due to the bipolar gradient. Histotripsy sonications were initiated by sending a trigger-out from the MRI scanner to the histotripsy electronic drivers. The travel time of ultrasound from the trigger to arrival at the array focus was 100 µs. All the treatments were done with 1 histotripsy sonication per TR.

The acquisition parameters for both the pulse sequences were: FOV: 40 cm × 40 cm, grid-size: 256 × 256, TE/TR: 19 ms/100 ms, flip-angle: 21°, 1 slice with 3 mm slice thickness, 1 histotripsy pulse/TR. The change in the phase was calculated by subtracting the phase from a baseline image before the start of any histotripsy treatment. The images were also

corrected for zeroth-order drift by subtracting the phase of a region in the water bath from the entire image.

5.3.2.1 Cartesian Acquisition

The spin-warp acquisition used a readout bandwidth of 100 kHz. The temporal resolution of the acquisition was 25.6 s. Since 256 TRs were used to generate 1 image, an average of 256 sonications were observed in the magnitude and phase images.

5.3.2.2 Non-Cartesian Acquisition

The temporal resolution used for the spin-warp acquisition in Section 5.3.2.1 is not reasonable for *in-vivo* histotripsy treatment monitoring. Additionally, delivering 256 histotripsy pulses to generate 1 image will lead to the loss of valuable treatment feedback. Treatment monitoring requires high temporal-resolution imaging to ensure the treatment is continuously delivered at the intended location. The spin-warp readout from Section 5.3.2.1 was replaced with a 5-shot spiral-out readout to approach higher temporal resolution imaging. Each spiral acquisition was 27 ms long and acquired at 250 kHz readout bandwidth. The temporal resolution for this scan was 500 ms, allowing more rapid monitoring of histotripsy-induced changes.

A conjugate-gradient sensitivity map encoded (CG-SENSE) reconstruction with a finite-difference regularizer was done using a sensitivity map acquired from a separate scan. Image reconstruction was performed using the Michigan Image Reconstruction Toolbox (https://web.eecs.umich.edu/~fessler/code/).

5.3.3 Sensitivity to Encoding Gradients

The cavitation-induced liquid dynamics change as a function of the treatment dose. To observe the sensitivity of real-time histotripsy images to varying encoding schemes, the encoding gradient amplitude and timing were modified.

5.3.3.1 Effect of Gradient Amplitude

The sensitivity to the motion due to histotripsy sonications was altered by playing the same pulse sequence with varying b-values by scaling the amplitude of the bipolar gradients (Fig. 5.2). Using larger magnitude gradients allows larger sensitivity to histotripsy motion and might sensitize the images to weaker motion at the boundaries of the lesion. Beyond a certain b-value, the lesion contrast would increase without providing new information about the cavitation events.

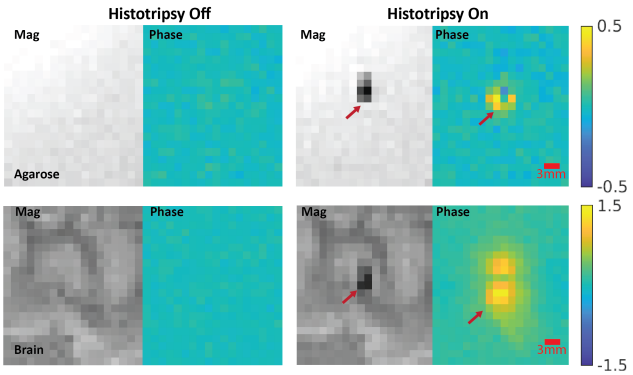

Figure 5.3: Magnitude and phase change due to histotripsy pulses in gel and *ex-vivo* brain tissue using a spin-warp acquisition. The images on the left column have no histotripsy sonication. The images on the right column have 1 histotripsy sonication/TR. The image magnitude decreases, indicating increased random motion within the lesion. The phase difference images show a net phase away from the histotripsy array.

The encoding scheme can also be explained as k-space frequency or phase cycles across the image, as described in detail by Allen et al. [2]. With higher cycles of phase across the lesion, spins undergoing weaker motion can obtain higher frequency dispersion, leading to a loss in signal magnitude. The following b-values were used for this study: 0, 0.5, 1, 5, 10, 20, 30, 40 and 50 $\mathrm{s/mm^2}$ with corresponding k-space frequencies of 0, 13.8, 19.4, 43.6, 61.6, 87.2, 106.8, 123.4 and 137.9 $\mathrm{cm^{-1}}$.

5.3.3.2 Effect of Encoding time

As alluded to in Section 5.2, the acellular matter within the histotripsy lesion is known to initially displace in the direction of ultrasound propagation, then recoils back towards the array. To observe the change in random and bulk motion within the lesion at different time points, the timing of the rephasor gradient was varied with respect to the histotripsy sonication (Fig. 5.2). The net motion at different time points can be estimated based on the phase images. The following spacing between the gradients was used: 0, 0.5, 1, 1.5, 2, 2.5, 3, 3.5 and 4 ms, corresponding to b-values of: 20, 24, 27.5, 31, 35, 39, 42.5, 46 and 50 $\mathrm{s/mm^2}$ and k-space frequency of 137.9 $\mathrm{cm^{-1}}$.

5.3.4 Transcranial Treatment

To validate the feasibility of using the real-time monitoring pulse sequences to monitor *in-vivo* transcranial treatments, a histotripsy lesion was created in *ex-vivo* bovine brain tissue through an excised human skull. Prior to histotripsy sonication, a pin hydrophone was used

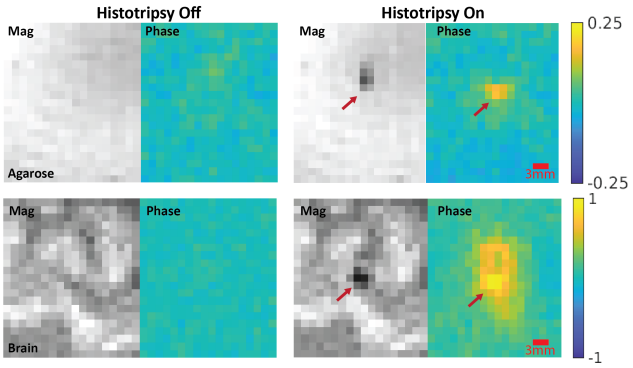

Figure 5.4: Magnitude and phase change due to histotripsy pulses in gel (top) and *ex-vivo* brain tissue (bottom) using spiral acquisition.

to perform aberration correction before performing treatments through the skull.

5.3.5 Comparison with Actual Lesion

After histotripsy treatments are complete, the ablation region contains tissue homogenate. Once the tissue is completely homogenized, additional histotripsy pulses mix the slurry around the ablation region. It is already known that the ablation region has a higher diffusion coefficient compared to intact tissue [3, 31]. A diffusion-weighted imaging (DWI) scan can accurately locate the histotripy ablation region. To correlate the location of real-time histotripsy to the location of the actual histotripsy lesion, the cartesian GRE scan was modified to have a b-value of 1000 $\mathrm{mm/s^2}$ The location of the real-time histotripsy lesion was compared with the post-treatment DWI to estimate the accuracy of the real-time monitoring pulse sequence.

5.4 Results

5.4.1 Monitoring Histotripsy using Cartesian Acquisition

The change in the image magnitude and phase due to histotripsy sonications for GRE scans with Cartesian acquisition is shown in Fig. 5.3. The phase difference images show positive and negative contrasts, indicating a net displacement away (positive) and towards (negative) the histotripsy array. It is important to note that the displacement only occurs when a histotripsy event occurs and not during the treatment 'off' phase. The magnitude decrease signifies the large random motion increase within the lesion due to histotripsy. The magnitude and phase images indicate that the net motion in the center of the lesion is more random but has a

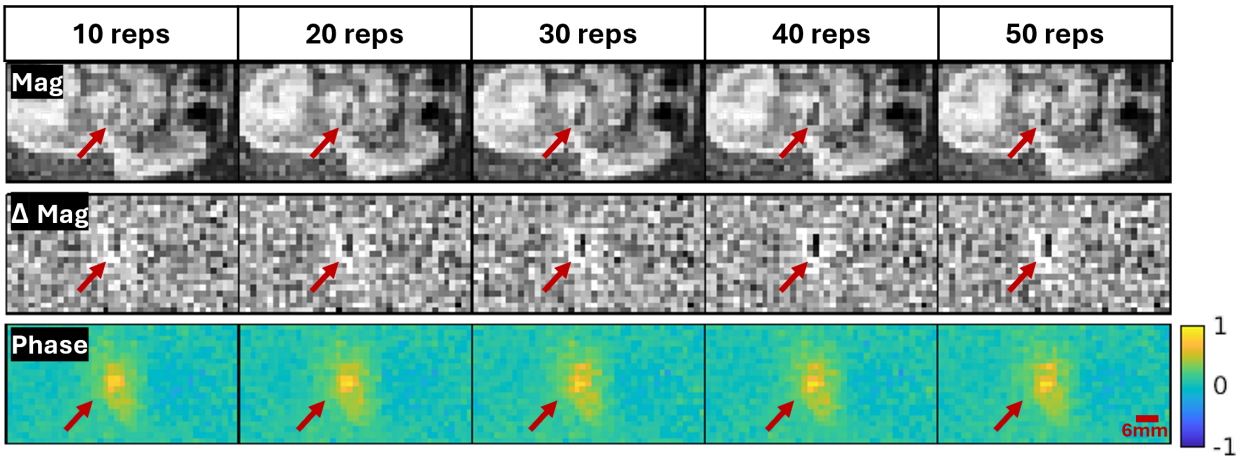

Figure 5.5: Real-time histotripsy images at different points during the treatment. Both the phase and magnitude increase in intensity with increasing histotripsy dose. The increased random motion within the lesion causes the magnitude loss. The phase image contains two regions: the region associated with the magnitude change with a large phase change and the surrounding region corresponding to phase change from multiple possible effects, including ARF, tissue stretching, and shear waves.

bulk shift away from the transducer (as signified by the positive phase difference).

Using the magnitude image, the lesion dimension in the agarose gel was about 3 mm × 6 mm. This lesion size corresponds well with the array's expected bubble cloud size. The relative signal change was higher in the phase images than in the magnitude images for both tissues and gels. The peak signal decrease in magnitude was estimated to be 50 %, and a signal increase in phase was estimated to be 0.3 rad compared to the baseline signal. The phase increase corresponds to an estimated net displacement of about 22 µm away from the transducer. The relative magnitude change in *ex-vivo* brain tissue is similar to the gel, but tissue shows a larger net displacement away from the array due to histotripsy. The phase increase corresponds to an estimated net displacement of about 120 µm away from the transducer. This is possibly due to the brain having higher absorption compared to gel. The estimated lesion size in the tissue was about 3 mm × 3 mm. Although the lesion size is smaller than in agarose, it is known that the bubble cloud expansion in tissues can be restricted due to reduced elasticity compared to a gel [103].

The extent of the phase change in both tissue and agarose was much larger than the extent of expected histotripsy-induced damage. The higher bulk shift in tissue could be associated with bulk motion and radiation force effects in the direction of ultrasound propagation.

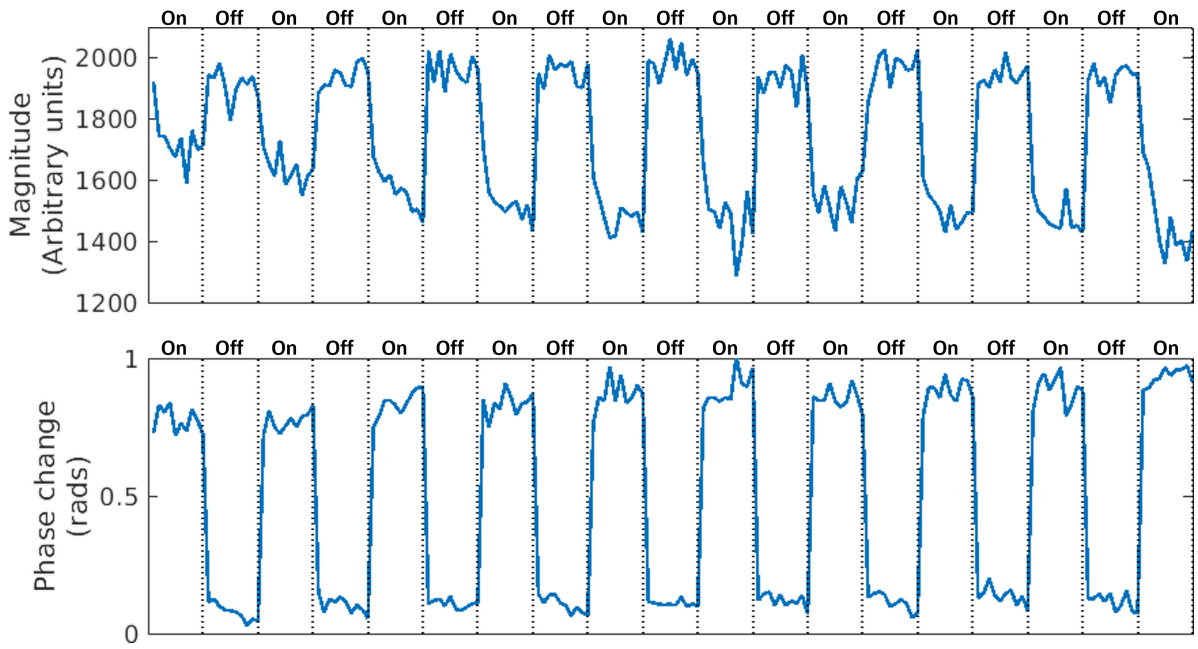

Figure 5.6: Change in magnitude and phase within the lesion shown in Fig. 5.5 as a function of therapy turning on/off. Each 'on' phase comprises 10 time points corresponding to 50 histotripsy pulses. As more histotripsy pulses are delivered to the tissue, the magnitude change becomes larger, corresponding to higher random motion. The phase change shows a linear phase component due to tissue heating up. As the therapy progresses, the phase change becomes smaller due to increased random motion and decreased bulk motion.

5.4.2 Monitoring Histotripsy using Non-Cartesian Acquisition

Histotripsy-induced real-time changes were also visible with the spiral acquisition in both the gel and *ex-vivo* brain tissues (Fig. 5.4). The relative signal change in magnitude and phase was similar to the Cartesian acquisition. Since the spiral acquisition temporal resolution is significantly higher than the spin-warp acquisition, we can track the histotripsy-induced changes to the tissue for every 5 histotripsy sonications.

Fig. 5.5 shows representative real-time spiral images in the brain tissue for different histotripsy dose levels during the course of the therapy. As the tissue gets ablated with more histotripsy pulses, we see an increase in the random motion within the lesion, as seen by the increased loss in the image magnitude difference. The signal from the treatment region is shown as a function of treatment on/off in Fig. 5.6. The tissue phase shows an increased displacement away from the array. The magnitude within the lesion gets darker with more histotripsy pulses, indicating increased signal loss due to larger incoherent motion with therapy progression. Once the cellular tissue matrix is completely broken down, additional pulses only mix the water molecules, and the magnitude does not decrease further.

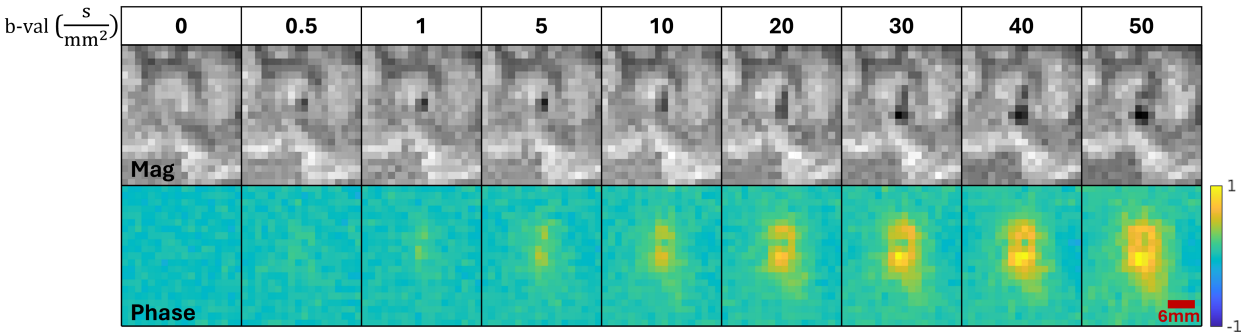

Figure 5.7: Effect of increasing gradient amplitude to histotripsy cavitation. Higher amplitude gradients (corresponding to larger k-space) are more sensitive to random and bulk motion inside the lesion.

5.4.3 Effect of Gradient Amplitude

The change in the image magnitude and phase to histotripsy with varying gradient amplitude but the same encoding time (T_{enc}) is shown in Fig. 5.7. As expected, the magnitude and phase contrast increase with a larger gradient amplitude since both the sensitivity to random and bulk motion are proportional to the gradient area. With a larger b-value (and cycles of phase), a larger cavitation region is visible in the magnitude image. This can be attributed to larger sensitivity to smaller random motion within the lesion. The phase image contrast was observed to scale linearly with the gradient amplitude since the phase is linearly proportional to spatial location and gradient area.

5.4.4 Effect of Encoding Time

The sensitivity of the pulse sequence to the location of the start of the second gradient (T_{enc}) is shown in Fig. 5.8. The b-value increases with a larger distance between the two gradients, but the k-space frequency across the lesion is the same for all figures. Similar to Section 5.4.3, the magnitude image shows a larger region containing the lesion with increasing b-value. The phase contrast decreases with increasing T_{enc} and b-value. Since the phase images encode the net displacement within the lesion, with larger T_{enc}, the spins within the lesion can relax back to the equilibrium position, leading to less phase accrued due to displacement.

5.4.5 Monitoring Transcranial Treatment

The real-time spiral pulse sequence could also visualize treatment through the human skull (Fig. 5.9). The change in magnitude and phase through the skull was smaller than in the free-field experiments due to lower peak-negative pressures achievable through the skull.

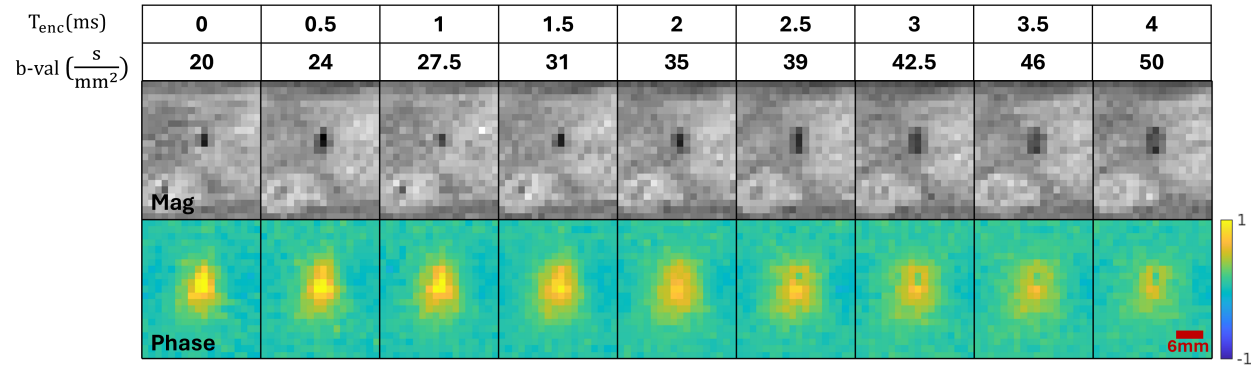

Figure 5.8: Effect of increasing gradient delay (T_{enc}) to the sensitivity to histotripsy cavitation events. With larger T_{enc}, the lesion appears larger due to a higher b-value. The phase contrast decreases with T_{enc}, suggesting that a large number of spins return to their equilibrium state 4 ms after the cavitation event.

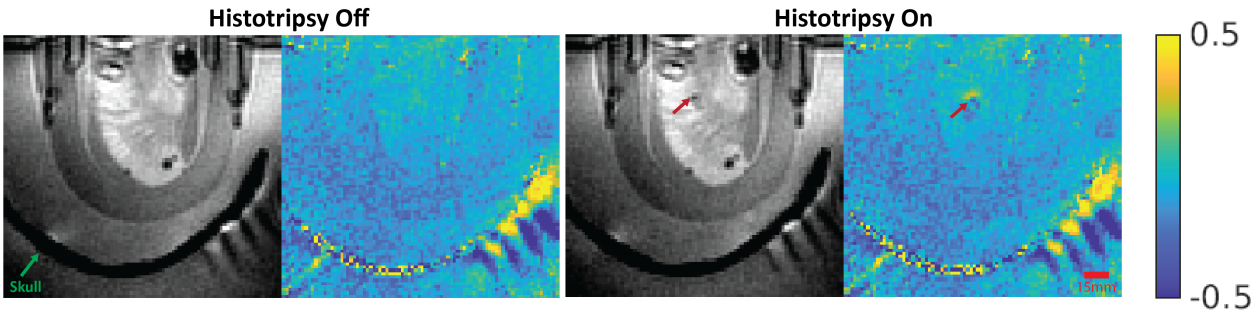

Figure 5.9: Magnitude and phase change due to histotripsy pulses in gel and *ex-vivo* brain tissue. The images show a similar trend in image contrast to the free-field histotripsy case. the signal change region is lower than the free field due to the reduced pressure through the skull.

The sensitivity to histotripsy through the skull can be increased by using larger encoding gradients.

5.4.6 Comparison with Actual Lesion

The location of the lesion from real-time histotripsy monitoring and post-histotripsy DWI is shown in Fig. 5.10. The magnitude of the real-time image corresponded well with the location of the lesion observed in the post-treatment b=1000 s/mm^2 DWI scan. This observation is unsurprising since histotripsy sonication creates high random motion within the acellular homogenate observed in the real-time images. The homogenate has a high diffusion coefficient and thus creates a hypointense region in the post-treatment DWI image. The phase change extends beyond the range of the actual histotripsy lesion. Although the phase image doesn't

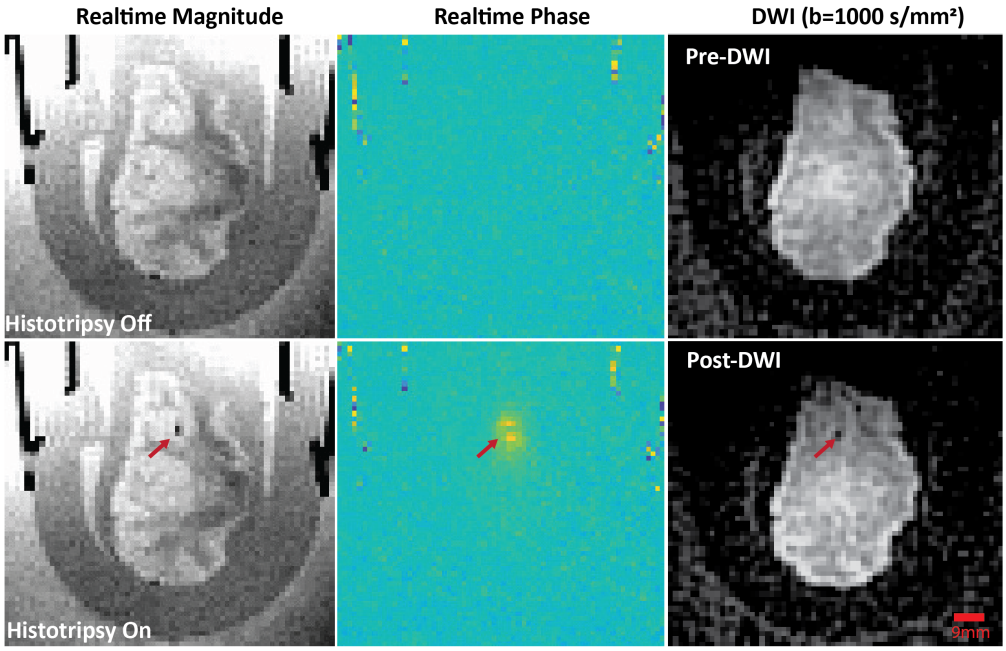

Figure 5.10: Comparing the location of signal change from real-time histotripsy with the actual post-treatment lesion location. The magnitude change corresponds well with the location of signal loss in post-treatment DWI. The phase change is activated at the periphery of the histotripsy lesion.

directly correlate with the location of the histotripsy lesion, it provides information about the possible extent of treatment effect caused by bulk motion effects. These effects might cause additional treatment effects such as blood-brain-barrier opening in *in-vivo* subjects.

5.5 Discussion

Transcranial histotripsy is a promising therapy for treating brain cancers. Prior *in-vivo* animal studies have demonstrated that histotripsy can treat various targets around the brain through an excised human skull without generating significant heating to the skull. In prior work [65], we have also demonstrated the feasibility of using tcMRgHt to perform brain histotripsy treatments in a human MRI scanner. MRI is already a crucial tool for visualizing brain diseases due to its superior soft-tissue contrast and sensitivity to various tissue properties. Previous work has also demonstrated that MRI can provide pre-treatment targeting and post-treatment dose analysis for histotripsy treatments [3, 1, 31]. Allen et al. [1] captured the changes in image contrast to histotripsy in water and *ex-vivo* liver on a 7 T animal scanner. It was demonstrated that b-values smaller than $1\,\mathrm{s/mm^2}$ is sufficient to visualize histotripsy sonications, although the relative timing of the sonication is important to

get high image contrast. In this work, we evaluate the feasibility of real-time MRI treatment monitoring of histotripsy treatment in a 3 T human MRI scanner.

This work focuses on the changes in MR-visible contrast due to histotripsy sonications in *ex-vivo* brain. The aim of this work was to observe changes in the histotripsy lesion with treatment progression and also validate treatment monitoring for transcranial histotripsy. Although the slice-selection gradient can be used to sensitize the images to histotripsy, we propose using a set of bipolar gradients to encode histotripsy-induced motions. Histotripsy pulses are µs-long, and the accompanying bubble cloud dynamics could last a few ms. Also, since histotripsy is a stochastic event, no two sonications can be expected to be the same. Due to the relatively longer time scales used in MRI, it is harder to resolve temporal changes caused by histotripsy. Nonetheless, MRI can be sensitized to the mm-order changes caused by histotripsy and is shown to capture 100 µm-order bulk motion effects post cavitation events. MR images were sensitized to histotripsy treatments by using bipolar gradients to encode motion.

The image magnitude and phase are sensitive to the histotripsy sonications and carry complementary information about the treatment. The rapid random motion within a lesion appears as a signal loss in the magnitude image. On the other hand, the bulk shift in the medium due to the tissue stretching from the bubble cloud and radiation force-induced bulk displacement after histotripsy treatments appears as a change in the phase image.

The phase changes appear more sensitive than the magnitude change and were observed in a region much larger than the estimated histotripsy lesion. We also observed that the relative timing of the histotripsy and the gradient pulses can lead to different phase contrasts. The large spatial extent of the phase images could be due to tissue stretching, ARF-induced bulk motion, and shear waves from the bubble cloud. An added benefit of phase images is the potential to be sensitive to histotripsy with short T2* species such as blood. Since the signal from magnitude images will appear hypointense, the phase changes might prove to be a more valuable measure of the histotripsy event.

Images acquired from *ex-vivo* brain using a non-Cartesian spiral acquisition demonstrated that real-time histotripsy monitoring is possible at a higher temporal resolution. The spiral acquisition had a temporal resolution of 0.5 s. The same pulse sequence can be used with several interleaved slices without a change in the temporal resolution. With the spiral acquisition, an image with 5 histotripsy sonications was generated, and a treatment dose-related change in the magnitude and phase was observed.

Future work will investigate quantifying the dynamic changes from the histotripsy event. This can be done by implementing a time-resolved MR-pulse sequence, where the motion-sensitizing gradients are timed at a much finer spacing after histotripsy, allowing time-

resolved measures of tissue displacement from the phase images. We can also investigate the potential shear wave component from the bubble cloud by using a pulse sequence similar to the MR-ARFI shear-wave elastography [43]. The real-time phase change image may contain information about the region where the histotripsy-induced blood-brain barrier opening occurs and must be investigated. A limitation of this study is the use of 1 imaging slice to perform real-time monitoring. This was done to ensure that all histotripsy sonications were captured in the same imaging slice. Future work will incorporate a multi-slice or 3D pulse sequence to measure the complete treatment volume. Since the real-time images have high temporal coherence, future work will investigate undersampled reconstruction, allowing a higher temporal resolution [59]. Nonetheless, the histotripsy pulse repetition frequency for *in-vivo* treatments might be much faster than the temporal resolution achievable by MRI scanners. In future work, it is likely that MR treatment monitoring would incorporate multiple treatment sonications per image.

5.6 Conclusion

This study is the first demonstration of real-time histotripsy monitoring in *ex-vivo* brain in a human MRI scanner. It was shown that the histotripsy cavitation events could be sensitized to both the magnitude and phase of the image by encoding the histotripsy motion using gradient pulses. A faster 2D acquisition method allows visualization of histotripsy treatments at a sub-second time scale without losing the treatment information.

5.7 Supplemental Data

5.7.1 Choosing Encoding Gradient Axis

The encoding gradients were played along the x, y, and z directions to observe the direction of motion due to histotripsy cavitation events. The change in the magnitude and phase for each gradient direction is shown in 5.11. The change in magnitude is not affected by the gradient direction, signifying that the random motion is isotropic in nature. The phase change is maximized when the gradient is played along the y-axis. Therefore, most of the bulk-motion effects due to cavitation occur along the direction of ultrasound propagation.

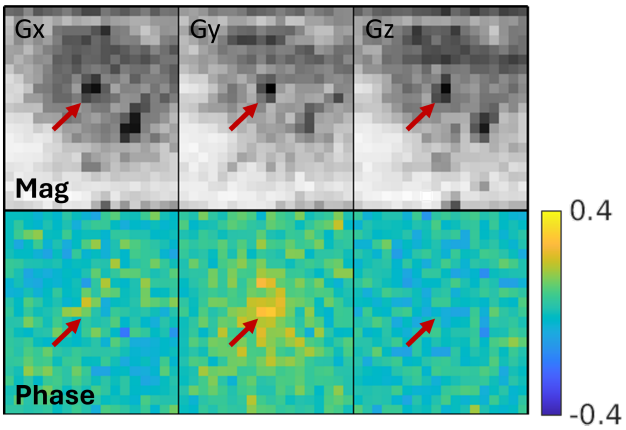

Figure 5.11: Visualizing histotripsy induced motion with different gradient direction. All three acquisitions were performed using a b-value of $10\,\mathrm{s/mm^2}$.

CHAPTER 6

Histotripsy Post-Treatment Evaluation

6.1 Introduction

About 700 000 Americans are currently diagnosed with cancers of the brain [5, 83, 55]. Treatment for brain diseases is typically performed by either surgical removal of the tumors or by radiation therapy. These methods are invasive and expose patients to harmful ionizing radiation [16, 41, 55, 30]. Many alternatives to these invasive methods are currently being investigated. Transcranial MR-guided high-intensity focused ultrasound (tcMRgHIFU) thermal treatment has been used to treat brain diseases noninvasively [17, 12, 63, 82] and is used clinically for the treatment of essential tremor, Parkinson's disease, osteoid osteoma, and uterine fibroids [92, 104, 22, 77, 21, 58]. tcMRgHIFU has seen limited clinical success in treating brain tumors due to a potentially small treatment region and overheating of the skull due to high duty-cycle sonication [15, 72]. Blood-brain-barrier (BBB) opening is another alternative method that uses FUS to temporarily open BBB to allow delivery of chemotherapeutic drugs to the tumors, which are otherwise restricted from entering the brain due to their large particle size [74]. So far, BBB opening studies have shown limited clinical success.

Histotripsy is a FUS-based treatment method that uses µs-long and high peak-negative pressure pulses to generate ultrasound cavitation and non-invasively tear down tissues with high precision [108, 85]. Transcranial histotripsy has been shown to treat a wide range of locations in the brain without significant temperature increase [28, 96, 94, 95]. Recently, we have demonstrated the feasibility of using transcranial MR-guided histotripsy (tcMRgHt) to treat various locations in *in-vivo* porcine brain. We have also used MR-thermometry and MR-ARFI for pre-treatment targeting of histotripsy treatments in the *ex-vivo* bovine brain [66, 65, 31].

Portions of this work have been presented at 32st Annual Meeting of ISMRM and 22nd Annual Meeting of ISTU [34, 35].

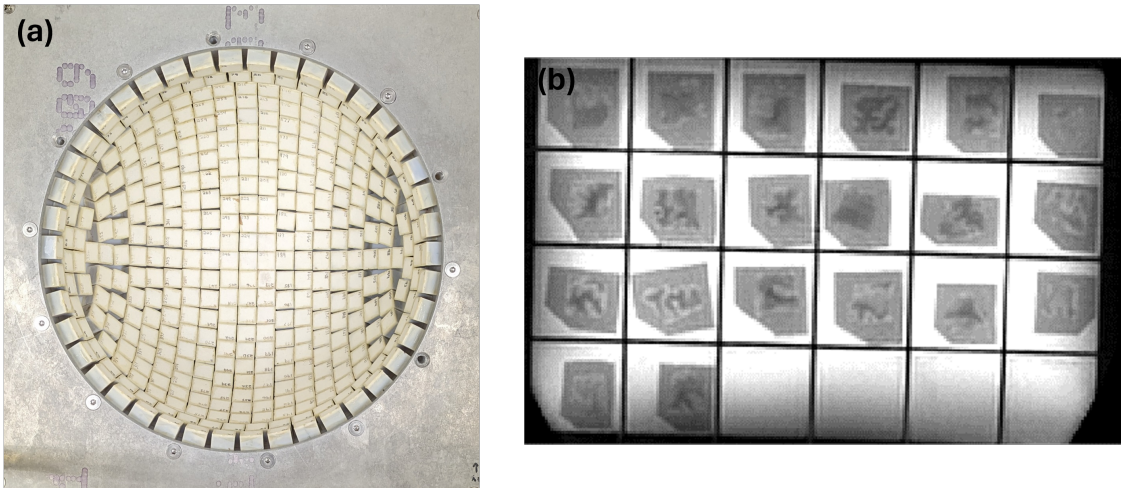

Figure 6.1: (a) 360 element histotripsy transducer used to perform histotripsy treatments in Section 6.2.1. (b) T2-weighted image of 20 tissues treated with the histotripsy array.

In order to deliver a sufficient dose for complete thermal necrosis, tcMRgHIFU therapies often use a thermal dose estimated from a time series of MR-thermometry images as a mechanism of estimating the stopping criteria for the treatment [89, 82]. Tissue necrosis due to temperature depends on the temperature and the length of time of exposure, as well as the physical properties of the tissue being treated. There is a tissue-specific temperature threshold ($\sim$43 °C for human tissues), beyond which the same damage could be achieved for multiple combinations of temperature and heating exposure time. Typically, a thermal isoeffective dose [91] is used to convert the delivered dose to an equivalent number of minutes of treatment at 43 °C using the following relation:

$$\text{CEM43 °C} = \text{tR}^{(43-\text{T})}, \tag{6.1}$$

where CEM43 °C is the cumulative number of equivalent minutes at 43 °C, R is a constant depending on tissue property (typically 0.17-0.25), t is the time of heating, and T is the average temperature at which heating was done. At 43 °C, it can take 25-240 minutes for complete necrosis [91]. This information can be used to deliver the required dose when the temperature is estimated by MR-thermometry.

Future tcMRgHt treatments will require quantified tissue damage to establish a stopping criterion and confirm that the intended dose was delivered to the brain without over-treatment. Using MR-thermometry to evaluate treatment dose does not apply to histotripsy since histotripsy treatments are non-thermal in nature and rely on mechanically breaking down the tissues. This limitation has led to the exploration of other metrics to estimate

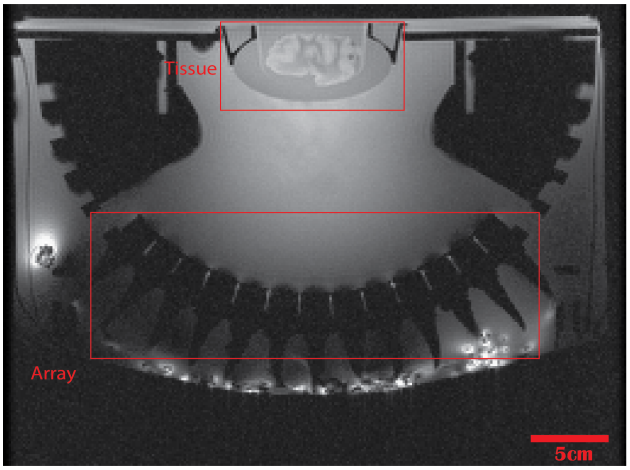

Figure 6.2: Experimental setup for treatment in Section 6.2.2. The parameter maps were acquired in a plane orthogonal to this image.

histotripsy dose, such as the cavitation emission signal from the expanding and collapsing histotripsy bubble clouds [39]. Allen et al.[3] studied the changes in T1, T2, and apparent diffusion coefficient (ADC) with histotripsy dose in various tissues on a 7T animal scanner. The aim of this study is to estimate histotripsy dose response in the brain on a 3T human scanner. The brain's heterogeneity and the significant differences in MR parameters from one region to another [8] make this a challenging area of study since the same ultrasound sonication could impart different treatment doses and show different MR responses. Many treatment parameters, such as the array's operating frequency and f-number, the peak-negative pressure, the number of pulse repetitions per location, the treatment's pulse repetition frequency, the treatment point spacing, and Young's modulus of the tissue, affect the histotripsy dose. Naturally, the treatment parameter space of delivering the same therapy dose is large. Still, our assumption is that for a given dose delivered to a tissue, the change in MR-visible tissue parameters would be the same regardless of what combination of treatment parameters was used to deliver that dose. Based on the result of the previous study on the 7 T scanner, this work evaluates the changes in T1, T2, and ADC to varying histotripsy doses in the brain, using *ex-vivo* bovine brains for dose estimation and comparing the damage to histology.

6.2 Methods

To evaluate the changes in MR-visible contrast to histotripsy treatments, *ex-vivo* bovine brains were treated with histotripsy and subsequently imaged using MRI. The bovine brains were collected from a nearby slaughterhouse up to 24 hours before performing histotripsy treatments and were stored in degassed saline until the start of the experiments. The brains

were set in 1.5 % agarose gel using 3D-printed molds to rigidly hold them during the course of the experiments. MR imaging was performed on a 3 T GE UHP human MRI scanner (GE HealthCare, Chicago, IL), and 21-channel GE AIR coil was used for acquiring MR data.

6.2.1 Evaluating Change in MRI Parameters to Dose

In the first experiment, twenty tissue samples were treated with varying levels of histotripsy dose to evaluate the MR parameters sensitive to histotripsy dose. The experiments were conducted with a 700 kHz, 360-element transmit-receive hemispherical histotripsy array with 15 cm focal distance. The top view of the histotripsy transducer is shown in Fig. 6.1. To align the tissue with the focus of the array, histotripsy was first generated at the focus in free-field, while two lasers were aligned such that they intersected at the histotripsy bubble cloud. Then, with the array turned off, the center of the tissue was steered to the aligned lasers using a motor system. All the tissues were imaged together in the MRI scanner after the treatments were concluded. The treatment parameters and MR imaging parameters are described in the subsequent sections.

6.2.1.1 Histotripsy Treatment Parameters

A 8 mm cubic lesion was made using a hexagonal packing grid with 0.5 mm spacing for a total of 6463 treatment locations with 500 Hz pulse repetition frequency. The histotripsy pulses were 1.5-cycle long with a peak-negative pressure of 40 MPa. Based on a separate small sample study, the histotripsy dose corresponding to complete tissue liquefication was estimated using histology and found to be 15 to 20 pulses per location. The dose was varied by treating 3, 5, 10, 20 and 30 pulses per location. Each of these five doses was repeated four times for twenty treatments. Once all the tissues were treated, they were placed in a box to acquire MR images.

6.2.1.2 MRI Acquisition

T1, T2, and ADC changes were evaluated as a function of histotripsy dose. T1 mapping was performed using variable flip-angle spoiled gradient recalled echo (VFA-SPGR) method [10] using the following scan parameters: TE/TR: 3ms/8ms, FA: 2°, 3°, 5°, 10° and 15°, FOV: 22 cm × 22 cm, matrix size: 256 × 256, slice-thickness: 2 mm. T2 mapping was performed using a vendor-provided T2-mapping sequence with a fast spin echo (FSE) acquisition. The following scan parameters were used: TR: 800 ms, TE: 5.7 ms to 45.7 ms with 5.7 ms increments, 22 cm × 22 cm, matrix size: 256 × 256, slice: 2 mm. A mono-exponential decay curve was fit to the acquired data to estimate the T2 of the tissues. ADC was estimated using a

vendor-provided DWI PROPELLER [25] scan with parameters: TE/TR: 48/4000ms, b: 0 and 500 s/mm^2 diffusion direction: A/P, FOV: 38 cm × 38 cm, matrix size: 256 × 256, slice: 3 mm. T1 and T2 maps were registered to the ADC maps using MATLAB's `imregister` function with a mutual information cost function. The lesions were labeled on the MR parameter map image for each histotripsy dose, and analysis was performed on all voxel intensities within the labelled region.

To identify the statistical significance of the three MR parameters in estimating the histotripsy dose, a linear regression model was fit to compare the change in the mean of the T1,T2 and ADC within the lesion with the applied histotripsy dose. The mean was chosen as a surrogate for the histotripsy dose throughout the lesion. A parameter map was deemed statistically significant for p-value $< \alpha = 0.05$. The linear fit was performed using MATLAB's `fitlm` function. The accuracy of the fit was also estimated by determining R^2 of the fit.

6.2.1.3 Histological Analysis

Following the MRI scans, each tissue sample was fixed in 10 % formalin for 48 hours, then removed and stored in 70 % ethanol. To prepare for hematoxylin and eosin (H&E) staining, each tissue block was cut in half so the slice was through the middle of the ablation region. A portion of tissue was cut from the block and positioned in the histology cassette such that the face of the ablation zone would be faced for slicing and staining. One slide was stained for each treatment sample for H&E staining.

6.2.2 Evaluating change in ADC with Dose

Since brain tissue is heterogeneous, the change in MR parameters to histotripsy dose might differ for different treatment regions. Therefore, to remove intra-tissue variability, the same tissue was treated with varying levels of histotripsy dose. For this experiment, brain tissues were placed in the MR scanner and treated with an MR-compatible histotripsy array (Fig. 6.2) [66]. MR parameter maps were acquired after each histotripsy dose was delivered to the tissue until the tissue was completely ablated. Further details about the experimental setup and treatment methods can be found in the subsequent sections.

6.2.2.1 Histotripsy Treatment Parameters

The array used in this experiment is similar to the array described in the Section 6.2.1 but populated with 128 out of the 360 elements [66]. A customized gel holder was made to align the center of the tissue with the histotripsy focus to ensure that the treatment was done in

the tissue. 8 mm square lesions were created using a linear raster scan with 1458 treatment points with 100 Hz pulse repetition frequency. The histotripsy pulses were 1.5-cycle long with a peak-negative pressure of 75 MPa. The dose was varied by treating 1, 5, 10, 20, 30, 40 and 50 pulses per location. MR acquisitions were taken after each dose was delivered to the brain tissue. This experiment was repeated for 3 tissues.

6.2.2.2 MRI Acquisition

Based on the results of the Section 6.2.1, only changes in ADC were measured for these tissues. Diffusion imaging was performed using the vendor's DWI SMS-EPI scan with a Hyperband factor of 2 slices. The scan parameters were: b-value: 0, 500, 1000 and 2000 s/mm^2, 3-directions, TE/TR: 71.5ms/2000ms. The acquisition used 0.5 times the object FOV, but no image wrap-around was observed over the tissue region. FSL's `dtifit` function was used to estimate the ADC in the tissue.

Similar to the analysis performed in Section 6.2.1, the mean change in the ADC and ΔADC maps within the lesion were fit with respect to the histotripsy treatment dose delivered to the tissues. The regression analysis was done for 24 data points (3 tissues $\times$ 8 dose levels). The α value of 0.05 was chosen to determine the statistical significance.

6.3 Results

6.3.1 Change in MR parameters to Dose

Histotripsy lesions were visible in all the tissues for all the levels of delivered histotripsy dose. A representative slice containing the histotripsy lesion was selected for each tissue. Then, an ROI containing the tissue was cropped for further analysis (Fig. 6.1). Fig. 6.3 shows a representative tissue for each dose level and its corresponding b=500 s/mm^2, T1, T2, and ADC maps. Only the T2 and the ADC maps showed a contrast to the histotripsy treatment. The mean T2 values decreased, and the mean ADC value increased within the histotripsy lesion compared to the untreated regions. Since a diffusion-weighted image's signal decreases with increasing ADC and a decrease in T2, the b=500 s/mm^2 images had the highest lesion contrast.

The range of T1, T2, and ADC values across each dose is shown in Fig. 6.4. The T2 values were lower within the lesions but did not exhibit a dose-related linear trend ($R^2 = 0.004$, $p > 0.05$). Similar to the T2 values, the T1 values did not correlate with the dose for all the treated tissues ($R^2 = 0.01$, $p > 0.05$). Using a two-sample t-test, the ADC between the treatment region was significantly increased compared to the untreated region ($p < 0.005$).

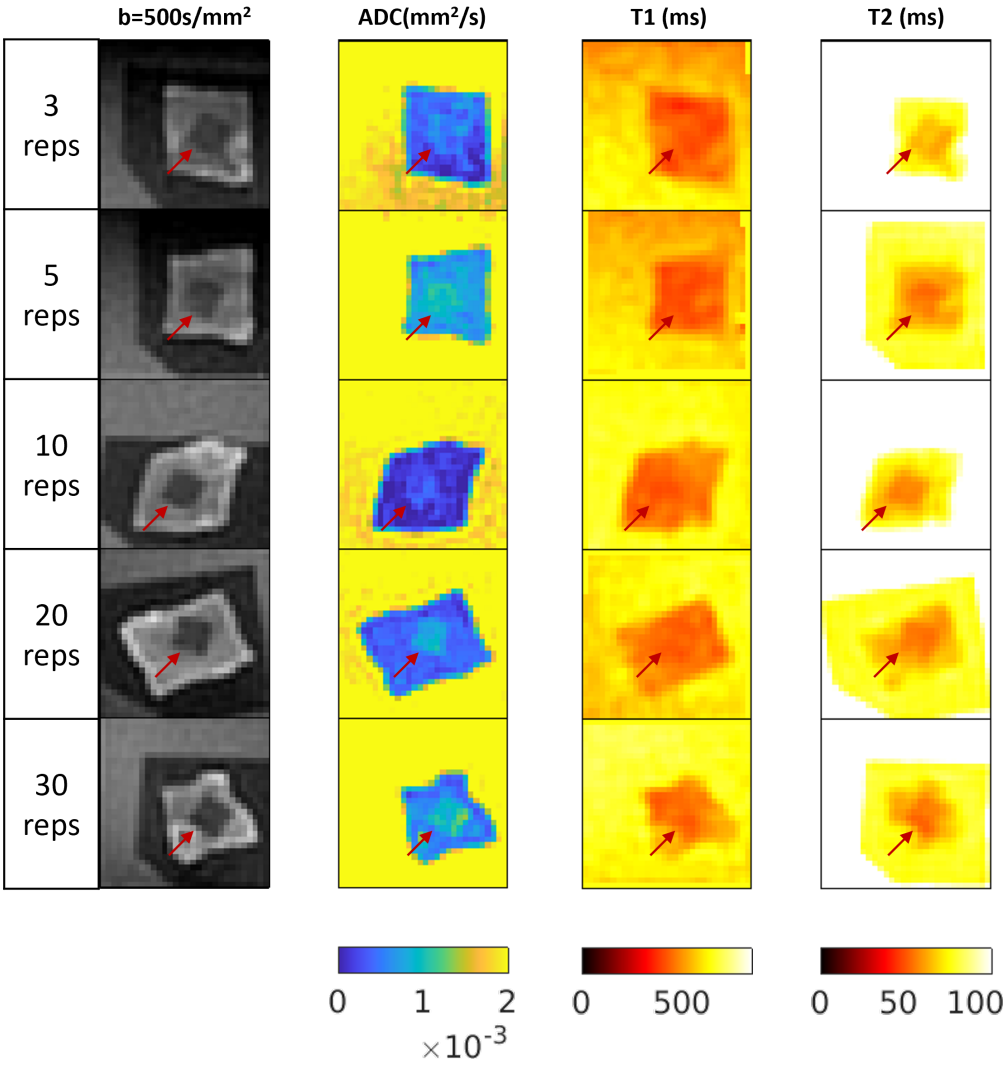

Figure 6.3: Representative b=500 s/mm^2, ADC, T1 and T2 images for each dose level. The dose (repetitions/location) is labeled on the top left of each row. Diffusion-weighted image visualizes the lesion well with sharp boundaries between treated and untreated regions.

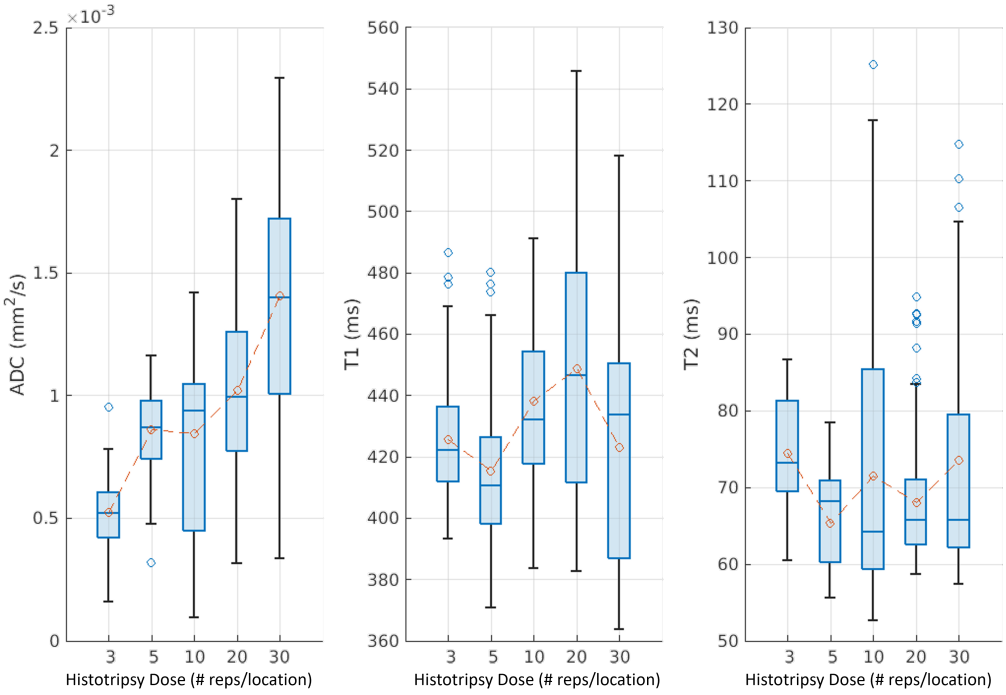

Figure 6.4: Box plot of change in ADC, T1 and T2 with histotripsy dose. Each bar plot represents values from 4 tissues treated with the same dose. The dotted red line represents the mean at each dose level. Only ADC shows a significant ($p < 0.001$) dose-related increase in parameter values.

For most tissues, mean ADC values increased with a higher histotripsy dose. The linear fit to the mean ADC showed a correlation ($R^2 = 0.45$, $p < 0.001$). The modest R^2 value can be explained by the intra-tissue heterogeneity, which could result in different mean ADC values at the same dose levels. The mean change in ADC between tissue treated with the lowest and highest histotripsy dose was $\sim 0.9 \times 10^{-3}\,\mathrm{mm^2/s}$. Since the brain tissue is heterogeneous in nature with a range of ADC, T1, and T2 values, it is possible that different regions of the brain would require different levels of histotripsy dose to get the same level of damage.

Histology of the tissues shown in Fig. 6.3 is shown in Fig. 6.5. The histology slides show that histotripsy treatments were delivered to varying tissue types within the brain. Histotripsy treatments rupture the tissue's cellular structure, but the precise treatment boundaries were evident for all tissues. The number of visible nuclei (black dots) in histology is reduced as the histotripsy dose increases. As more treatment is done, the cavitation events destroy the cell nuclei into smaller segments until the nuclei are completely diffused throughout the treatment region. The destruction of cell nuclei could lead to an increased diffusion of water molecules due to reduced restriction of motion. Also, once a histotripsy lesion is created, it not only breaks the cells but also mixes the cellular material from different parts of the lesion volume. Therefore, it is unlikely that a uniform measure of T1, T2, and ADC would be visible throughout the lesion volume.

6.3.2 Evaluating change in ADC with Dose

For the histotripsy treatments performed in the MRI scanner, the lesion was identified from the b=1000 s/mm^2 image with the largest delivered dose. Fig. 6.6 shows the raw b=1000 s/mm^2 image for all 3 tissues. As the tissues get treated with more histotripsy dose, the lesion appears darker due to increased diffusion and/or reduced T2 effects. An ROI was selected on the image with the largest histotripsy dose, and the changes in ADC were tracked for each voxel within the lesion. Fig. 6.7 shows the ADC maps within the lesion at all dose levels. The ADC maps showed an increased diffusion coefficient with increasing treatment dose for all tissues. Since the same tissue is treated with varying levels of histotripsy dose, a change in the ADC parameter (ΔADC) map was also estimated (Fig. 6.8). The ΔADC map visualized the lesion with higher contrast and showed the precise boundaries of the treatment region.

The mean ADC within the lesion increases with the delivered histotripsy dose (Fig. 6.9). The regression analysis of the mean ADC against histotripsy dose shows a strong linear relation ($R^2 = 0.903$, $p < 0.001$) of ADC to predict histotripsy dose. Similarly the ΔADC analysis shows high correlation with histotripsy delivered dose ($R^2 = 0.914$, $p < 0.001$). As

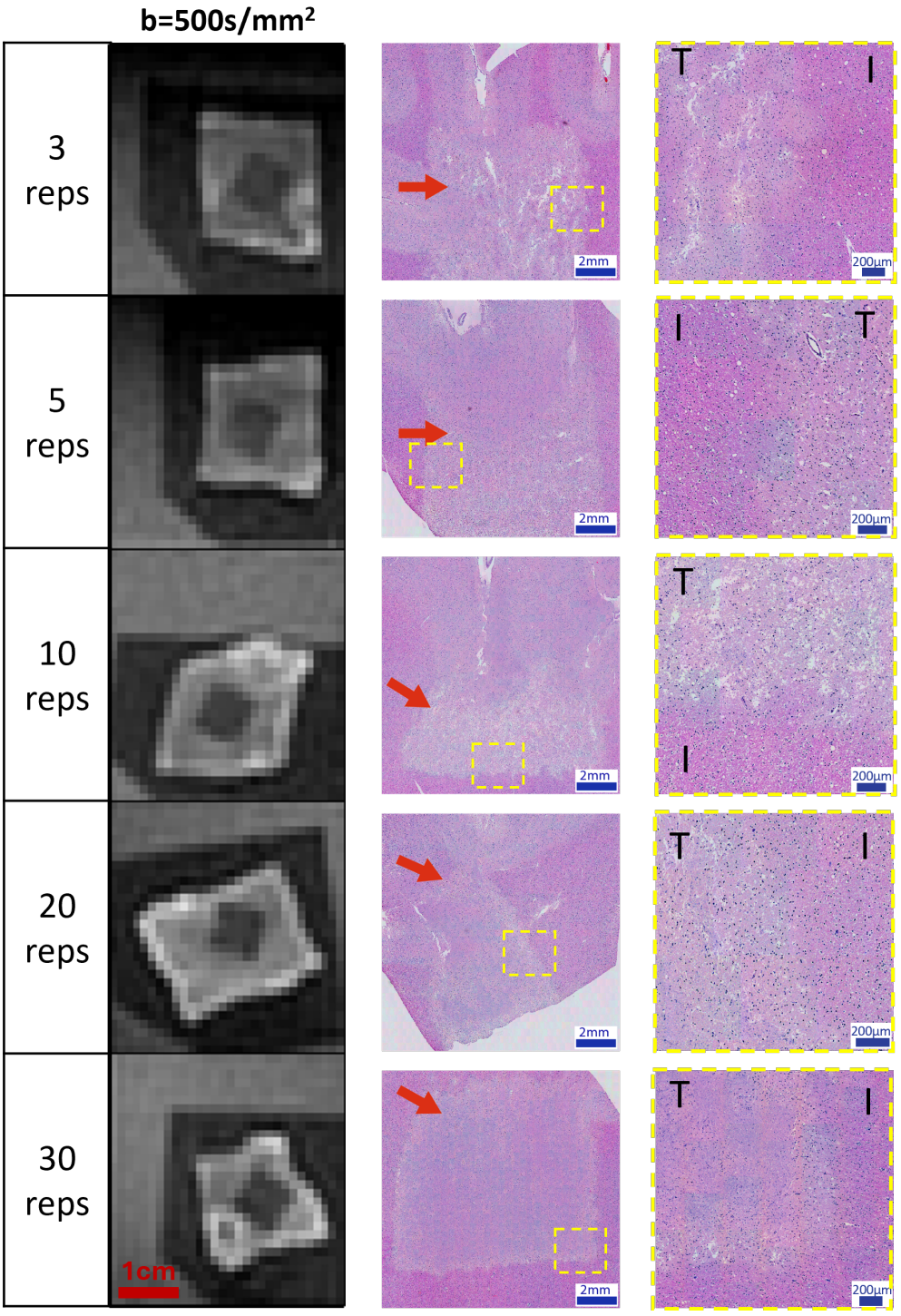

Figure 6.5: Histology from the tissues shown in Fig. 6.3. The red arrow in the center plot marks the histotripsy region. In the zoomed histology images on the right, the boundary of treated (T) and intact (I) tissues can be observed.

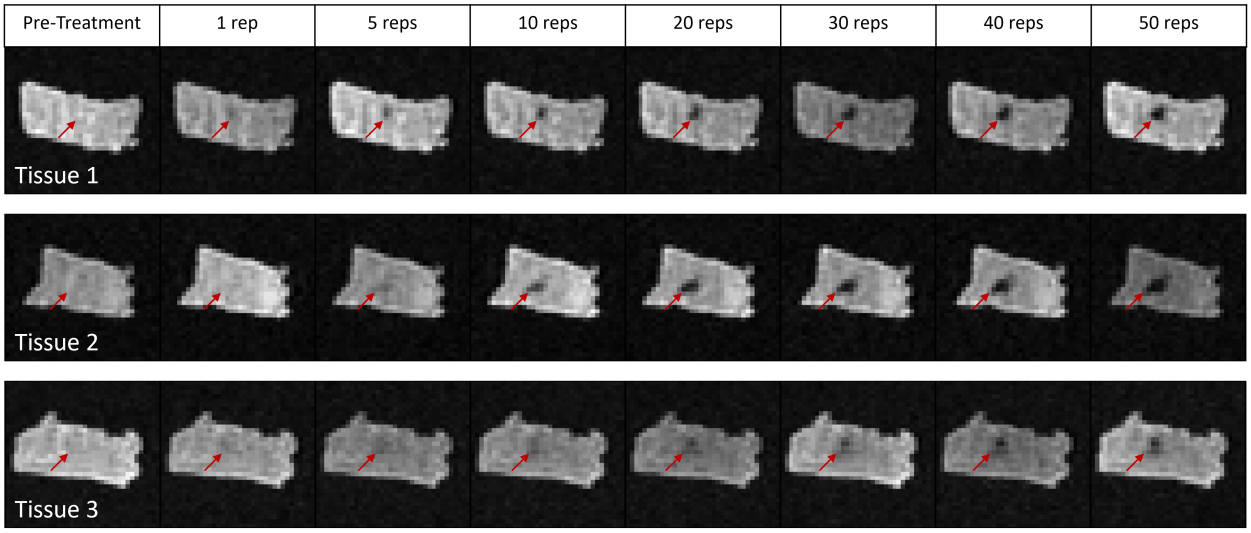

Figure 6.6: b=1000 s/mm^2 images for 3 tissues treated with increasing dose of histotripsy. The lesion grows and appears darker as the tissue gets treated with a higher dose.

the tissue gets treated with more histotripsy dose, the range of ADC values also displays higher variations. This deviation in the ADC could be due to variations in brain tissue's material properties that might require different levels of histotripsy dose for an equivalent treatment outcome. In addition to the brain tissue's heterogeneous elastic properties, the variation could also be due to the spatially varying pressure profile from the histotripsy transducer, which causes variation in the level of damage within the lesion. The mean change in ADC was observed to be 6.5×10^{-4} mm^2/s with 50 reps of histotripsy dose.

The ADC within the lesion was also observed to plateau at 40 reps. Once the histotripsy treatments completely homogenize the treatment region, extra treatment pulses should impart negligible effect on the diffusion of water molecules inside the lesion. This would lead to a minor change in the ADC even when more histotripsy pulses are delivered to the tissues. Although the ADC appeared to have plateaued for the tissues treated in this study, further tissue samples and a higher delivered dose are essential to ensure the change in ADC plateaus after a certain histotripsy dose. This analysis also suggests that a higher-order or a non-linear fit might be more suitable for the association between ADC and histotripsy dose.

6.4 Discussion

tcMRgHt is a promising therapy that has demonstrated the ability to target various locations in the brain without generating significant heating of the skull. A quantifiable histotripsy

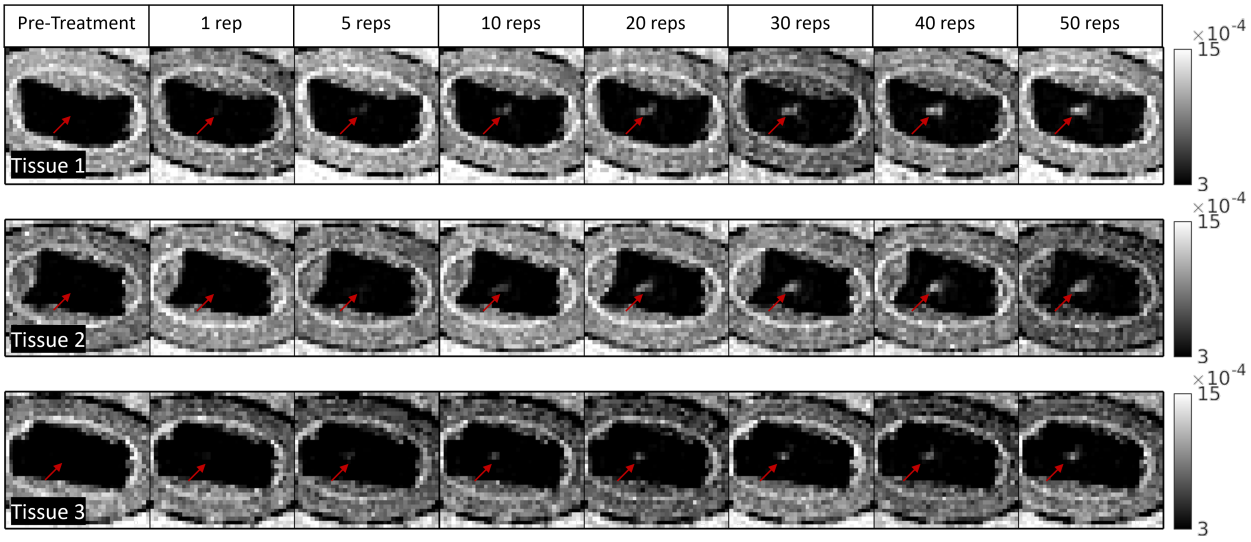

Figure 6.7: ADC map of 3 tissues treated with increasing dose of histotripsy. The ADC within the lesion gets larger as more histotripsy pulses are delivered to the tissue.

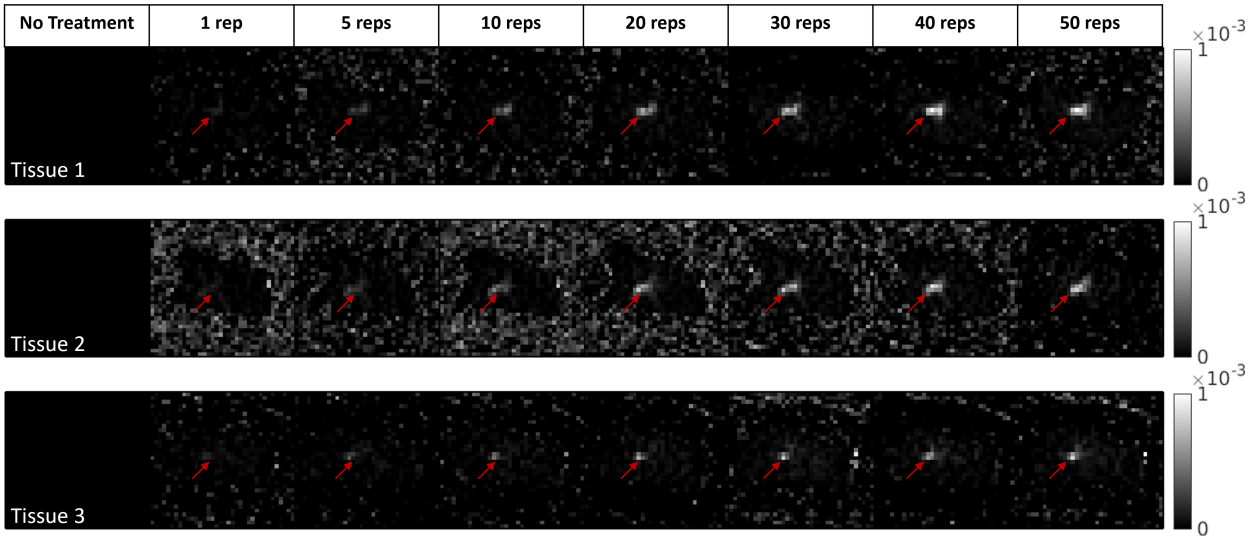

Figure 6.8: Change in ADC of 3 tissues treated with increasing dose of histotripsy. Only the lesion in the tissue shows an increase in ADC values.

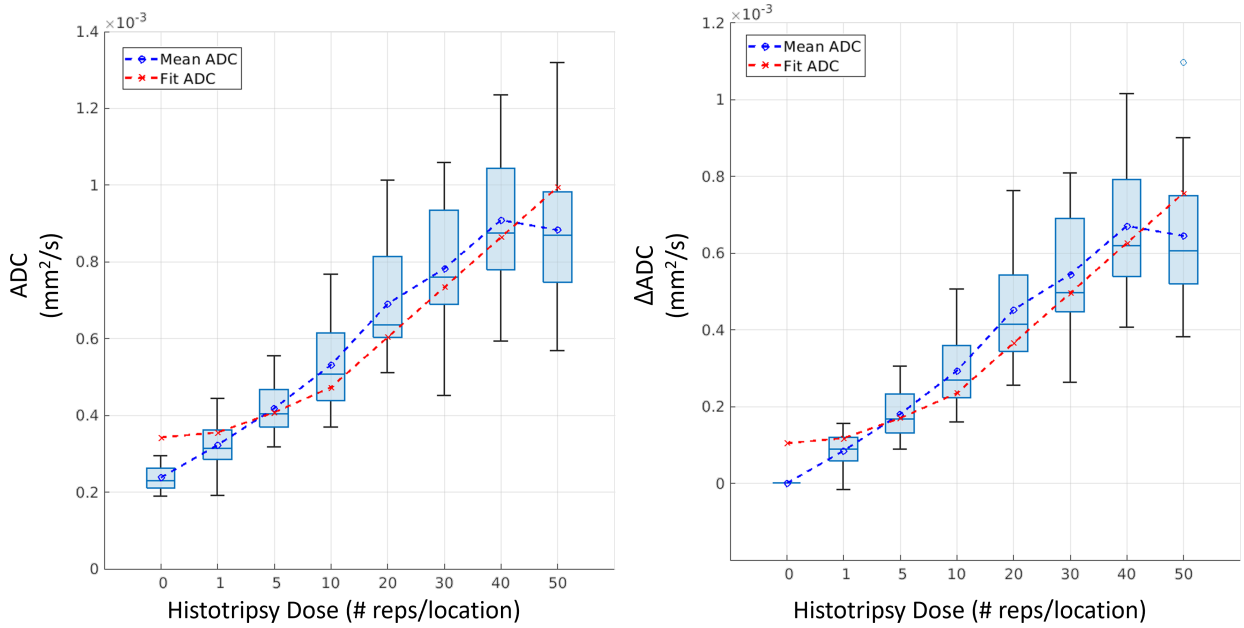

Figure 6.9: Box plots of ADC and change in ADC with histotripsy dose across 3 tissues. The blue line represents the mean ADC within a given histotripsy dose. The red line is the linear fit performed on the mean dose. Both ADC and ΔADC fit the mean accurately ($R^2 > 0.90$, $p < 0.001$).

'dose' measure is needed to ensure sufficient therapy is delivered to the target location. Similar tissue ablation from histotripsy can be achieved by varying ultrasound treatment parameters. Therefore, a metric of histotripsy dose that is agnostic to the treatment parameters but reflects the change in the tissue property is needed. In this work, we investigated the change in the ADC, T1, and T2 values in *ex-vivo* bovine brains as a function of histotripsy dose.

Two histotripsy transducers with different treatment parameters were used to treat multiple *ex-vivo* bovine brains. In the first set of experiments, the tissue parameters sensitive to histotripsy dose were studied. Multiple tissues were treated with different histotripsy doses and then subsequently imaged in the MRI scanner. Although a change in the tissue's T2 and ADC was observed, a dose-related change was only observed in the ADC maps. The mean ADC increased from $\sim 0.5 \times 10^{-3}\,\mathrm{mm^2/s}$ to $\sim 1.4 \times 10^{-3}\,\mathrm{mm^2/s}$ with increasing histotripsy dose from 3 reps to 30 reps ($p < 0.01$). Although this experiment provided valuable information about the changes in MR parameters to histotripsy, heterogeneity in the brain's elastic parameters made it difficult to understand dose variability within the same tissue.

In the second set of experiments, the change in tissue ADC with histotripsy dose was studied for the same tissue. Three tissues were treated with a 128-element histotripsy array

with increasing histotripsy dose. ADC maps were made after each dose of histotripsy to remove inter-tissue variability. The mean ADC increased from $\sim 0.25 \times 10^{-3}\,\mathrm{mm^2/s}$ to $\sim 0.9 \times 10^{-3}\,\mathrm{mm^2/s}$ ($p < 0.01$). The ΔADC values correlated well with histotripsy dose for all three tissues, further supporting ADC as a viable metric for estimating histotripsy dose in the brain.

The ADC of tissue depends not only on the tissue's cellular properties but also on the age and temperature of the tissue and the experimental conditions. This could explain the variability of the ADC between the two experiments. Out of the three parameter maps tested in this study, only a dose-dependent increase in the lesion's ADC was observed for both the histotripsy treatment methods. It is hypothesized that as the lesion becomes increasingly homogenized with more histotripsy pulses, the homogenate can diffuse more freely within the treatment zone, increasing the net ADC. Although variations in the ADC within the lesion were observed, the median and mean ADC across all tissues increased with higher histotripsy dose.

6.5 Conclusion

In this work, we demonstrated that histotripsy treatments in the brain can cause a change in the tissue ADC. It was observed that the ADC within the lesion increased linearly with increasing histotripsy dose. In future work, the net change in ADC could be used as a metric to inform treatment-stopping criteria. Future work will also correlate the histotripsy damage from histology to ADC to evaluate treatment dose.

CHAPTER 7

Conclusions and Future Work

This dissertation aimed to develop MRI methods to perform transcranial histotripsy treatments. To this end, we developed methods to perform pre-treatment targeting, real-time treatment monitoring, and post-treatment evaluation.

In Chapter 3, a method to perform pre-treatment targeting of histotripsy treatments using low-temperature heating generated by the histotripsy transducer was introduced. This method uses MR-thermometry and low-temperature heating to guide histotripsy therapy without causing irreversible tissue damage. FUS heating was achieved by playing short 1.5-cycle pulses at low pressure, but 50% duty cycle to heat the tissue to about 1.5 °C. The absolute mean/standard-deviation difference of the estimated lesion location using MR-thermometry was 0.59 mm/0.31 mm in the transverse and 1.31 mm/0.93 mm in the longitudinal planes, respectively.

In Chapter 4, the pre-treatment targeting method from Chapter 3 was extended to perform pre-treatment targeting of histotripsy treatments using two CW-based approaches. To achieve 'tone-burst' sonications for MR-thermometry and MR-ARFI, the electronic drivers used to perform histotripsy treatments were modified to allow high-duty-cycle but low-pressure sonications. The mean estimated error across all cases in the transverse/longitudinal axis was 2.06 mm/2.95 mm and 2.13 mm/2.51 mm for MR-ARFI and MR-thermometry, respectively. Future studies could employ either of these techniques to perform pre-treatment targeting, but MR-ARFI is potentially better due to its ability to map the ultrasound field and also the low risk of overheating the skull due to lower duty-cycle sonication.

In Chapter 5, a method to perform real-time monitoring of histotripsy lesions in the brain was discussed. Once the target has been localized and histotripsy treatment is ready to commence, real-time treatment monitoring would be needed to ensure the therapy is delivered at the intended spot without damaging any off-target locations. Real-time monitoring of histotripsy was done by modifying a GRE scan to encode the motion from the histotripsy cavitation events using bipolar gradients. It was shown that both the image magnitude and

the phase provide complementary information about the histotripsy sonications. The cavitation events cause a rapid increase in the local motion of the acellular matrix, which can be described as a combination of random and bulk motion. The random motion is encoded by a decrease in the image magnitude, and the bulk motion is encoded by the image phase. Realtime treatment monitoring was performed at a temporal resolution of 0.5 s using a spiral acquisition.

In Chapter 6, the changes in MR-visible parameters due to histotripsy treatments in the brain are described. After the histotripsy treatments are done, the damage caused by the therapy needs to be quantified to estimate the therapy dose. T2 and ADC of the tissue are affected by histotripsy treatments in the brain. It was shown that although both T2 and ADC values change with histotripsy treatment, only the ADC exhibits a dose-related increase. As the lesion becomes more liquified with increasing histotripsy dose, the ADC within the lesion increases as the water molecules can freely move in the homogenate. For the *ex-vivo* brains treated in the MR-scanner, the mean ADC was observed to increase by $6.5 \times 10^{-4}\,\mathrm{mm^2/s}$ with 50 reps of histotripsy dose compared to untreated tissue. The change in ADC was shown to be lineraly increasing from 1 to 40 reps and appears to plateau by 50 reps of histotripsy. Therefore, the ADC within a lesion might provide a surrogate for tissue damage due to histotripsy.

In conclusion, this body of work developed several MR methods that could be utilized to perform tcMRgHt therapies in the future. MR-ARFI and MR-thermometry could be used to localize the treatment region, and pre-treatment DWI scans can provide a baseline ADC value for the treatment region. Then, the histotripsy treatment would be performed while receiving feedback from the real-time treatment monitoring scan. The real-time dynamic changes in the magnitude and phase would also provide a possible treatment-stopping criterion. Finally, a post-treatment DWI scan would provide quantifiable dose information. Nonetheless, immense possible innovations can further enhance future tcMRgHt treatments. I briefly mention some potential future work in Section 7.1. Most of the pulse sequences that were used in this work can be found at `https://github.com/dinankg`.

7.1 Future Work

7.1.1 Pre-treatment MR-ARFI for Aberration Correction

Since histotripsy causes permanent damage to the tissue, aberration correction is important to ensure that the treatment is performed at the correct location and that enough power is available for focal steering.Transcranial ultrasound propagation undergoes severe aberration

due to the presence of the skull. Typical transcranial HIFU treatments use CT-based aberration correction that estimates the propagation phase delays for each element in the therapy transducer by using the Hounsfield units to estimate the relative sound speed through the skull. This process involved co-registering the therapy transducer to the pre-treatment CT, and MR-thermometry scans [90].

Although the methods in Chapters 3 and 4 can provide information about the location of the histotripsy focus, they cannot be used to provide aberration correction for the transducer. An alternative method is using the same HIFU device to perform aberration correction before treatment. MR-ARFI has been used to perform aberration correction for tcMRgHIFU therapies [40, 54, 50]. The method involves sonicating the target location with varying phase delays applied to each transducer element and measuring the displacement maps using ARFI. By performing multiple phase-delay sonications and having the knowledge of the position of each transducer element, a reliable aberration correction measurement has been made for FUS thermal and BBB therapies.

MR-ARFI based aberration correction could be used to facilitate histotripsy treatments. One can potentially use high-pressure but sub-threshold MR-ARFI sonications to perform aberration correction for histotripsy treatments. To save scan time, the array elements can be grouped to form smaller number of 'virtual transducers' [54] to estimate a set of initial delays. The delays can be used to deliver some histotripsy sonications at the target region. Once a few histotripsy pulses are delivered to the brain, acoustic cavitation emission signal-based aberration correction can further improve the element delays [39, 67]. This method would circumvent the need for a CT scan and avoid image registration-based errors in the aberration correction process.

7.1.2 Practical Real-Time Monitoring Pulse Sequences

The pulse sequences described in Section 5 are GRE based and image 1 slice to get a high temporal resolution. A GRE scan is sensitive to T2* effects and could make it difficult to observe a signal from *in-vivo* histotripsy lesions due to bleeding in the treatment region, which causes a signal loss due to hemoglobin in the blood. The change in the image phase could possibly provide enough contrast even when there is bleeding. There are many alternatives to the GRE based method that would be robust to loss of signal to tissue bleeding. Either a short-TE or a spin-echo-based method would be ideal to either image short T2* isochromats or rephase their signal [37, 64].

A spin-echo based might be readily available for most clinical scanners. To that end, there are two spin-echo based approaches that can be considered. First, a 2D spin-echo scan

with interleaved slice ordering would allow faster acquisition times for volume but slower temporal resolution for a given slice. Also, to sensitize the image to the motion/flow of histotripsy, the histotripsy steering might have to be linked to the location where the slice is being acquired. Second, a 3D fast-spin-echo (FSE) is another alternative spin-echo pulse sequence that provides some robustness against signal loss from bleeding. FSE can be either diffusion prepared [4], or histotripsy pulses could be played along with the crushers around the rephasing pulses. However, it should be noted that for *in-vivo* experiments performed on a 7T animal scanner, T2-weighted FSE scans were sensitive to bleeding [20]. Thus, a lower TE is still preferable for FSE scans, especially at higher field strengths.

7.1.3 Reduced FOV Pulse Sequences and Reconstruction

The imaging FOV for experiments involving the histotripsy array was restricted to be at least $40\,\text{cm} \times 40\,\text{cm}$ to avoid aliasing artifacts in the reconstructed image. Another issue with the large FOV is the time spent acquiring data with no valuable information about the treatment since it mostly contains water. Therefore, reducing the FOV of the images will be valuable in reducing scan times and/or providing higher-resolution images. The FOV can be reduced by modifying both the acquisition and reconstruction methods as described below.

7.1.3.1 Acquiring a Reduced FOV

The RF excitation pulse can be modified to either excite only an ROI of interest or saturate the region outside the ROI of interest. A few of the earliest methods to excite an inner volume are STEAM/PRESS ([36, 26]). The methods use a train of orthogonal slab excitation/refocusing RF pulses that only excite the intersection of all the pulses. Although this RF excitation method can be robust to field inhomogeneities, it is not ideal for dynamic scans used for tcMRgHt studies due to potentially depositing a lot of energy.

Another alternative is learning an optimized trajectory that can excite an inner volume or saturate an outer volume. [68]. The tailored RF pulses can be custom-designed and incorporate the $\vec{B}_0$ and $\vec{B}_1$ in the optimization cost function. The tailored RF pulse can be designed to have low specific absorption rate (SAR), thus making it more feasible for dynamic imaging.

7.1.3.2 Reconstructing a Reduced FOV

Most clinical MR imaging is done by using an array of receiver coils. For most of the work presented in this thesis, a 21-channel receive coil was used to acquire data. The receive coils typically comprise single-loop elements and associated electronics for tuning

and matching. The region of high signal sensitivity is usually about the diameter of the receive coil. Therefore, one can design RF coils with a diameter comparable to the depth of the planned histotripsy treatment. This would ensure minimal signal is acquired from the water bath; thus, the FOV for image acquisition could be reduced. Another alternative to reduce the FOV is using a sensor-domain beamforming approach called ROVir to reduce the already acquired data into a smaller number of sensitive coils in the ROI [52]. This approach can simultaneously reduce the acquired data's size while reconstructing the image only in the inner volume. It is possible that the data acquisition can be reduced to accompany the new FOV and resolution requirements based on the ROVir approach, thus reducing the scan times.

7.1.4 Temporal Reconstruction of Real-time Monitoring Data

The real-time treatment monitoring data will comprise of a time series of 2D/3D images. The dynamic images are mostly similar across time points, with localized changes only around the region where histotripsy treatments occur. Naturally, these images could be reconstructed by sharing information in images across time frames. Many spatiotemporal reconstruction methods for MR imaging can be used to monitor histotripsy treatments. Low-rank and compressed-sensing-based reconstruction approaches are the most commonly used methods that can be used for reconstructing dynamic histotripsy treatments [69, 60].

7.1.5 Change in MR-ARFI due to Histotripsy Treatments

It is known that the histotripsy lesions have a decreased elastic modulus compared to untreated regions [105]. Therefore, a measure of change in elasticity can be used as a potential metric for evaluating therapy dose. MR-ARFI-based elastography techniques have previously been used in thermal ablation studies [93, 43]. The benefit of this method is that it does not require additional hardware apart from the therapy transducer. Although the elastography measurements could be time-consuming, our initial results show that MR-ARFI does encode the changes in tissue elasticity due to histotripsy.

To evaluate the change in MR-ARFI encoded displacement, a volume histotripsy lesion was generated in a *ex-vivo* bovine brain. The volume lesion of size $5\,\text{mm} \times 5\,\text{mm} \times 30\,\text{mm}$ was generated with $0.5\,\text{mm} \times 0.5\,\text{mm} \times 5\,\text{mm}$ spacing with 500 Hz pulse repetition frequency and 75 MPa peak-negative pressure. Histotripsy dose was increased by increasing the number of sonications per location: 1, 6, 10, 15, 20, 30 and 50 reps/location. After each dose was delivered to the tissue, MR-ARFI scan was acquired using the same MRI pulse sequence as described in Chapter 4. Fig. 7.1 shows the response of MR-ARFI displacement to increasing

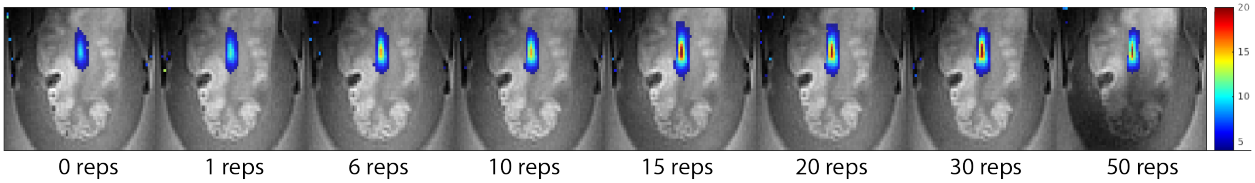

(a) MR-ARFI image for the same tissue at different histotripsy dose levels

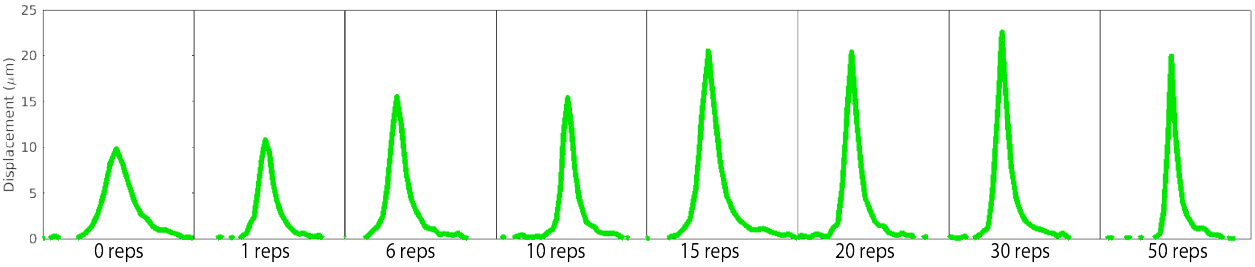

(b) MR-ARFI along the center of the displacement region for each dose. The peak displacement increased from 10 μm to 22 μm away from the transducer

Figure 7.1: The effect of histotripsy dose on MR-ARFI displacement maps.

histotripsy dose. The acoustic radiation force F can be evaluated as:

$$F = \frac{2\alpha I}{c}, \tag{7.1}$$

where α is the medium's absorption coefficient, I is the acoustic intensity, and c is the velocity of the sonicating wave. Since the applied acoustic intensity I between each column of Fig. 7.1 is the same, the change in the radiation force can be assumed to come from the change in the medium's absorption. Based on the MR-ARFI images, a $\Delta\alpha$ metric could be derived as a surrogate for histotripsy dose.

BIBLIOGRAPHY

[1] Steven P. Allen, Timothy L. Hall, Charles A. Cain, and Luis Hernandez-Garcia. Controlling cavitation-based image contrast in focused ultrasound histotripsy surgery. *Magnetic Resonance in Medicine*, 73(1):204–213, January 2015.

[2] Steven P. Allen, Luis Hernandez-Garcia, Charles A. Cain, and Timothy L. Hall. MR-based detection of individual histotripsy bubble clouds formed in tissues and phantoms. *Magnetic Resonance in Medicine*, 76(5):1486–1493, November 2016.

[3] Steven P. Allen, Eli Vlaisavljevich, Jiaqi Shi, Luis Hernandez-Garcia, Charles A. Cain, Zhen Xu, and Timothy L. Hall. The response of MRI contrast parameters in in vitro tissues and tissue mimicking phantoms to fractionation by histotripsy. *Physics in Medicine and Biology*, 62(17):7167–7180, August 2017.

[4] David C. Alsop. Phase insensitive preparation of single-shot rare: Application to diffusion imaging in humans. *Magnetic Resonance in Medicine*, 38:527–533, October 1997.

[5] American Brain Tumor Association. Metastatic brain tumor.

[6] Kenneth B Bader and Christy K Holland. The influence of medium elasticity on the prediction of histotripsy-induced bubble expansion and erythrocyte viability. *Physics in Medicine and Biology*, 63:095010, May 2018.

[7] Kenneth B. Bader, Eli Vlaisavljevich, and Adam D. Maxwell. For whom the bubble grows: Physical principles of bubble nucleation and dynamics in histotripsy ultrasound therapy. *Ultrasound in Medicine and Biology*, 45(5):1056–1080, May 2019.

[8] C. Badve, A. Yu, S. Dastmalchian, M. Rogers, D. Ma, Y. Jiang, S. Margevicius, S. Pahwa, Z. Lu, M. Schluchter, J. Sunshine, M. Griswold, A. Sloan, and V. Gulani. MR fingerprinting of adult brain tumors: Initial experience. *American Journal of Neuroradiology*, 38:492–499, March 2017.

[9] Rachel R. Bitton and Kim R.Butts Pauly. MR-acoustic radiation force imaging (MR-ARFI) and susceptibility weighted imaging (SWI) to visualize calcifications in ex vivo swine brain. *Journal of Magnetic Resonance Imaging*, 39:1294–1300, May 2014.

[10] Stefan Blüml, Lothar R. Schad, Boris Stepanow, and Walter J. Lorenz. Spin-lattice relaxation time measurement by means of a turboflash technique. *Magnetic Resonance in Medicine*, 30:289–295, September 1993.

[11] Cancer.Net Editorial Board. Brain tumor: Statistics. pages 1–3, 2023.

[12] Adomas Bunevicius, Nathan Judson McDannold, and Alexandra J Golby. Focused ultrasound strategies for brain tumor therapy. *Operative Neurosurgery*, 19(1):9–18, December 2019.

[13] Jing Chen, Ron Watkins, and Kim Butts Pauly. Optimization of encoding gradients for MR-ARFI. *Magnetic Resonance in Medicine*, 63(4):1050–1058, 2010.

[14] Karine Choquet, Jonathan Vappou, Paolo Cabras, Ounay Ishak, Afshin Gangi, and Elodie Breton. Magnetic resonance acoustic radiation force imaging (MR-ARFI) for the monitoring of High Intensity Focused Ultrasound (HIFU) ablation in anisotropic tissue. *Magnetic Resonance Materials in Physics, Biology and Medicine*, 36:737–747, October 2023.

[15] Or Cohen-Inbar, John Snell, Zhiyuan Xu, and Jason Sheehan. What holds focused ultrasound back? *World Neurosurgery*, 91:661–665, 2016.

[16] Jeffrey T. Cole, Angela Yarnell, William S. Kean, Eric Gold, Bobbi Lewis, Ming Ren, David C. McMullen, David M. Jacobowitz, Harvey B. Pollard, J. Timothy O'Neill, Neil E. Grunberg, Clifton L. Dalgard, Joseph A. Frank, and William D. Watson. Craniotomy: True sham for traumatic brain injury, or a sham of a sham? *Journal of Neurotrauma*, 28(3):359–369, March 2011.

[17] Daniel Coluccia, Javier Fandino, Lucia Schwyzer, Ruth O'Gorman, Luca Remonda, Javier Anon, Ernst Martin, and Beat Werner. First noninvasive thermal ablation of a brain tumor with MR-guided focused ultrasound. *Journal of Therapeutic Ultrasound*, 2(1):1–7, October 2014.

[18] Joshua T. de Bever, Henrik Odéen, Lorne W. Hofstetter, and Dennis L. Parker. Simultaneous MR thermometry and acoustic radiation force imaging using interleaved acquisition. *Magnetic Resonance in Medicine*, 79:1515–1524, 2018.

[19] Joshua T. de Bever, Henrik Odéen, Nick Todd, Alexis I. Farrer, and Dennis L. Parker. Evaluation of a three-dimensional MR acoustic radiation force imaging pulse sequence using a novel unbalanced bipolar motion encoding gradient. *Magnetic Resonance in Medicine*, 76(3):803–813, 2016.

[20] Sarah Duclos, Andrew Golin, Adam Fox, Neeraj Chaudhary, Sandra Camelo-Piragua, Aditya Pandey, and Zhen Xu. Transcranial histotripsy parameter study in primary and metastatic murine brain tumor models. *International Journal of Hyperthermia*, 40, December 2023.

[21] Howard M. Eisenberg, Vibhor Krishna, W. Jeffrey Elias, G. Rees Cosgrove, Dheeraj Gandhi, Charlene E. Aldrich, and Paul S. Fishman. MR-guided focused ultrasound pallidotomy for Parkinson's disease: safety and feasibility. *Journal of Neurosurgery*, 135(3):792–798, September 2021.

[22] W. Jeffrey Elias, Diane Huss, Tiffini Voss, Johanna Loomba, Mohamad Khaled, Eyal Zadicario, Robert C. Frysinger, Scott A. Sperling, Scott Wylie, Stephen J. Monteith, Jason Druzgal, Binit B. Shah, Madaline Harrison, and Max Wintermark. A pilot study of focused ultrasound thalamotomy for essential tremor. *New England Journal of Medicine*, 369:640–648, August 2013.

[23] Jeffrey A. Fessler, Sangwoo Lee, Valur T. Olafsson, Hugo R. Shi, and Douglas C. Noll. Toeplitz-based iterative image reconstruction for MRI with correction for magnetic field inhomogeneity. *IEEE Transactions on Signal Processing*, 53(9):3393–3402, September 2005.

[24] Jeffrey A. Fessler and Bradley P. Sutton. Nonuniform fast fourier transforms using min-max interpolation. *IEEE Transactions on Signal Processing*, 51(2):560–574, February 2003.

[25] Kirsten P. Forbes, James G. Pipe, John P. Karis, and Joseph E. Heiserman. Improved image quality and detection of acute cerebral infarction with propeller diffusion-weighted MR imaging. *Radiology*, 225:551–555, November 2002.

[26] Jens Frahm, Klaus-Dietmar Merboldt, and Wolfgang Hänicke. Localized proton spectroscopy using stimulated echoes. *Journal of Magnetic Resonance (1969)*, 72:502–508, May 1987.

[27] Tyler Gerhardson, Jonathan R. Sukovich, Aditya S. Pandey, Timothy L. Hall, Charles A. Cain, and Zhen Xu. Catheter hydrophone aberration correction for transcranial histotripsy treatment of intracerebral hemorrhage: Proof-of-concept. *IEEE Transactions on Ultrasonics, Ferroelectrics, and Frequency Control*, 64:1684–1697, November 2017.

[28] Tyler Gerhardson, Jonathan R. Sukovich, Aditya S. Pandey, Timothy L. Hall, Charles A. Cain, and Zhen Xu. Effect of frequency and focal spacing on transcranial histotripsy clot liquefaction, using electronic focal steering. *Ultrasound in Medicine and Biology*, 43(10):2302–2317, October 2017.

[29] Dennis C. Ghiglia and Mark D. Pritt. *Two-dimensional phase unwrapping*. Wiley, New York, 1998.

[30] Dana Greene-Schloesser, Mike E. Robbins, Ann M. Peiffer, Edward G. Shaw, Kenneth T. Wheeler, and Michael D. Chan. Radiation-induced brain injury: A review. *Frontiers in Oncology*, 2:1–18, 2012.

[31] Dinank Gupta, Dave Choi, Ning Lu, Steven P. Allen, Timothy L. Hall, Douglas C. Noll, and Zhen Xu. Magnetic resonance thermometry targeting for magnetic resonance–guided histotripsy treatments. *Ultrasound in Medicine and Biology*, 49(5):1102–1107, May 2023.

[32] Dinank Gupta, Tarana Kaovasia, Steven Allen, Timothy Hall, Zhen Xu, and Douglas Noll. MRI-guided histotripsy targeting using MR-Thermometry and MR-ARFI. In Proceedings of the 33rd Annual Meeting of ISMRM, 2024.

[33] Dinank Gupta, Tarana Kaovasia, Steven Allen, Timothy Hall, Zhen Xu, and Douglas Noll. Transcranial MRI guided histotripsy targeting using MR-ARFI and MR-thermometry. Ultrasound in Medicine and Biology, Submitted.

[34] Dinank Gupta, Tarana Kaovasia, Dave Choi, Ning Lu, Steven Allen, Timothy Hall, Douglas Noll, and Zhen Xu. Evaluating histotripsy treatment dosage in the brain using MRI. In Proceedings of the 22nd Annual Meeting of ISTU, Lyon, 2023.

[35] Dinank Gupta, Tarana Kaovasia, Dave Choi, Ning Lu, Steven Allen, Timothy Hall, Zhen Xu, and Douglas Noll. Evaluating histotripsy treatment dosage in the brain using MRI. In Proceedings of the 32nd Annual Meeting of ISMRM, 2023.

[36] A Haase, J Frahm, D Matthaei, W Hänicke, H Bomsdorf, D Kunz, and R Tischler. MR imaging using stimulated echoes (STEAM). *Radiology*, 160:787–790, September 1986.

[37] E. L. Hahn. Spin echoes. *Physical Review*, 80:580–594, November 1950.

[38] T. L. Hall, J. B. Fowlkes, and C. A. Cain. Imaging feedback of tissue liquefaction (histotripsy) in ultrasound surgery. *Proceedings - IEEE Ultrasonics Symposium*, 3:1732–1734, 2005.

[39] Scott C Haskell, Ning Lu, Greyson E Stocker, Zhen Xu, and Jonathan R Sukovich. Monitoring cavitation dynamics evolution in tissue mimicking hydrogels for repeated exposures via acoustic cavitation emissions. *The Journal of the Acoustical Society of America*, 153:237–247, January 2023.

[40] Y. Hertzberg, A. Volovick, Y. Zur, Y. Medan, S. Vitek, and G. Navon. Ultrasound focusing using magnetic resonance acoustic radiation force imaging: Application to ultrasound transcranial therapy. *Medical Physics*, 37:2934–2942, 2010.

[41] Shawn L. Hervey-Jumper and Mitchel S. Berger. Maximizing safe resection of low- and high-grade glioma. *Journal of Neuro-Oncology*, 130(2):269–282, May 2016.

[42] J. C. Hindman. Proton resonance shift of water in the gas and liquid states. *The Journal of Chemical Physics*, 44(12):4582–4592, June 1966.

[43] Lorne W. Hofstetter, Henrik Odéen, Bradley D. Bolster, Alexander Mueller, Douglas A. Christensen, Allison Payne, and Dennis L. Parker. Efficient shear wave elastography using transient acoustic radiation force excitations and MR displacement encoding. *Magnetic Resonance in Medicine*, 81:3153–3167, 2019.

[44] Andrew B. Holbrook, Juan M. Santos, Elena Kaye, Viola Rieke, and Kim Butts Pauly. Real-time MR thermometry for monitoring HIFU ablations of the liver. *Magnetic Resonance in Medicine*, 63:365–373, February 2010.

[45] K Hynynen, WR Freund, HE Cline, AH Chung, RD Watkins, JP Vetro, and FA Jolesz. A clinical, noninvasive, MR imaging-monitored ultrasound surgery method. *RadioGraphics*, 16(1):185–195, January 1996.

[46] NIH National Cancer Institute. Cancer facts and figures 2020. *CA: A Cancer Journal for Clinicians*, pages 1–76, 2020.

[47] Bio Joo, Mi Suk Park, Soo Hyeon Lee, Hye Jin Choi, Seung Tack Lim, Sun Young Rha, Itay Rachmilevitch, Young Han Lee, and Jin Suck Suh. Pain palliation in patients with bone metastases using magnetic resonance-guided focused ultrasound with conformal bone system: A preliminary report. *Yonsei Medical Journal*, 56(2):503–509, feb 2015.

[48] Na Young Jung and Jin Woo Chang. Magnetic resonance-guided focused ultrasound in neurosurgery: Taking lessons from the past to inform the future. *Journal of Korean Medical Science*, 33(44), sep 2018.

[49] Elena A. Kaye, Jing Chen, and Kim Butts Pauly. Rapid MR-ARFI method for focal spot localization during focused ultrasound therapy. *Magnetic Resonance in Medicine*, 65(3):738–743, 2011.

[50] Elena A. Kaye, Yoni Hertzberg, Michael Marx, Beat Werner, Gil Navon, Marc Levoy, and Kim Butts Pauly. Application of Zernike polynomials towards accelerated adaptive focusing of transcranial high intensity focused ultrasound. *Medical Physics*, 39:6254–6263, 2012.

[51] Elena A. Kaye and Kim Butts Pauly. Adapting MRI acoustic radiation force imaging for in vivo human brain focused ultrasound applications. *Magnetic Resonance in Medicine*, 69:724–733, 2013.

[52] Daeun Kim, Stephen F. Cauley, Krishna S. Nayak, Richard M. Leahy, and Justin P. Haldar. Region-optimized virtual (ROVir) coils: Localization and/or suppression of spatial regions using sensor-domain beamforming. *Magnetic Resonance in Medicine*, 86:197–212, July 2021.

[53] Nan kuei Chen, Arnaud Guidon, Hing Chiu Chang, and Allen W. Song. A robust multi-shot scan strategy for high-resolution diffusion weighted MRI enabled by multiplexed sensitivity-encoding (MUSE). *NeuroImage*, 72:41–47, May 2013.

[54] Benoît Larrat, Mathieu Pernot, Gabriel Montaldo, Mathias Fink, and Mickaël Tanter. MR-guided adaptive focusing of ultrasound. *IEEE Transactions on Ultrasonics, Ferroelectrics, and Frequency Control*, 57:1734–1747, 2010.

[55] Benjamin Lassen, Eirik Helseth, Pål Rønning, David Scheie, Tom Børge Johannesen, Jan Maehlen, Iver A. Langmoen, and Torstein R. Meling. Surgical mortality at 30 days and complications leading to recraniotomy in 2630 consecutive craniotomies for intracranial tumors. *Neurosurgery*, 68(5):1259–1269, May 2011.

[56] Kelvin J. Layton, Stefan Kroboth, Feng Jia, Sebastian Littin, Huijun Yu, Jochen Leupold, Jon-Fredrik Nielsen, Tony Stöcker, and Maxim Zaitsev. Pulseq: A rapid and hardware-independent pulse sequence prototyping framework. *Magnetic Resonance in Medicine*, 77:1544–1552, April 2017.

[57] Suzanne LeBlang and Timothy J. Ziemlewicz. The art of histotripsy: a focused ultrasound application that has the potential to treat from head to toe! *International Journal of Hyperthermia*, 41, December 2024.

[58] Suzanne D. Leblang, Katherine Hoctor, and Fred L. Steinberg. Leiomyoma shrinkage after MRI-guided focused ultrasound treatment: Report of 80 patients. *American Journal of Roentgenology*, 194:274–280, 2010.

[59] Zhi-Pei Liang. Spatiotemporal imaging with partially separable functions. pages 181–182. IEEE, October 2007.

[60] Claire Yilin Lin and Jeffrey A. Fessler. Efficient dynamic parallel MRI reconstruction for the low-rank plus sparse model. *IEEE Transactions on Computational Imaging*, 5:17–26, March 2019.

[61] Kuang Wei Lin, Yohan Kim, Adam Maxwell, Tzu Yin Wang, Timothy Hall, Zhen Xu, J. Fowlkes, and Charles Cain. Histotripsy beyond the intrinsic cavitation threshold using very short ultrasound pulses: Microtripsy. *IEEE Transactions on Ultrasonics, Ferroelectrics, and Frequency Control*, 61:251–265, 2014.

[62] Mark E. Linskey, David W. Andrews, Anthony L. Asher, Stuart H. Burri, Douglas Kondziolka, Paula D. Robinson, Mario Ammirati, Charles S. Cobbs, Laurie E. Gaspar, Jay S. Loeffler, Michael McDermott, Minesh P. Mehta, Tom Mikkelsen, Jeffrey J. Olson, Nina A. Paleologos, Roy A. Patchell, Timothy C. Ryken, and Steven N. Kalkanis. The role of stereotactic radiosurgery in the management of patients with newly diagnosed brain metastases: A systematic review and evidence-based clinical practice guideline. *Journal of Neuro-Oncology*, 96:45–68, 2010.

[63] Nir Lipsman, Michael L. Schwartz, Yuexi Huang, Liesly Lee, Tejas Sankar, Martin Chapman, Kullervo Hynynen, and Andres M. Lozano. MR-guided focused ultrasound thalamotomy for essential tremor: a proof-of-concept study. *The Lancet Neurology*, 12(5):462–468, May 2013.

[64] Emil Ljungberg, Nikou L. Damestani, Tobias C. Wood, David J. Lythgoe, Fernando Zelaya, Steven C.R. Williams, Ana Beatriz Solana, Gareth J. Barker, and Florian Wiesinger. Silent zero TE MR neuroimaging: Current state-of-the-art and future directions. *Progress in Nuclear Magnetic Resonance Spectroscopy*, 123:73–93, April 2021.

[65] Ning Lu, Dinank Gupta, Badih J. Daou, Adam Fox, Dave Choi, Jonathan R. Sukovich, Timothy L. Hall, Sandra Camelo-Piragua, Neeraj Chaudhary, John Snell, Aditya S. Pandey, Douglas C. Noll, and Zhen Xu. Transcranial magnetic resonance-guided histotripsy for brain surgery: Pre-clinical investigation. *Ultrasound in Medicine and Biology*, 48(1):98–110, January 2022.

[66] Ning Lu, Timothy L. Hall, Dave Choi, Dinank Gupta, Badih J. Daou, Jonathan R. Sukovich, Adam Fox, Tyler I. Gerhardson, Aditya S. Pandey, Douglas C. Noll, and

Zhen Xu. Transcranial MR-guided histotripsy system. *IEEE Transactions on Ultrasonics, Ferroelectrics, and Frequency Control*, 68(9):2917–2929, September 2021.

[67] Ning Lu, Timothy L. Hall, Jonathan R. Sukovich, Sang Won Choi, John Snell, Nathan McDannold, and Zhen Xu. Two-step aberration correction: application to transcranial histotripsy. *Physics in Medicine and Biology*, 67:125009, June 2022.

[68] Tianrui Luo, Douglas C. Noll, Jeffrey A. Fessler, and Jon-Fredrik Nielsen. Joint design of RF and gradient waveforms via auto-differentiation for 3d tailored excitation in MRI. *IEEE Transactions on Medical Imaging*, 40:3305–3314, August 2020.

[69] Michael Lustig, David Donoho, and John M. Pauly. Sparse MRI: The application of compressed sensing for rapid MR imaging. *Magnetic Resonance in Medicine*, 58:1182–1195, December 2007.

[70] L. Marsac, D. Chauvet, B. Larrat, M. Pernot, B. Robert, M. Fink, A. L. Boch, J. F. Aubry, and M. Tanter. MR-guided adaptive focusing of therapeutic ultrasound beams in the human head. *Medical Physics*, 39:1141–1149, February 2012.

[71] Adam D Maxwell, Tzu-Yin Wang, Charles A Cain, ; J Brian Fowlkes, Oleg A Sapozhnikov, Michael R Bailey, and Zhen Xu. Cavitation clouds created by shock scattering from bubbles during histotripsy. *J. Acoust. Soc. Am*, 130:1888–1898, 2011.

[72] Nathan McDannold, Greg T. Clement, Peter Black, Ferenc Jolesz, and Kullervo Hynynen. Transcranial magnetic resonance imaging– guided focused ultrasound surgery of brain tumors: Initial findings in 3 patients. *Neurosurgery*, 66(2):323–332, February 2010.

[73] Nathan McDannold and Stephan E. Maier. Magnetic resonance acoustic radiation force imaging. *Medical Physics*, 35(8):3748–3758, July 2008.

[74] Ying Meng, Suganth Suppiah, Shanan Surendrakumar, Luca Bigioni, and Nir Lipsman. Low-intensity MR-guided focused ultrasound mediated disruption of the blood-brain barrier for intracranial metastatic diseases. *Frontiers in Oncology*, 8:1–8, August 2018.

[75] Ryan M. Miller, Adam D. Maxwell, Tzu Yin Wang, J. Brian Fowlkes, Charles A. Cain, and Zhen Xu. Real-time elastography-based monitoring of histotripsy tissue fractionation using color doppler. *IEEE International Ultrasonics Symposium, IUS*, pages 196–199, 2012.

[76] Ryan M. Miller, Xi Zhang, Adam D. Maxwell, Tzu Yin Wang, J. Brian Fowlkes, Charles A. Cain, and Zhen Xu. Investigation of the mechanism of ARFI-based color Dopplerfeedback of histotripsy tissue fractionation. *IEEE International Ultrasonics Symposium, IUS*, pages 934–937, 2013.

[77] William K. Miller, Kathryn N. Becker, Andrew J. Caras, Tarek R. Mansour, Malik T. Mays, Mehmood Rashid, and Jason Schwalb. Magnetic resonance-guided focused ultrasound treatment for essential tremor shows sustained efficacy: a meta-analysis. *Neurosurgical Review*, 45:533–544, February 2022.

[78] Morteza Mohammadjavadi, Ryan T. Ash, Ningrui Li, Pooja Gaur, Jan Kubanek, Yamil Saenz, Gary H. Glover, Gerald R. Popelka, Anthoney M. Norcia, and Kim Butts Pauly. Transcranial ultrasound neuromodulation of the thalamic visual pathway in a large animal model and the dose-response relationship with MR-ARFI. *Scientific Reports*, 12:1–14, November 2022.

[79] Raja Muthupillai, Phillip J. Rossman, David J. Lomas, James F. Greenleaf, Stephen J. Riederer, and Richard L. Ehman. Magnetic resonance imaging of transverse acoustic strain waves. *Magnetic Resonance in Medicine*, 36:266–274, August 1996.

[80] Jon Fredrik Nielsen and Douglas C. Noll. TOPPE: A framework for rapid prototyping of MR pulse sequences. *Magnetic Resonance in Medicine*, 79:3128–3134, June 2018.

[81] Douglas C. Noll, Jeffrey A. Fessler, and Bradley P. Sutton. Conjugate phase MRI reconstruction with spatially variant sample density correction. *IEEE Transactions on Medical Imaging*, 24(2):325–336, 2005.

[82] Henrik Odéen and Dennis L. Parker. Magnetic resonance thermometry and its biological applications – physical principles and practical considerations. *Progress in Nuclear Magnetic Resonance Spectroscopy*, 110:34–61, February 2019.

[83] Quinn T. Ostrom, Haley Gittleman, Gabrielle Truitt, Alexander Boscia, Carol Kruchko, and Jill S. Barnholtz-Sloan. CBTRUS statistical report: Primary brain and other central nervous system tumors diagnosed in the united states in 2011–2015. *Neuro-Oncology*, 20:1–86, October 2018.

[84] W. M. Pardridge. Blood-brain barrier drug targeting: The future of brain drug development. *Molecular Interventions*, 3(2):90–105, March 2003.

[85] Jessica E. Parsons, Charles A. Cain, Gerald D. Abrams, and J. Brian Fowlkes. Pulsed cavitational ultrasound therapy for controlled tissue homogenization. *Ultrasound in Medicine and Biology*, 32(1):115–129, January 2006.

[86] Kim Butts Pauly, Viola Rieke, Andrew B. Holbrook, Will Grissom, Jean Chen, and Elena Kaye. MR-guidance of HIFU Therapy. In *Proceedings of the 31st Annual International Conference of the IEEE Engineering in Medicine and Biology Society: Engineering the Future of Biomedicine, EMBC 2009*, pages 141–144. IEEE, sep 2009.

[87] John De Poorter, Carlos De Wagter, Yves De Deene, Carsten Thomsen, Freddy Ståhlberg, and Eric Achten. Noninvasive MRI Thermometry with the proton resonance frequency (PRF) method: In vivo results in human muscle. *Magnetic Resonance in Medicine*, 33:74–81, January 1995.

[88] Shibin Qu, Tejaswi Worlikar, Amy E Felsted, Anutosh Ganguly, Megan V Beems, Ryan Hubbard, Ashley L Pepple, Alicia A Kevelin, Hannah Garavaglia, Joe Dib, Mariam Toma, Hai Huang, Allan Tsung, Zhen Xu, and Clifford Suhyun Cho. Non-thermal histotripsy tumor ablation promotes abscopal immune responses that enhance cancer immunotherapy. *Journal for ImmunoTherapy of Cancer*, 8:200, 2020.

[89] Viola Rieke and Kim Butts Pauly. MR thermometry. *Journal of Magnetic Resonance Imaging*, 27(2):376–390, January 2008.

[90] Francesco Sammartino, Dylan W. Beam, John Snell, and Vibhor Krishna. Kranion, an open-source environment for planning transcranial focused ultrasound surgery: technical note. *Journal of Neurosurgery*, 132(4):1249–1255, 2020.

[91] Stephen A. Sapareto and William C. Dewey. Thermal dose determination in cancer therapy. *International Journal of Radiation Oncology, Biology, Physics*, 10:787–800, 1984.

[92] Karun V. Sharma, Pavel S. Yarmolenko, Haydar Celik, Avinash Eranki, Ari Partanen, Anilawan Smitthimedhin, Aerang Kim, Matthew Oetgen, Domiciano Santos, Janish Patel, and Peter Kim. Comparison of noninvasive high-intensity focused ultrasound with radiofrequency ablation of osteoid osteoma. *Journal of Pediatrics*, 190:222–228.e1, November 2017.

[93] Rémi Souchon, Rares Salomir, Olivier Beuf, Laurent Milot, Denis Grenier, Denis Lyonnet, Jean Yves Chapelon, and Olivier Rouvière. Transient MR elastography (t-MRE) using ultrasound radiation force: Theory, safety, and initial experiments in vitro. *Magnetic Resonance in Medicine*, 60:871–881, October 2008.

[94] Jonathan R. Sukovich, Charles A. Cain, Aditya S. Pandey, Neeraj Chaudhary, Sandra Camelo-Piragua, Steven P. Allen, Timothy L. Hall, John Snell, Zhiyuan Xu, Jonathan M. Cannata, Dejan Teofilovic, James A. Bertolina, Neal Kassell, and Zhen Xu. In vivo histotripsy brain treatment. *Journal of Neurosurgery*, 131(4):1331–1338, October 2019.

[95] Jonathan R. Sukovich, Jonathan J. MacOskey, Jonathan E. Lundt, Tyler I. Gerhardson, Timothy L. Hall, and Zhen Xu. Real-time transcranial histotripsy treatment localization and mapping using acoustic cavitation emission feedback. *IEEE Transactions on Ultrasonics, Ferroelectrics, and Frequency Control*, 67:1178–1191, June 2020.

[96] Jonathan R. Sukovich, Zhen Xu, Yohan Kim, Hui Cao, Thai Son Nguyen, Aditya S. Pandey, Timothy L. Hall, and Charles A. Cain. Targeted lesion generation through the skull without aberration correction using histotripsy. *IEEE Transactions on Ultrasonics, Ferroelectrics, and Frequency Control*, 63:671–682, May 2016.

[97] Hyuna Sung, Jacques Ferlay, Rebecca L. Siegel, Mathieu Laversanne, Isabelle Soerjomataram, Ahmedin Jemal, and Freddie Bray. Global cancer statistics 2020: GLOBOCAN estimates of incidence and mortality worldwide for 36 cancers in 185 countries. *CA: A Cancer Journal for Clinicians*, 71:209–249, May 2021.

[98] Jonathan Vappou, Pierre Bour, Fabrice Marquet, Valery Ozenne, and Bruno Quesson. MR-ARFI-based method for the quantitative measurement of tissue elasticity: Application for monitoring HIFU therapy. *Physics in Medicine and Biology*, 63, 2018.

[99] Joan Vidal-Jove, Xavier Serres, Eli Vlaisavljevich, Jon Cannata, Alex Duryea, Ryan Miller, Xavier Merino, Manuela Velat, Yossi Kam, Ryan Bolduan, Joseph Amaral, Timothy Hall, Zhen Xu, Fred T. Lee, and Timothy J. Ziemlewicz. First-in-man histotripsy of hepatic tumors: the theresa trial, a feasibility study. *International Journal of Hyperthermia*, 39(1):1115–1123, August 2022.

[100] Eli Vlaisavljevich, Tyler Gerhardson, Tim Hall, and Zhen Xu. Effects of f-number on the histotripsy intrinsic threshold and cavitation bubble cloud behavior. *Physics in Medicine and Biology*, 62:1269–1290, January 2017.

[101] Eli Vlaisavljevich, Yohan Kim, Gabe Owens, William Roberts, Charles Cain, and Zhen Xu. Effects of tissue mechanical properties on susceptibility to histotripsy-induced tissue damage. *Physics in Medicine and Biology*, 59:253–270, 2014.

[102] Eli Vlaisavljevich, Adam Maxwell, Lauren Mancia, Eric Johnsen, Charles Cain, and Zhen Xu. Visualizing the histotripsy process: Bubble cloud–cancer cell interactions in a tissue-mimicking environment. *Ultrasound in Medicine and Biology*, 42:2466–2477, 2016.

[103] Eli Vlaisavljevich, Adam Maxwell, Matthew Warnez, Eric Johnsen, Charles a Cain, and Zhen Xu. Histotripsy-induced cavitation cloud mechanical properties. *IEEE Trans. Ultrason. Ferroelectr. Freq. Control*, 61:341–352, 2014.

[104] M. J. Voogt, H. Trillaud, Y. S. Kim, W. P.Th M. Mali, J. Barkhausen, L. W. Bartels, R. Deckers, N. Frulio, H. Rhim, H. K. Lim, T. Eckey, H. J. Nieminen, C. Mougenot, B. Keserci, J. Soini, T. Vaara, M. O. Köhler, S. Sokka, and Maurice A.A.J. Van Den Bosch. Volumetric feedback ablation of uterine fibroids using magnetic resonance-guided high intensity focused ultrasound therapy. *European Radiology*, 22:411–417, February 2012.

[105] Tzu Yin Wang, Timothy L. Hall, Zhen Xu, J. Brian Fowlkes, and Charles A. Cain. Imaging feedback of histotripsy treatments using ultrasound shear wave elastography. *IEEE Transactions on Ultrasonics, Ferroelectrics, and Frequency Control*, 59:1167–1181, 2012.

[106] Tejaswi Worlikar, Man Zhang, Anutosh Ganguly, Timothy L. Hall, Jiaqi Shi, Lili Zhao, Fred T. Lee, Mishal Mendiratta-Lala, Clifford S. Cho, and Zhen Xu. Impact of histotripsy on development of intrahepatic metastases in a rodent liver tumor model. *Cancers*, 14:1612, April 2022.

[107] Zhen Xu, Timothy L. Hall, Eli Vlaisavljevich, and Fred T. Lee. Histotripsy: the first noninvasive, non-ionizing, non-thermal ablation technique based on ultrasound. *International Journal of Hyperthermia*, 38(1):561–575, January 2021.

[108] Zhen Xu, Achian Ludomirsky, Lucy Y. Eun, Timothy L. Hall, Binh C. Tran, J. Brian Fowlkes, and Charles A. Cain. Controlled ultrasound tissue erosion. *IEEE Transactions on Ultrasonics, Ferroelectrics, and Frequency Control*, 51(6):726–736, June 2004.

[109] Ellen Yeats, Ning Lu, Jonathan R. Sukovich, Zhen Xu, and Timothy L. Hall. Soft tissue aberration correction for histotripsy using acoustic emissions from cavitation cloud nucleation and collapse. *Ultrasound in Medicine and Biology*, 49:1182–1193, May 2023.

[110] Yuan Zheng, Michael Marx, G. Wilson Miller, and Kim Butts Pauly. High sensitivity MR acoustic radiation force imaging using transition band balanced steady-state free precession. *Magnetic Resonance in Medicine*, 79(3):1532–1537, 2018.